Karlsruhe Institute of Technology

IEKP-KA/2013-21

Calibration of the digital readout chip of the CMS Pixel Detector Phase I Upgrade

Benedikt Freund

Diplomarbeit

Fakultät für Physik
Institut für Experimentelle Kernphysik (IEKP)

Referent: Prof. Dr. Ulrich Husemann
Korreferent: Prof. Dr. Marc Weber

Karlsruhe, 30. September 2013

Deutsche Zusammenfassung

In den Jahren 2013/14 wird der Large Hadron Collider (LHC) konsolidiert [EB08], sodass die Kollisionsenergie sowie die instantane Luminosität gesteigert wird mit dem Ziel, eine erhöhte Anzahl an Teilchenkollisionen in den Experimenten zu erreichen. Dank der erhöhten Kollisionsenergie verändern sich Wirkungsquerschnitte für interessante physikalische Prozesse wie die Higgs-Produktion. Für die Experimente ergibt sich daraus die Möglichkeit, präzisere Messungen der Teilcheneigenschaften durchzuführen.

Im Detail bedeutet dies, dass der Beschleuniger nach der Konsolidierung die doppelte Designluminosität $\mathcal{L} = 2 \times 10^{34}\,\mathrm{cm}^{-2}\mathrm{s}^{-1}$ bei 14 TeV Schwerpunktsenergie erreichen wird [D$^+$12, Zim09]. Aufgrund der gesteigerten Luminosität wird sich die Anzahl der simultan eintretenden Teilchenkollisionen (pile-up) erhöhen, die von den Experimenten getrennt aufgelöst werden müssen. Bisher hatte der Compact Muon Solenoid (CMS) Detektor [CMS08] 25 simultane Teilchenkollisionen bei einer instantanen Luminosität von $\mathcal{L} = 7.75 \times 10^{33}\,\mathrm{cm}^{-2}\mathrm{s}^{-1}$ zu separieren. Bei erhöhter Schwerpunktsenergie und doppelter Designluminosität könnten bis zu 50 Kollisionen gleichzeitig auftreten, die zu trennen wären [D$^+$12]. Um sicher zu stellen, dass der Pixeldetektor unter diesen erschwerten Bedingungen effizient betrieben werden kann, wird dieser im Zuge des Phase-I-Upgrades ersetzt. Das Silizium-Sensormaterial muss ersetzt werden, da aufgrund der steigenden Teilchenraten die auftretenden Strahlenschäden im Laufe der Zeit ein nicht tragbares Maß erreichen. Außerdem ist es notwendig, den Auslesechip (Readout Chip, ROC) auszutauschen, da der aktuelle ROC wegen der zu erwartenden erhöhten Okkupanz deutliche Datenverluste aufweisen würde [Mei11]. Um dem entgegenzuwirken, wurde ein neuer ROC (PSI46dig) entwickelt, der über größere Zwischenspeicher verfügt und die Daten in einem digitalen Format überträgt. Zusätzlich muss auch der Token Bit Manager (TBM) angepasst werden, welcher für die Trigger-Signalverarbeitung verantwortlich ist und die Auslese der ROCs koordiniert.

Abgesehen von den Änderungen betreffend des ROCs sind auch Modifikationen der Pixeldetektorgeometrie vorgesehen. Um weiterhin die Teilchenspuren und die zugehörigen Wechselwirkungspunkte verlässlich rekonstruieren zu können, wird die Anzahl an sensitiven Lagen im Zentralbereich von drei auf vier und im Bereich der beiden Endkappen von zwei auf drei erhöht. Zusätzlich ermöglicht der geringere Durchmesser der neuen LHC-Strahlröhre, die innerste Lage des Zentralbereichs näher an den Kollisionspunkt zu bringen.

Die sensitiven Lagen sind aus kleineren Untereinheiten aufgebaut, den sogenannten Modulen. Ab 2014 wird am Karlsruher Institut für Technologie (KIT) die Hälfte der Module für die neue vierte Lage im Zentralbereich gefertigt werden. Im Anschluss an die Modulproduktion wird mittels Röntgenstrahlung definierter Energie eine Energiekalibration durchgeführt, mit welcher sich diese Diplomarbeit befasst.

Auch wenn der Pixeldetektor nicht für Energiemessungen vorgesehen ist, so ist eine Energiekalibration dennoch notwendig, da die Ortsauflösung des Detektors durch sogenanntes „Charge Sharing“ verbessert wird [CMS10]. Als Charge Sharing bezeichnet man den Effekt, wenn Teilchen eine Detektorlage durchqueren und Ladung nicht nur im getroffenen Pixel, sondern aufgrund des Lorentzdrifts, infolge des Magnetfelds auch in benachbarten Pixeln

generieren. Die Pixel, in denen Ladung von einem einzigen Teilchendurchgang deponiert wurde, nennt man Cluster. Eine Verbesserung der Auflösung wird dadurch erzielt, dass nachdem die Pulshöhen der Pixel eines Clusters ausgelesen wurden, der Ladungsschwerpunkt bestimmt wird. Dieser liefert im Vergleich zu einer rein binären Auslese eine bessere Auflösung. Zur Gewichtung der einzelnen Pulshöhen ist ein linearer Zusammenhang zwischen Detektorsignal und deponierter Energie gewünscht, jedoch ist dieser Zusammenhang vielmehr hyperbolisch [Dam09]. Im Detail bedeutet dies, dass speziell für sehr große Eingangssignale das Detektorsignal in Sättigung geht, was aber kein Problem darstellt, da die im Experiment entstehenden Teilchen keine entsprechend großen Eingangssignale erzeugen. Mit Röntgenkalibrationen soll im Bereich niedriger Energien ein möglichst linearer Zusammenhang zwischen Eingangs- und Detektorsignal bestimmt werden. Da die Kalibration einen entscheidenden Einfluss auf die Gewichtung unterschiedlicher Pulshöhen und somit auf die Ortsauflösung hat, ist eine detailierte Untersuchung der Signalauslese und damit verbundener Effekte gerechtfertigt.

Diese Arbeit befasst sich mit Röntgenkalibrationen, die Anwendung bei der Evaluation der zu produzierenden Module finden werden. Zunächst werden Analysen der gemessenen Detektorsignale und Untersuchungen bezüglich der Auswirkungen des Untergrunds vorgestellt. Zentraler Punkt der Studien ist jedoch der Einfluss diverser experimenteller Parameter wie Temperatur, Bestrahlungsrate und des sogenannten „Stretched Clock Cycle“ (*scc*) auf die Pulshöhe. Der Parameter *scc* dient vor allem bei Messungen mit niedrigen Teilchenraten zur Verbesserung der Statistik durch Vergrößerung des aktiven Zeitintervalls der Datennahme. Zusätzlich gibt es zwei verschiedene Methoden zur Messung des Detektorsignals, die miteinander verglichen werden. Die Spektrummethode basiert darauf, die gemessenen Spektren mit einer Gaussfunktion anzupassen, wobei der Mittelwert des Anpassung dem Signal entspricht. Bei der Schwellenmethode werden die Signale mit einer einstellbaren Komparatorschwelle in jeder einzelnen Pixelzelle (pixel unit cell, PUC[1]) verglichen [Trü08]. Es wird die Schwelle bestimmt, welche der gemessenen Ladung entspricht. Anschließend werden steigende ROC-interne Kalibrationsignale verwendet, zur Ermittlung, welches dieser Kalibrationssignale der zuvor bestimmten Schwelle entspricht. Das Prinzip der Schwellenmethode beruht darauf, dass die erzeugte Ladung allein mit den PUC-Komponenten bis zum Komparator bestimmt wird, alle Einflüsse der sich anschließenden Auslesekette können daher nicht berücksichtigt werden.

Alle durchgeführten Untersuchungen befassen sich ausschließlich mit dem neuentwickelten Auslesechip PSI46dig. Allerdings werden an einigen Stellen Vergleiche mit Ergebnissen des aktuell verwendeten Auslesechips PSI46V2 gegeben.

Zur Durchführung der Kalibrationen wurden zwei Teststationen verwendet, die beide auf dem Prinzip beruhen, die Einzelchipmodule mit Röntgenstrahlung definierter Energie zu bestrahlen. Einzelchipmodule beinhalten im Gegensatz zu den eigentlichen Modulen nicht 16 sondern nur einen Auslesechip. Erzeugt wird die Röntgenstrahlung durch Anregung bestimmter Targetmaterialien und dem entsprechenden K_α-Übergang in der Elektronenhülle. Zur Datenauslese werden PSI46-Testboards und die Softwarepakete psi46expert und TakeData verwendet, wobei die Softwarepakete auf Linux-basierten PCs ausgeführt werden. Unterschiede in den Teststationen gibt es in der Art und Weise, wie die Targetmaterialien angeregt werden und hinsichtlich der vorhandenen Kühlung der Einzelchipmodule. Die Röntgenröhren-Teststation regt die austauschbaren Targets (Eisen, Kupfer, Zink, Molybdän, Silber, Indium, Zinn, Neodym) mit Hilfe kontinuierlicher Röntgenstrahlung an. Dabei wird Röntgenstrahlung mit charakteristischer Energie emittiert und trifft auf den Sensor des Einzelchipmoduls. Ein Vorteil dieser Teststation ist, dass dank der leistungsstarken Röntgenröhre die zur Verfügung stehenden Raten groß und variabel wählbar sind. Mit der zur Verfügung stehenden Kühlung sind stabile Temperaturen im Bereich der Raumtemperatur möglich. Die zweite Teststation verwendet eine ^{241}Am-Quelle und deren emittierten Photonen zur Anregung der verfügbaren

[1] In einer PUC sind alle elektronischen Komponenten zur Signalverarbeitung für einen Pixel untergebracht

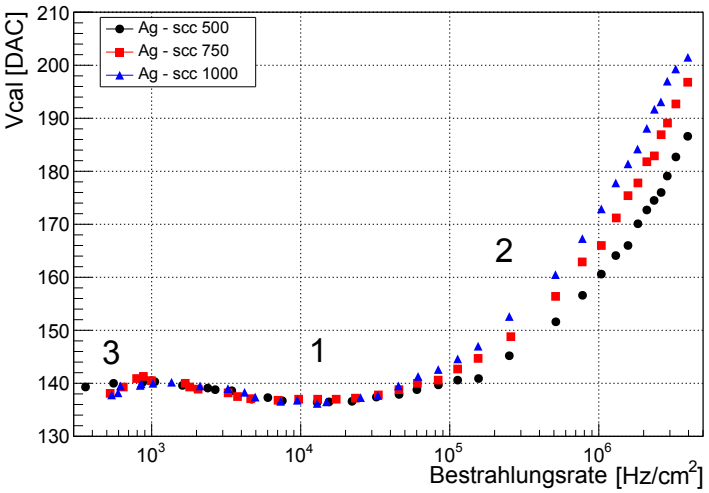

Abbildung 1: Ratenabhängigkeit des PSI46dig-Detektorsignals für ein Silbertarget und verschiedene *scc*-Werte. Das Signal lässt sich in drei Bereiche trennen: eine Signalsenke (1) im Bereich von 10-20 kHz/cm^2, einen sehr steilen Anstieg (2) oberhalb von 100 kHz/cm^2 und einen Signalrückgang (3) für Bestrahlungsraten kleiner als 100 kHz/cm^2. Während die Positionen der drei Bereiche stabil sind, schwankt die absolute Höhe je nach gewähltem *scc*-Wert.

Targetmaterialien (Cu, Rb, Mo, Ag, Ba, Tb). Im Gegensatz zur Röntgenröhren-Teststation verfügt diese nur über geringe Bestrahlungsraten, hat jedoch dank einer Wasserkühlung der Peltier-Elemente einen frei wählbaren Temperaturbereich von $-30°$C bis 20°C.

Durch eine detaillierte Bestimmung und Analyse des Untergrunds in Teststationen wurde eine Korrektur der gemessenen Spektren ermöglicht. Allerdings zeigte sich, dass auf eine Korrektur der Spektren verzichtet werden kann, da die Genauigkeit und Zuverlässigkeit der Anpassung der Gaussfunktion auch ohne Korrektur die gleichen zuverlässigen Werte liefert, sofern vernünftige Anpassungs-Grenzen gewählt werden.

Im Rahmen dieser Arbeit wurden folgende fünf Abhängigkeiten beobachtet, detailliert beschrieben und interpretiert.

In Abbildung 1 ist die Ratenabhängigkeit der Pulshöhe zu sehen, welche in drei Regionen unterteilt wurde. In Region 1 ist eine Signalsenke bei Bestrahlungsraten von $10 - 20$ kHz/cm^2 beobachtet worden. Diese tritt unabhängig vom Targetmaterial beziehungsweise der Energie der Photonen und vom gewählten *scc*-Wert immer bei gleichen Raten auf. Verantwortlich für diese Senke ist der Speicherkondensator im Abtast-Halte-Glied der PUC. Das Detektorsignal wird in diesem Kondensator durch den analogen Spannungsbereich der PUC gespeichert, jedoch wird die Auslese des Kondensators durch den digitalen Spannungsbereich versorgt. Während der Analogstrom und somit die Analogspannung sowie das gespeicherte Signal nahezu konstant sind, zeigt der Digitalstrom im Bereich der Signalsenke eine Änderung. Das Auslesen des Kondensators geschieht über einen sogenannten single-ended-Verstärker, da dessen Versorgungsspannung ratenabhängig ist, fällt das Signal ab. Dieser Effekt ist bekannt als *power supply rejection ratio*. Die Signalsenke wurde bereits beim PSI46V2 beobachtet, war dort jedoch deutlich ausgeprägter. Die Reduzierung wurde durch eine Änderung in der Spannungsversorgung des Verstärkers erzielt.

Für Bestrahlungsraten oberhalb von 100 kHz/cm^2 (Abbildung 1, Region 2) zeigt das Detektorsignal einen steilen Anstieg. Im Vergleich dazu zeigte der aktuelle ROC PSI46V2 für hohe Raten einen Signalabfall. Genauso wie die Signalsenke tritt dieses Verhalten unabhängig von Targetmaterial und *scc* auf, wobei der Effekt für steigende *scc*-Werte stärker wird. Dieses

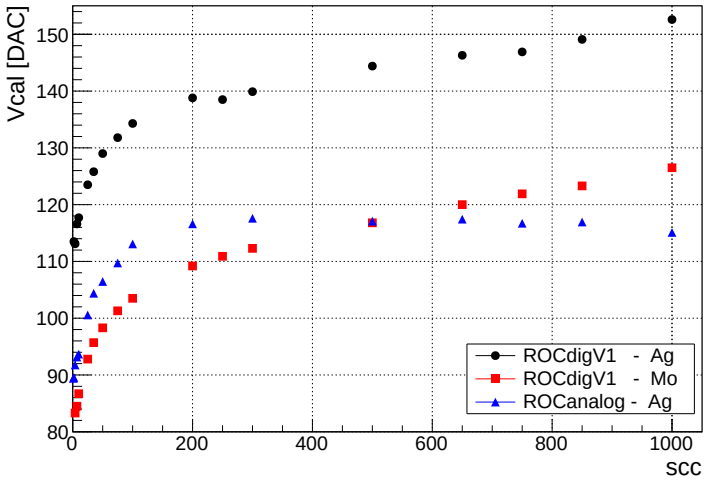

Abbildung 2: *scc* Abhängigkeit der Pulshöhe für den aktuell verwendeten analogen ROC PSI46V2 [Hos12, p.70] und den neuen digitalen ROC PSI46digV1. Die beobachteten Pulshöhen für Silber und Molybdän zeigen das gleiche Verhalten. Zunächst wächst das Detektorsignal – mit steigendem *scc* – steil an, ab einem *scc* Wert von etwa 200 steigt es jedoch nur noch moderat an. Für den ROC PSI46V2 ergibt sich ein ähnliches Verhalten, jedoch fällt das Signal für hohe *scc* Werte wieder ab.

Verhalten lässt sich allerdings nicht durch eine Ratenabhängigkeit des Digitalstrom erklären, da dieser nur in Region 1 nicht konstant ist (der Analogstrom ist ohnehin für alle Bestrahlungsraten konstant). Da Messungen mit der Schwellenmethode keinerlei Ratenabhängigkeit zeigten, müssen Komponenten der PUC nach dem Komparator für den Anstieg verantwortlich sein. Um einen zu starken Einfluss der Ratenabhängigkeit im Kalibrationsprozess zu vermeiden, sollte bei Raten kleiner 200 $\mathrm{kHz/cm^2}$ gemessen werden.

Zusätzlich gibt es einen Abfall der Pulshöhe für Bestrahlungsraten unterhalb von 0.6-1 $\mathrm{kHz/cm^2}$ (Abbildung 1, Region 3), der ebenfalls für andere Targets auftritt. Zwar ist es je nach Target möglich, mit der vorhandenen Ausrüstung noch bei kleineren Raten zu messen, allerdings ist dieser Bereich nicht mehr interessant für die Kalibration, da die Bestrahlungsraten zu gering sind, um eine gewünschte Mindestanzahl an detektierten Photonen zu erhalten.

Eine weitere Abhängigkeit des Detektorsignals zeigt sich bereits in Abbildung 1. Wie in Abbildung 2 zu sehen ist, zeigt die gemessene Pulshöhe einen starken Anstieg für größere werdende *scc*-Werte. Vor allem für *scc*-Werte bis zu 200 ist der Anstieg sehr steil und flacht erst danach leicht ab. Auch dieses Verhalten ist unabhängig vom verwendeten Targetmaterial und wurde in ähnlicher Form schon beim PSI46V2 beobachtet [Hos12]. Möglicherweise hängt dieser Effekt mit einer – bisher nicht bestätigten – *scc*-Abhängigkeit der Signalabtastzeit zusammen, jedoch gibt es bislang keine Möglichkeit, dies näher zu untersuchen.

Das letzte unerwartete Verhalten wurde in einer Pulshöhen-Abhängigkeit von den WBC/TCT Parametern beobachtet. Diese Parameter sind jedoch nur dafür verantwortlich, zu welchem Taktzyklus ausgelesen werden soll und dürften keinen Einfluss auf die Pulshöhe haben. Allerdings zeigt sich, dass die Pulshöhe je nach WBC/TCT-Wert um bis zu 5 Vcal-Einheiten schwankt, wobei statistische Schwankungen als Ursache ausgeschlossen werden konnten. Wie in Abbildung 3 zu sehen ist, gibt es kein erkennbares Muster in Form einer Frequenz oder Ähnlichem. Auch ist die Form der Verteilung für zwei verschiedene ROCs (beide Version PSI46digV1) unterschiedlich. Für die Röntgenkalibrationen bedeutet dies, dass die WBC/TCT

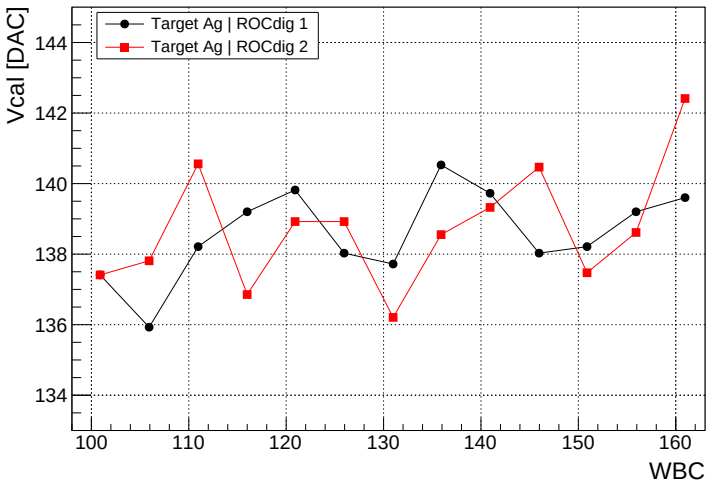

Abbildung 3: TCT/WBC-Abhängigkeit des Detektorsignals des PSI46digV1 für zwei ROCs mit einem Silbertarget. Die gemessenen Pulshöhen schwanken in einem Bereich von 5 Vcal-Einheiten, jedoch ohne erkennbare Frequenz. Außerdem zeigen die beiden ROCs verschiedene Verläufe, also handelt es sich zudem um einen ROC-abhängigen Effekt. Zuvor konnten statische Schwankungen als Grund ausgeschlossen werden.

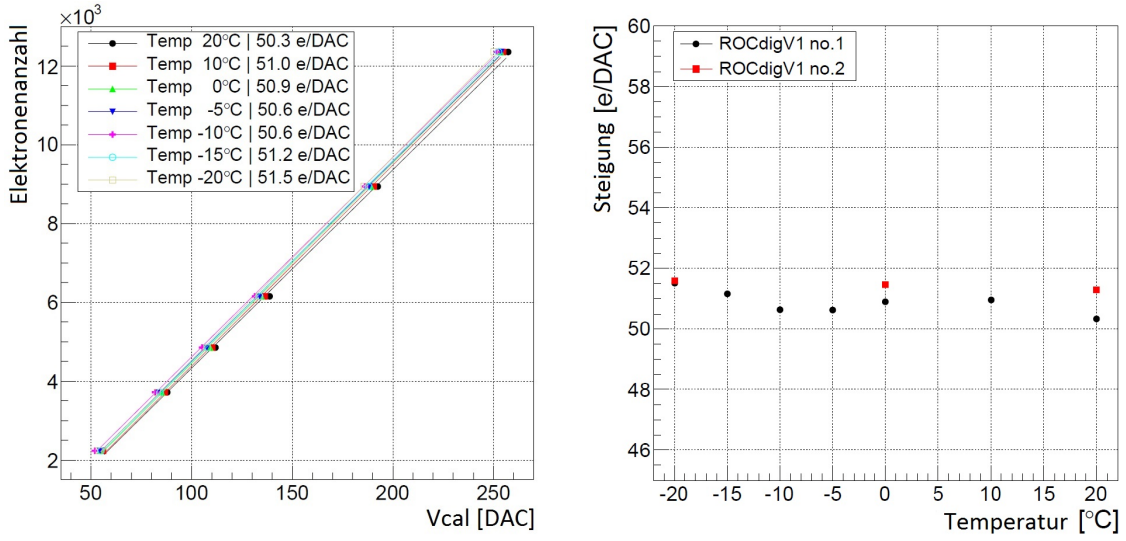

(a) Kalibrationsgeraden (b) Steigungen der Kalibrationsgeraden

Abbildung 4: Temperaturabhängigkeit der Pulshöhe des PSI46digV1. Die angegebenen Temperaturen wurden auf der Sensoroberfläche gemessen. In (a) sind Kalibrationsgeraden für verschiedene Temperaturen gegeben, wobei keine Temperaturabhängigkeit erkennbar ist. Zwar gibt es eine geringe Verschiebung, jedoch ohne Trend. In (b) ist die Temperaturunabhängigkeit des PSI46digV1 verdeutlicht: die Steigungen aller Kalibrationsgeraden liegen um 50 e/DAC.

Parameter nicht verändert werden sollten, um die Auswirkungen dieses Effekts zu vermeiden.

Zusätzlich konnte noch eine andere Beobachtung gemacht werden, die jedoch nicht unerwartet auftrat und zudem keine Abhängigkeit von einem experimentellen Parameter aufweist. So zeigt sich in Abbildung 4 (a), dass die Kalibrationsgeraden keine Temperaturabhängigkeit aufweisen. Interessant ist dies, da der Vorgänger ROC PSI46V2 noch eine starke Temperaturabhängigkeit zeigte, was zur Folge hatte, dass sich die Steigungen der Kalibrationsgeraden bis zu 30 % unterschieden. Im Vergleich dazu ist in Abbildung 4 (b) zu sehen, dass die Steigungen der Kalibrationsgeraden des PSI46dig nahezu konstant sind. Ein Vorteil, der sich hieraus ergibt ist, dass zur Kontrolle der Funktionalität der am KIT zu produzierenden Module ein Test bei Raumtemperatur ausreichend ist.

Aus den detaillierten Beschreibungen der beobachteten Effekte ergeben sich zum einen neue Erkenntnisse bezüglich der Signalauslese, zum anderen lassen sich aber auch Empfehlungen für die Röntgenkalibration geben. Außerdem konnte eine Übersicht gegeben werden, wo Unsicherheiten in den Messungen auftreten, wie groß diese sind und inwiefern sie sich verringern oder sogar gänzlich vermeiden lassen. Somit lässt sich aus dieser Arbeit ein Leitfaden für die benötigte Energiekalibration der für das Phase-I-Upgrade zu produzierenden Module ableiten.

Contents

List of Figures

List of Tables

1. Introduction

On July 4, 2012 the CMS (**C**ompact **M**uon **S**olenoid) and the ATLAS (**A** **T**oroidal **L**HC **A**pparatu**s**) Collaborations presented results with a major breakthrough showing for the first time the discovery of a new boson [A$^+$12, C$^+$12]. More recent results – from March 8, 2013 – of the CMS Collaboration indicate that it is a Higgs-like boson at a mass of about 125 GeV/c^2 with a combined local significance of five standard deviations [CMS13c]. It is very likely the Higgs Boson which was postulated by Peter Higgs [Hig64a, Hig64b] and others [EB64, GHK64] in 1964 as an excitation of the Higgs field. The great opportunity of the Higgs boson and the associated Higgs field is that its discovery would explain the origin of mass of elementary particles, an essential open question within the Standard Model of particle physics (SM). The Standard Model is a theory characterising the fundamental particles and the interactions between them. It is able to describe three of the four fundamental interactions – the electromagnetic, the weak and the strong interactions – but not gravitation (see e.g. [Gri08]). The description of nature by the Standard Model is excellent even though there are observations and theoretical expectations it cannot explain.

With the discovery of a Higgs boson the CMS and ATLAS experiments are a huge success, however, the investigation of this particle is by no means finished. For this purpose many more proton-proton collisions have to be provided by the LHC since the production plus associated detection properties of the possible Higgs boson are relatively small. In consequence, the LHC will undergo major consolidation work during a long shutdown in 2013/14 to increase the centre-of-mass energy $\sqrt{s}$ up to 14 TeV while the luminosity will reach $\mathcal{L} = 2 \times 10^{34}\,\mathrm{cm}^{-2}\mathrm{s}^{-1}$ which corresponds to twice the design luminosity [D$^+$12]. As a result the number of simultaneous collisions, the so called pile-up, will increase from 25 up to 50. For the detectors of the experiments this means harsher conditions to deal with concerning the readout speed and radiation hardness due to the increased particle rate. As the CMS pixel detector is the innermost part and closest to the interaction point it is the most affected component of the CMS detector. Therefore the entire pixel detector will be replaced at the end of 2016 to maintain its high efficiency in terms of trajectory and vertex reconstruction of charged particles.

For the upgrade a new readout chip (ROC) containing extended buffers and digital readout has been developed to increase the readout speed and to meet the increased particle rate. Further an additional layer will be mounted in the barrel region and in each endcap to improve the covered sensitive volume [D$^+$12]. Half of the modules – the smallest pixel detector subunit – of the new barrel layer four will be produced at Karlsruhe Institute of Technology (KIT). The

fully assembled modules will be qualified by calibration measurements with monochromatic X-rays.

This thesis deals with the calibration process of the ROC PSI46dig. Although the pixel detector is not intended for energy-measurements the calibration is required as charge sharing is exploited to improve the resolution [CMS10]. Charge sharing is the effect when particles traverse the sensor and deposit charge in more than one pixel because of the Lorentz drift of charge carriers in the magnetic field of the CMS solenoid. Reading out the collected charge and calculating the centre of gravity of the charge distribution of the pixel clusters determines the penetration point of the particle. Improving the resolution is an advantage for tracking and vertex reconstruction which in turn is beneficial for the physics objectives of the entire detector. Therefore it is important to achieve reliable charge sharing which requires a linear relation between initially deposited energy and measured detector signal. A non-linear relation would lead to wrong ratios between different signal heights and hence degrade the resolution. This motivates detailed investigations of the calibration procedure.

The calibration process relies on monochromatic X-rays of known energy as reference signals. They are generated from the K_α transition of electrons in atomic shells when some target material is excited by photons. The calibration curve is obtained by reading out the detector signals for different targets and plotting them together with the theoretical K_α transition energy. Regarding the module production it is of great interest to gain experience in the calibration process, obtain performance know-how of the new readout chip and to determine reasonable X-ray calibration procedures for the module testing.

At first this thesis introduces basic elements like the Large Hadron Collider and the Compact Muon Solenoid experiment in Chapter 2. The physics objectives with the associated detector requirements and the structure of the CMS subdetectors are described in detail. Chapter 3 presents the central component of this thesis, the CMS pixel detector. First the working principle of semiconductor detectors and their most important properties are explained. Afterwards the CMS pixel detector is introduced where the readout chip and the changes within the Phase I Upgrade are extensively described. It is important to obtain a detailed understanding of the readout chip as it has a large influence on the detector performance and for the interpretation of measurements and results of this work. A comparison of the pixel detector before and after the Phase I Upgrade is also given since this thesis deals with the new ROC and compares its performance to the current used ROC. In Chapter 4 the motivation for the X-ray calibration is given and the equipment consisting of test samples, test boards and test stations is described followed by the pre-calibration, an initial routine before X-ray calibrations are performed. Finally two different methods of data acquisition are explained and compared and an introduction of the recorded rate is given. Chapter 5 is the central part of this thesis which focuses on the measurements performed as well as the results obtained in this thesis and conclusions of the X-ray calibrations. The studies include a characterisation of the background and spectra obtained from a Gaussian fitting procedure. The influence of experimental parameters such as temperature, irradiation rate and readout timing on the detector signal are investigated. Finally an overview of the uncertainties associated with the above influences is presented. A summary of the results and conclusions as well as an outlook for further measurements is given in Chapter 6.

2. The LHC and the CMS Experiment

"When we're born, we want to know why the stars shine. We want to know why the sun rises." – *Michio Kaku*. The curiosity of mankind was always the engine to step up effort and to design greater experiments to draw the secrets from nature.

Excellent examples of human curiosity are the construction of the Large Hadron Collider (LHC) and its experiments like the Compact Muon Solenoid (CMS). This chapter will introduce the LHC as well as CMS since this diploma thesis will deal with the readout chip of the pixel detector of the Compact Muon Solenoid experiment.

2.1 The Large Hadron Collider

In December 1994 the council of the European Organisation for Nuclear Research (CERN[1]) approved the construction of the Large Hadron Collider (LHC) [B$^+$04], the largest and most powerful particle collider ever made. The LHC is located at CERN near Geneva while its centrepiece, the 27 km long storage ring, is on average about 100 m below the surface of the earth. The particles accelerated in the LHC are protons or heavy ions which travel in two counter-rotating beams. According to its design, the LHC should be able to provide proton-proton collisions with a centre-of-mass energy $\sqrt{s}$ of 14 TeV (this corresponds to 0.999999991 times the speed of light [Lef09, D$^+$12]). The LHC went into operation in September 10, 2008 but already nine days later a defective electrical connection entailed in a magnet quench and an explosion of a helium cooling tank [F$^+$12]. Recommissioning took more than a year and the first proton-proton collisions were observed on November 23, 2009, [CER09].

Two very important values which qualify a particle accelerator are the instantaneous and the integrated luminosity. The instantaneous luminosity provides the event rate of an accelerator with – in case of the LHC – two counter-rotating beams and is defined as follows:

$$\mathcal{L} = \frac{N_a \cdot N_b \cdot j \cdot f}{A}. \tag{2.1}$$

Thereby is j the number of bunches, N_a and N_b are the numbers of particles of the two colliding bunches, f is the bunch crossing frequency and A is the beam cross-section at the interaction point [Pov04]. In the original LHC design an instantaneous luminosity of $\mathcal{L} = 1 \times 10^{34}\text{cm}^{-2}\text{s}^{-1}$ is given, however it is planned to reach twice this value before the

[1] Acronym: CERN derives from the French name of the council which was in charge of its foundation, the **C**onseil **E**uropéen pour la **R**echerche **N**ucléaire

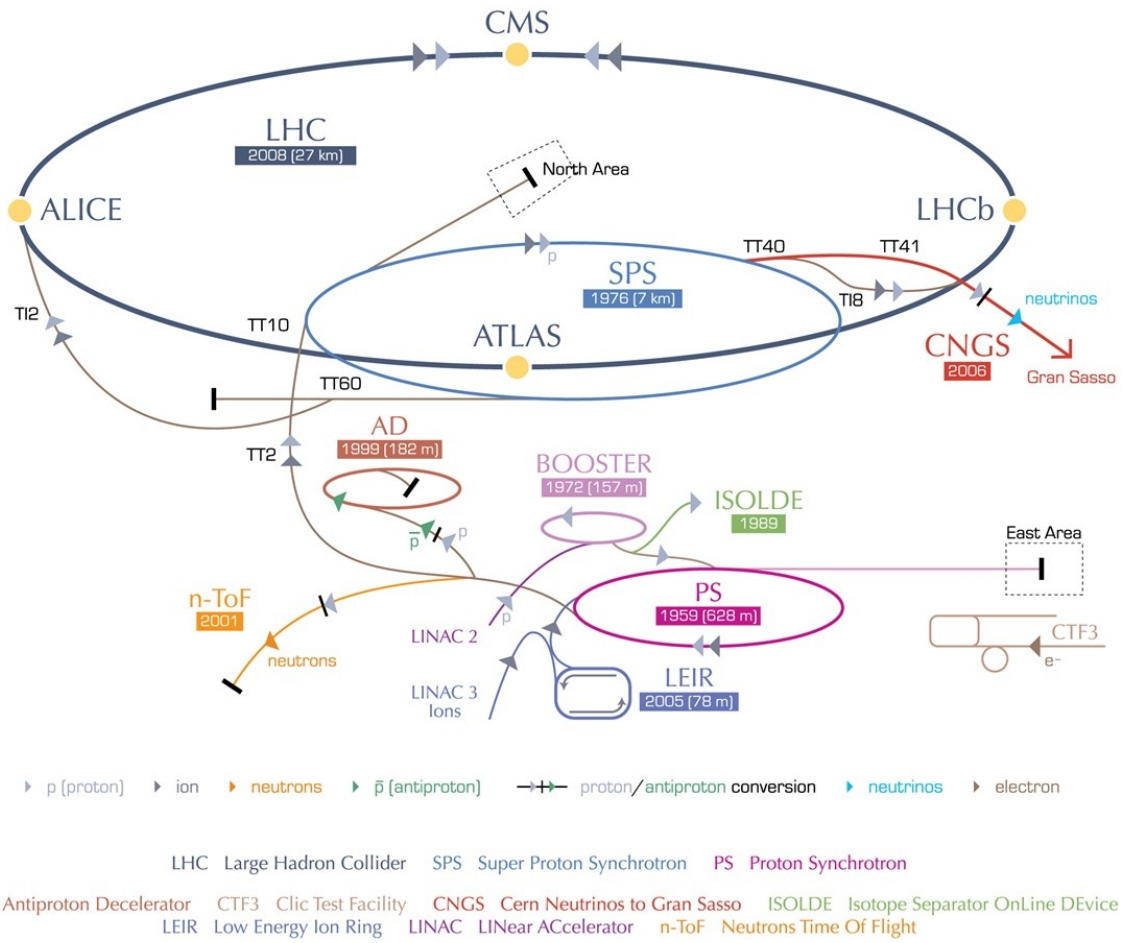

Figure 2.1: Overview of the CERN accelerator complex including the LHC and the four main experiments. Protons and lead ions have to pass several pre-accelerators before they are injected into the LHC and reach their final energy [Lef09].

next extended technical stop in 2016/2017. The integrated luminosity is the instantaneous luminosity integrated over time.

Before protons (or heavy ions) are brought to collision they have to pass several pre-accelerators to reach their final energy. Protons start their journey from a bottle of hydrogen. After the electron is separated from the hydrogen the remaining proton is accelerated in the LINAC2 to an energy of 50 MeV and then injected into the Proton Synchrotron Booster (PSB). Within the PSB the protons reach an energy of 1.4 GeV before they are transferred into the Proton Synchrotron (PS). There they achieve 25 GeV are then injected into the Super Proton Synchrotron (SPS) and accelerated to an energy of 450 GeV. In a last step they are transferred into the LHC where they reach the final energy, the highest so far was 4 TeV. A schematic of the accelerators involved is shown in figure 2.1.

The LHC – which is not a perfect circle – is equipped with 9593 magnets out of which are 1232 Nb-Ti (niobium-titanium) main dipole magnets with 154 in each of the eight arcs to bend the beam and 392 main quadrupole magnets to keep the beam focused in order to minimise its spot as far as possible at the interaction point. Keeping 7 TeV protons on track require magnet fields up to 8.33 T which in turn requires dipole operating temperatures of −271.3 °C (1.9 K). Achieving such a low temperature is obtained by exploiting the superfluid state of helium with its very high thermal conductivity. Accelerating protons in the entirely filled LHC is accomplished by eight superconducting cavities per beam providing 2 MV at 400 MHz. They also have the indispensable task to ensure that the particles stay tightly

bunched to achieve the highest possible collision rate. As soon as the LHC is entirely filled there are 2808 bunches in the ring. A bunch (of protons) consists of 10^{11} protons and is a few centimetres long and millimetres wide as long as it is far away from the interaction points. Once a bunch reaches an interaction point it is squeezed to roughly 16 µm in diameter to increase the collision rate. The minimal bunch spacing is 25 ns which corresponds to a distance between two consecutive bunches of approximately 7 m [Lef09, B$^+$04].

2.1.1 LHC Experiments

The experiments are located at four intersection points where the stored protons respectively heavy ions are brought to collision. There are four main experiments – CMS, ATLAS, LHCb and ALICE – each located in its on cavern.

The Large Hadron Collider beauty (LHCb) experiment is a single-arm (measuring only on one side of the interaction point) spectrometer [LHC08a] exploring decays containing b- or c-quarks [LHC98]. The special single-arm design is appropriate since b- and $\bar{b}$-hadrons are mainly produced in the same direction at high energies. LHCb's physics programme contains the precise measurement of the CP-violation and the validation of the Standard Model of particle physics.

ALICE is the acronym for A Large Ion Collider Experiment using a cylindrically symmetrical detector. As the name suggests, ALICE deals basically with heavy ions, in case of the LHC lead ions (up to now). One main objective of ALICE is the investigation of quark-gluon plasma which is an expected new state of matter at very high energy density and temperature [ALI08].

In contrast to ALICE the CMS experiment and the ATLAS experiment (A Toroidal LHC Apparatus) are optimised for proton-proton collisions. CMS is explained in section 2.2 while further information concerning ATLAS is available in [ATL08].

Additionally there are three smaller experiments. One aim of TOTEM[2], which is located in the CMS cavern, is to measure the proton size with an accuracy never seen before [TOT08]. LHCf[3] is placed in the ATLAS cavern and measures particles in proton-proton collisions extremely close to the beam line to study forward particle production relevant for extensive air showers initiated by cosmic rays [LHC08b]. The last experiment is MoEDAL[4] which seeks for magnetic monopoles and other highly ionising stable – or pseudo-stable – massive particles [MoE09].

2.2 The CMS Experiment

The Compact Muon Solenoid – 21.6 metres long, 14.6 metres in diameter and with a weight of 12500 tons – was designed to investigate many facets of physics, including physics at the TeV scale, the search for the Higgs Boson and physics beyond the standard model [CMS06]. CMS as well as ATLAS – each located at one of the four interaction points of the LHC – are the two large general-purpose detectors at CERN with similar goals. These two detectors were developed independently and hence use different technologies to achieve their goals. This redundancy was desired since it has the advantage to provide independent proof of discoveries.

2.2.1 Physics Objectives

The main physics objectives of CMS are the search for the Higgs Boson, the performance of even more precise measurements of known Standard Model processes and the search for

[2] Acronym: **TOT**al **E**lastic and Diffractive Cross Section **M**easurement
[3] Acronym: **L**arge **H**adron **C**ollider **f**orward
[4] Acronym: **Mo**nopole and **E**xotics **D**etector **A**t the **L**HC

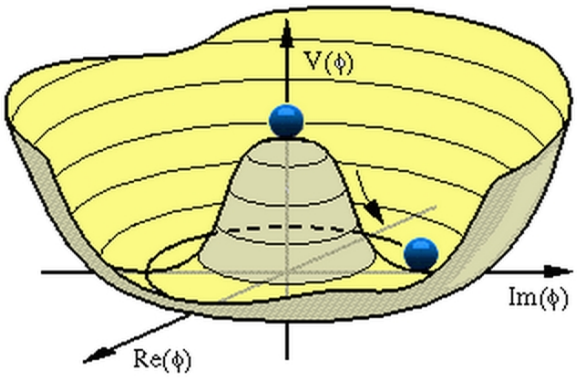

Figure 2.2: Mexican hat-like shape of the Higgs potential. The spontaneous symmetry breaking is indicated [CMS13a].

evidence of physics beyond the Standard Model. The Standard Model of particle physics (SM) is a theory characterising the fundamental particles and the interactions between them. It is able to describe three of the four fundamental interactions – the electromagnetic, the weak and the strong – but not gravitation (see e.g. [Gri08]).

One primary objective is the investigation of the electroweak symmetry breaking mechanism. This topic is of great interest since the Standard Model does not explain the origin of mass. In 1964 Peter Higgs [Hig64a, Hig64b] and others [EB64, GHK64] introduced a theory which is able to explain the phenomenon of mass via the so called Higgs mechanism. Within this theory a scalar background in form of an isospin doublet of complex fields is described. The corresponding potential has the shape of a Mexican hat as depicted in figure 2.2.

When the ground state is occupied the local symmetry is spontaneously broken – visible in figure 2.2 – and the electroweak gauge bosons Z ($91.2\,\mathrm{GeV/c^2}$) and $\mathrm{W^{\pm}}$ ($80.4\,\mathrm{GeV/c^2}$) [SS07] receive mass while the photon stays massless. Three of the four degrees of freedom of the Higgs field are absorbed and the last one corresponds to the Higgs boson. The couplings of this particle to all other particles grow with the masses of the particles while only the mass M_H of the Higgs boson is unknown. Therefore the search for the Higgs boson is of such big interest as the discovery would deliver all production and decay properties of the Standard Model Higgs boson.

There are four relevant Higgs production mechanisms at the LHC: gluon fusion, vector boson fusion and associated production with $\mathrm{W^{\pm}}$, Z or top quark (see figure 2.3). The main production mechanism at the LHC in the interesting Higgs mass range is gluon fusion which can also be seen from the production cross sections presented in figure 2.4 (a) [CMS07].

Before first results were obtained the Higgs decay mechanisms were divided into two regions depending on the Higgs mass M_H (see figure 2.4 (b)). The dominant decays modes are $b\bar{b}$ or $\tau^+\tau^-$ for $M_H \lesssim 135\,\mathrm{GeV/c^2}$ and two $\mathrm{W^{\pm}}$ or two Z bosons for $M_H \gtrsim 135\,\mathrm{GeV/c^2}$.

From theory and previous experiments at the LEP[5] upper and lower bounds for the Higgs boson mass M_H were known. For instance the experiments at LEP2 obtained a lower bound of $114\,\mathrm{GeV/c^2}$ at 95% confidence level (CL) for the Higgs mass M_H [LEP01] while natural arguments gave a theoretical upper bound at around $1\,\mathrm{TeV/c^2}$ [Esp96]. Further the experiments at Tevatron were able to exclude masses between $147\,\mathrm{GeV/c^2}$ and $180\,\mathrm{GeV/c^2}$ [Phy12] at 95% confidence level while an upper limit of $162\,\mathrm{GeV/c^2}$ at 95% CL for the Higgs mass was obtained by [F$^+$08].

On July 4, 2012 the CMS and the ATLAS collaborations presented their first results with a major breakthrough showing the discovery of a new boson. Latest results – from March 8,

[5] Acronym: **L**arge **E**lectron-**P**ositron Collider

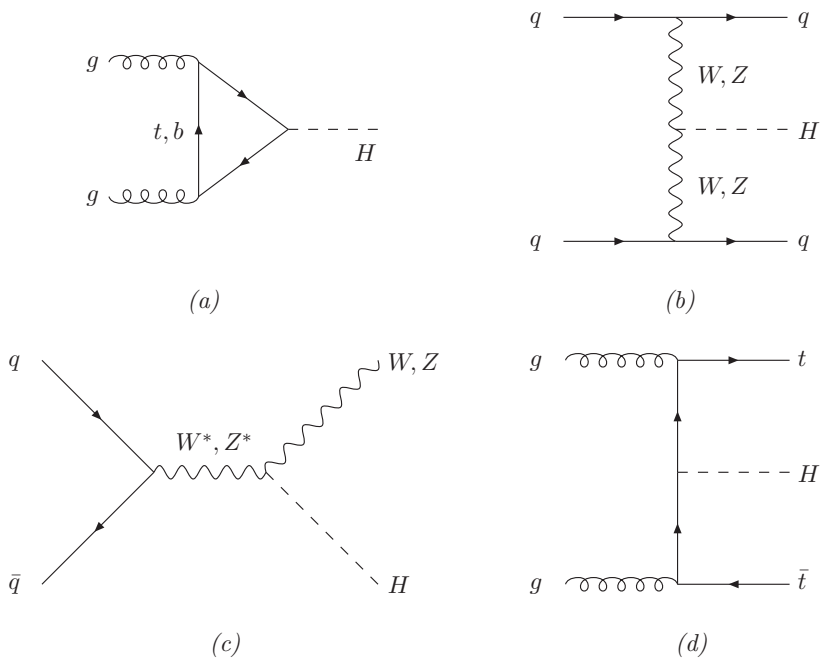

Figure 2.3: Higgs production mechanisms at the LHC. Namely they are (a) gluon fusion, (b) vector boson fusion, (c) associated production with $W^{\pm}$, Z and (d) associated production with top-quarks [CMS07].

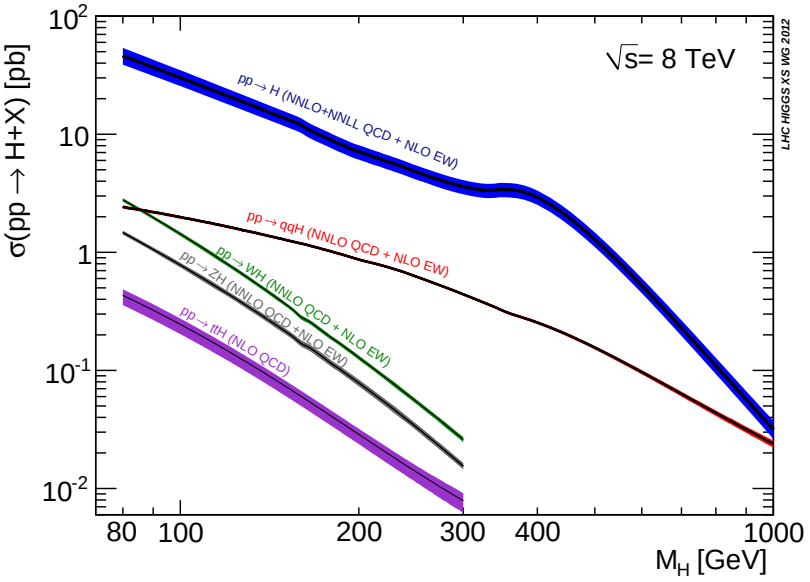

Figure 2.4: LHC production cross sections of the Higgs boson as a function of the Higgs mass M_H. Gluon fusion – illustrated in blue – is dominating the whole plotted range [LDM+11].

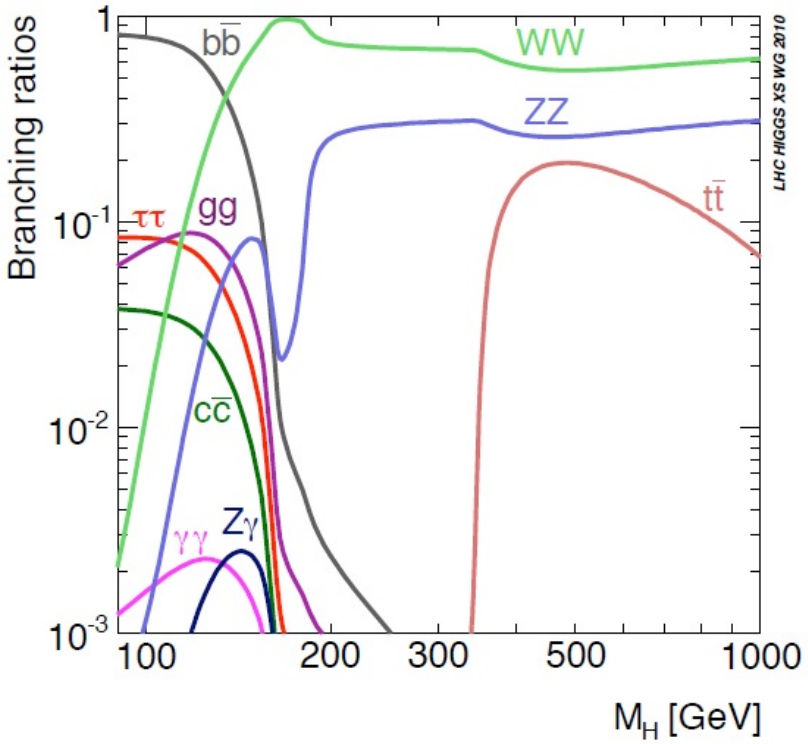

Figure 2.5: Branching ratios of the main decay modes of the SM Higgs boson as function of the Higgs mass M_H [LHM+13].

2013 – of the CMS Collaboration indicate that it is a Higgs-like boson at a mass of about $125\,\mathrm{GeV/c^2}$ with a combined local significance of five standard deviations. The excess of the two high resolution channels $\mathrm{H} \to \gamma\gamma$ and $\mathrm{H} \to \mathrm{ZZ} \to 4\ell$ delivers the best results with a mass estimation of $125.3 \pm 0.4 \pm 0.5\,\mathrm{GeV/c^2}$. The integrated luminosity of the data samples corresponds to $5.1\,\mathrm{fb}^{-1}$ at $\sqrt{s} = 7\,\mathrm{TeV/c^2}$ and up to $5.3\,\mathrm{fb}^{-1}$ at $\sqrt{s} = 8\,\mathrm{TeV/c^2}$ [CMS13c]. ATLAS also presented results on March 8, 2013 showing an excess of events at $125.5\,\mathrm{GeV/c^2}$ [ATL13] which is in a good consent with the CMS results. However more data is required to verify whether the observed particle is the SM Higgs boson.

The search for the Higgs boson is – although it is probably the most famous one – not the only objective. The Standard Model is a very accurate theory even though there are observations and theoretical expectations it cannot explain. For instance it does not consider dark matter [Moo94], the mass of neutrinos which is a conclusion of the neutrino oscillation [CGL09] or – as previously mentioned – gravitation. An attempt to give answers to open questions of the Standard Model is a theory called Supersymmetry (SUSY). The name Supersymmetry derives from the additional symmetry that each boson has a fermionic superpartner, the so called gauginos, and each fermion has a bosonic superpartner, the so called squarks [WZ74]. It is expected that supersymmetric particles decay – due to the large mass and the associated short lifetime – in cascades into the stable Lightest Supersymmetric Particle (LSP), a possible candidate for dark matter. As the LSP should barely interact with SM particles it should mostly leave the detector. In this case it could be measured via the missing transverse energy $E_{\mathrm{T}}^{\mathrm{miss}}$.

2.2.2 Detector Requirements

The following requirements have to be considered according to the LHC physics objectives [CMS06]:

- The Higgs decay mode into four leptons requires good muon identification and momentum resolution for a pseudo rapidity[6] range of $|\eta| < 2.5$, a good mass resolution of about 1% at $100\,\mathrm{GeV/c^2}$ as well as a precise charge measurement of muons up to $p = 1\,\mathrm{TeV/c}$.
- Good charged particle momentum resolution and precise vertex reconstruction requires a pixel detector with fine spatial resolution near the interaction point in the centre of the detector.
- The Higgs decay mode into two photons requires a good electromagnetic energy and mass resolution of about 1% at $100\,\mathrm{GeV/c^2}$ with a geometric coverage of $|\eta| < 2.5$.
- To measure the missing transverse energy $E_\mathrm{T}^\mathrm{miss}$ as precisely as possible the hadron calorimeter has to absorb the hadrons completely including a good energy resolution.

2.2.3 Detector Layout

The CMS detector is a barrel-and-endcap like design consisting of different layers which exploit the various properties of the particles emerging from proton-proton and heavy ion collisions to measure their energies and momenta. To achieve good angular resolution each of the different layers has a barrel and an endcap sector (see figure 2.6). Further this design provides the opportunity to exchange single parts of the detector or to have better access to several parts during maintenance periods.

Figure 2.7 shows a slice of the CMS detector. The different sections of the detector – starting from the beam pipe – are the silicon tracker, the electromagnetic calorimeter, the hadron calorimeter, the superconducting solenoid magnet and at last the muon chambers embedded in the iron magnet return yoke. The slice also shows exemplary tracks of different particles traversing the detector and interacting in the different sections.

2.2.4 Tracker

The silicon tracker is the innermost part of the CMS detector, covers a sensitive area of roughly $200\,\mathrm{m^2}$ and is therefore the largest silicon detector ever built. Its task is to precisely detect trajectories of charged particles and to reconstruct vertices which requires good spatial resolution [K$^+$98]. From the direction of the track-bending the sign of the charge can be determined while the momentum is calculated using the bending radius of the particle track. However it is not possible to detect neutral particles with the tracker. A difficult task is to cope with the short bunch crossing times of 25 ns which corresponds to 40 million bunch crossings per second. The average number of simultaneous proton-proton collisions (called pile-up) are – so far – 25 per bunch crossing yielding in up to 1000 emerging particles [D$^+$12]. Due to the high particle flux the detector requires a radiation-hard design, high granularity and a fast readout. Further the detector has to be cooled to improve the durability and reduce the power consumption. At the same time it is important to keep the material budget as low as possible to minimise multiple scattering and to receive good tracking conditions. Since the particle flux is highest close to the beam and decreases with increasing radius the tracker consists of two parts using different sensor technologies. The inner part is a silicon pixel detector equipped with 2D segmentation technology while the outer part is a silicon micro strip detector with 1D segmentation.

[6] η is the pseudo rapidity, which is defined as $\eta = -\ln\left[\tan\left(\frac{\theta}{2}\right)\right]$, where θ is the polar angle between beam axis and particle track.

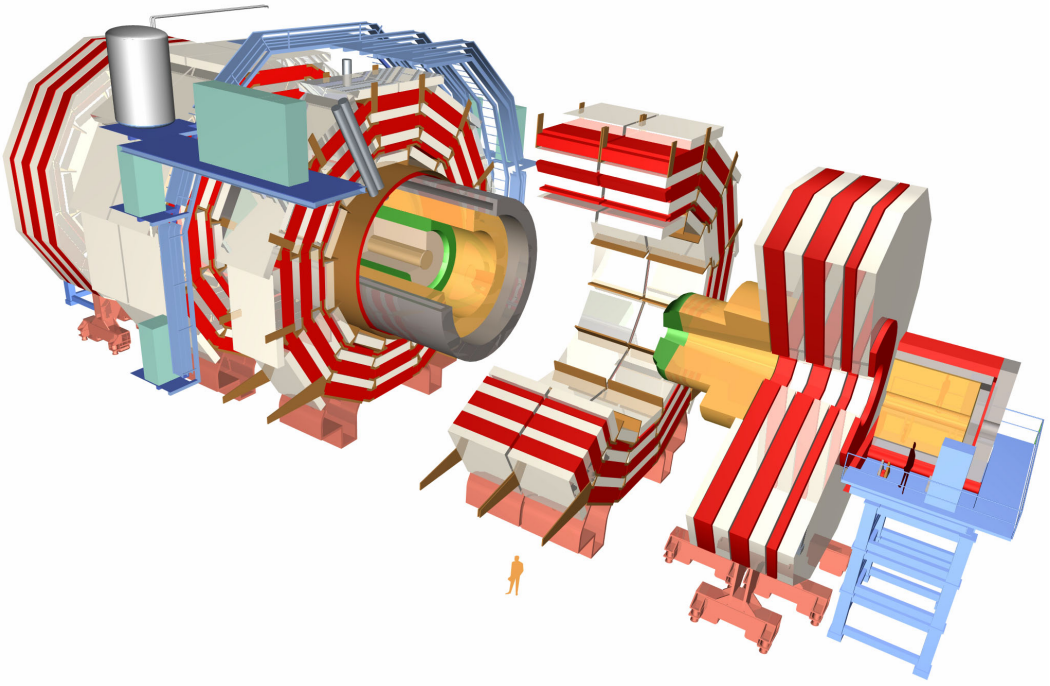

Figure 2.6: Sketch of the CMS detector showing the different components: The sandwich structure of the iron return yoke and the muon chambers (red and white), the solenoid magnet (grey), the hadron (yellow) and electromagnetic (green) calorimeters and the tracker in the centre (white-grey). As indicated in the figure CMS can be separated in single parts [CMS11].

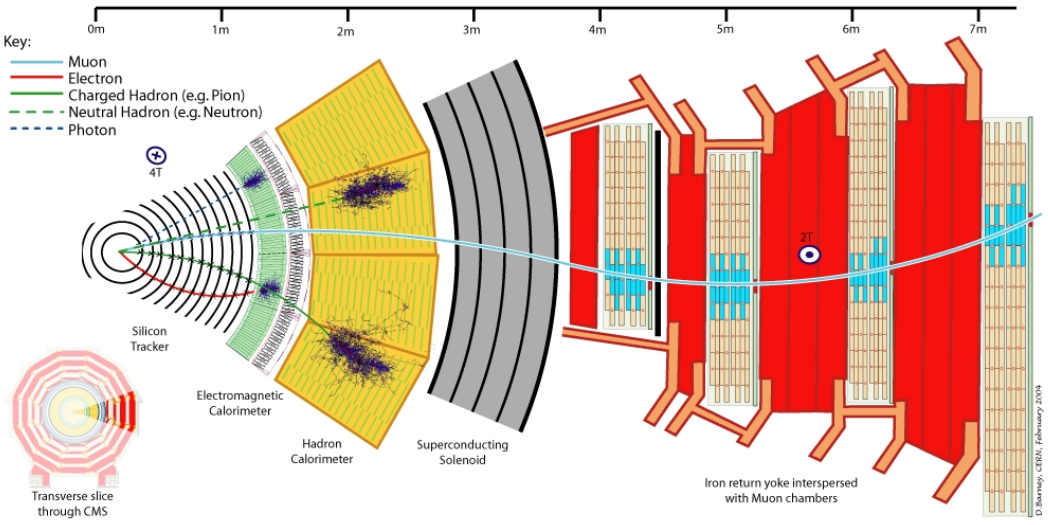

Figure 2.7: Slice of the CMS detectors presenting the silicon tracker, the electromagnetic and hadron calorimeters, the solenoid magnet and the sandwich structure consisting of the iron return yoke and the muon chambers. In addition several exemplary particle tracks and their interactions with the detector components are depicted [Bar13].

The current pixel detector consists of three barrel layers – mounted at radii of 4 cm, 7 cm and 11 cm – and two endcaps on each side of the barrel section with a total of 66 million readout channels. Thanks to the high granularity the pixel detector is able to handle fluxes of up to 1 MHz/mm^2 with an occupancy below 1%. Since the pixel detector is the main subject of this thesis it is described in detail in section 3.

As the particle flux decreases with radius it is not necessary to equip the tracker completely with pixel detectors. A micro strip detector is mounted instead which can be divided in two regions, the outer tracker and the inner tracker. In total the micro strip detector consists of 10 barrel layers, 6 small endcap-like discs and 18 endcaps with an overall amount of 15 148 modules. Inner and outer tracker cover the volume from 20 cm to 1.1 m and a pseudo rapidity range of up to $|\eta| < 2.5$ [Sat08]. The modules differ in length (10 cm to 25 cm) [HS12], thickness (320 µm and 500 µm) and pitch (80 µm to 184 µm) [But12]. Further there are some layers which consist of back-to-back modules. This mean they are made of two strip sensors and tilted by an angle of 100 mrad to measure 2D coordinates. Although the micro strip detector covers a much larger area than the pixel detector it only requires 10 million readout channels.

2.2.5 Electromagnetic Calorimeter

The part adjoined to the tracker is the electromagnetic calorimeter (ECAL). Its aim is the precise energy measurement of electrons and photons. They deposit their energy via pair production and the emission of bremsstrahlung. The corresponding electromagnetic showers stop when the particles energy falls below the pair production threshold of 1.022 MeV. Measuring electrons or photons is achieved by choosing material which stops and fully absorbs electromagnetic showers. In order to fit into the solenoid magnet and to fulfil the above requirements the material needs to have a short radiation length[7] X_0 and high density ρ. For this reason the scintillator material $PbWO_4$ ($X_0 = 7.37\,\mathrm{g/cm^2}$ and $\rho = 8.28\,\mathrm{g/cm^3}$) was chosen which provides a very fast scintillation process with 80% light emission within the LHC bunch-crossing time of 25 ns [CMS06]. Only the small light yield of 50 photons/MeV of the frustum-shaped crystals is a minor handicap. The barrel region consists of 61 200 crystals and the endcaps of 14 648 crystals [Bro07]. The electromagnetic calorimeter covers a pseudo rapidity range of $|\eta| \lesssim 3$. The scintillator crystals of the ECAL are read out by photo multipliers. Based on the amount of charge read out in the ECAL it is possible to calculate the energy of the absorbed particle. Due to radiation damage during the operation of the ECAL the transmissibility will suffer and has to be taken into account in the energy resolution [Bon12]. The relative energy resolution of the electromagnetic as well as the hadron calorimeter is given by (see e.g. [Ngu11]):

$$\left(\frac{\sigma}{E}\right)^2 = \left(\frac{S}{\sqrt{E}}\right)^2 + \left(\frac{N}{E}\right)^2 + C^2. \tag{2.2}$$

With the stochastic term S, the noise N and the constant contribution C to the signal.

2.2.6 Hadronic Calorimeter

The hadron calorimeter (HCAL) measures the energy of hadrons like neutrons, protons, kaons or pions [CMS06]. Due to the strong interactions of hadrons in the HCAL the corresponding hadronic showers are much more complex than the electromagnetic showers in the ECAL. In addition the cone in which the energy is deposited is much wider which results in a more difficult energy reconstruction. The HCAL uses a sandwich-like design with a plastic scintillator material interleaved with dense brass made of Russian artillery shells [Sha09]. This

[7] The radiation length is defined as the length over which an electron loses all but $1/e$ of its energy.

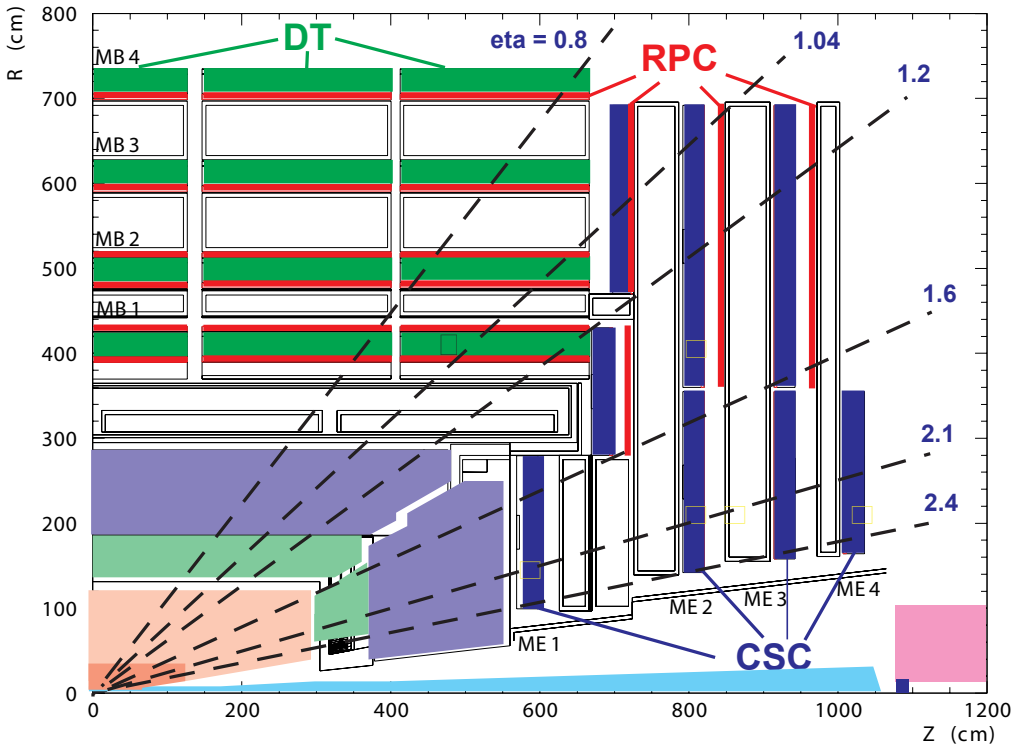

Figure 2.8: Design of one quarter of the CMS muon system including the covered pseudo rapidity range. DTs (dark green) are used in the barrel region and CSCs (dark blue) in the endcap region while RPCs (red) are used in both [CMS06].

ensures that the HCAL fits into the solenoid magnet and still provides efficient absorption of high energy hadrons. The pseudo rapidity coverage of the HCAL components within the solenoid is $|\eta| \lesssim 3$, however the pseudo rapidity range increases up to $|\eta| = 5.2$ due to the forward HCAL outside the solenoid magnet. Besides this there are two additional active layers outside the magnet to ensure that the total absorber thickness is larger than 5 times the interaction length [CMS97b].

2.2.7 Solenoid Magnet

Measuring the momenta of particles within the tracker requires – as described in section 2.2.4 – a magnetic field to bend the tracks. Such a magnetic field has to be very strong if even high p_T particles shall be measured with a momentum resolution less than one percent. To fulfil this requirements CMS uses a superconducting solenoid magnet with a length of 12.9 m and an inner diameter of 5.9 m. The operation temperature of the magnet is $T = 4.6\,\mathrm{K}$ providing a 3.8 T magnetic field. Outside the solenoid magnet a 10 000 t iron yoke returns the magnetic flux achieving a 2 T magnetic field within the muon chambers. The solenoid magnet is large enough to house the tracker and almost the entire components of calorimeters. This is desirable since particles do not have to pass much material before their energy is measured. The cold mass of the magnet amounts to 220 t distributed over four winding layers of superconducting cables. Due to the high amount of stored energy (2.7 GJ) the ratio between stored energy and cold mass is high resulting in a deformation of the solenoid of about 0.15 % during the energising process. For that reason the solenoid is made of stabilised reinforced NbTi [CMS06, CMS08].

2.2.8 Muon Chambers

As already indicated by the experiment name Compact Muon Solenoid the identification and measurement of muons is a major task [CMS06], especially since the golden decay channel of the Standard Model Higgs boson into four muons – which achieves one of the cleanest signatures – is of huge interest. Since muons are able to penetrate several metres of iron without interacting they are able to pass the calorimeters. For this reason the muon chambers are located in the outer region where muons are the only particles still present. Further the measurements from the muon systems and the tracker are combined to improve the momentum resolution. As a result of the importance of muons CMS uses three types of redundant detectors to investigate muons [CMS97a]. The drift tubes (DT) provide a precise measurement of the position and are located in the barrel region where the muon rate is low. DTs cover a pseudo rapidity range up to $|\eta| = 1.3$. In the endcaps where the muon rate is high and the magnetic field is not uniform cathode strip chambers (CSC) are used. The pseudo rapidity range covered by the CSCs is approximately $0.9 < |\eta| < 2.4$. Resistive plate chambers (RPC) are the third detector type which in contrast to DTs and CSCs are installed in the barrel and the endcap region. They provide a pseudo rapidity coverage up to $|\eta| = 2.1$. An advantage of CSCs is a time resolution of 1 ns which is favourable for fast trigger information. Overall there are 1630 muon chambers consisting of 912 RPCs, 468 CSCs and 250 DTs [Abb13, CMS11]. A sketch of the muon systems is presented in figure 2.8.

2.2.9 Trigger System

Since the LHC provides a collision rate of 40 MHz corresponding to only 25 ns between each bunch crossing an effective and fast trigger system is required to reduce the data and only store interesting events. The CMS trigger systems consists of two main parts (as depicted in figure 2.9) [VPB07], the Level-1 Trigger (L1) and the High Level Triggers (HLT). The L1 trigger is a hardware system based on FPGAs[8] and hard-wired ASICs[9] using information from the muon systems and the calorimeters. It searches for events with clear signatures like muons with very high transverse energy E_{T} or missing transverse energy $E_{\mathrm{T}}^{\mathrm{miss}}$. The time which is required from detecting an event until the L1 trigger comes to a decision is only 3.2 µs. Due to the L1 trigger the data rate is reduced down to about 100 kHz [B$^+$00, CRS02] and the corresponding data is sent to computer farms [A$^+$09]. There the HLT reduces the rate once again resulting in a data rate of a few 100 Hz [B$^+$12a].

In contrast to the L1 trigger the HLT is a very dynamical software system and can be adjusted depending on the physics objectives or experimental conditions like luminosity. Nevertheless the CMS detector generates huge amounts of data which is analysed by the Worldwide LHC Computing Grid.

[8] Acronym: **F**ield **P**rogrammable **G**ate **A**rray
[9] Acronym: **A**pplication **S**pecific **I**ntegrated **C**ircuits

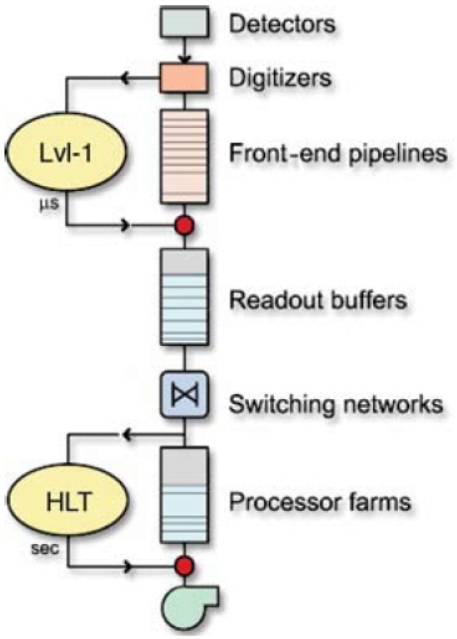

Figure 2.9: Block diagram of the data flow in the CMS trigger system. The trigger system consists of the hardware based Level-1 Trigger, the readout buffers and the processor based High Level Trigger [CRS02].

3. The CMS Pixel Detector

The innermost part of the Compact Muon Solenoid (CMS) is the CMS pixel detector. Its task is to measure the momentum of charged particles emerging in proton-proton collisions by measuring its trajectories. A precise determination of the impact parameter with regard to the primary interaction point is necessary for accurate vertex reconstruction. To meet the requirements the pixel detector needs a fine spatial resolution, a fast readout system and radiation hardness to get along with the harsh conditions around the interaction point. Besides this the material budget should be minimised to limit multiple scattering which complicates track fitting and vertex reconstruction.

This chapter deals with semiconductor detectors in general, the CMS pixel detector, its readout chip as well as the Phase I Upgrade of the CMS pixel detector.

3.1 Semiconductor Detector

Since 1960 semiconductor sensors are used for spectroscopy applications, however gas detectors were used for a long time to measure particle tracks [Lut99]. Semiconductor detectors and gas-filled ionisation chambers rely on the same detection principle even though they use different media. Not until 1970 semiconductor detectors became usual tracking detectors in particle physics. The most common choice of them are silicon detectors which have the benefit that only 3.6 eV are necessary to create an electron-hole pair compared to 20 eV for gas ionisation resulting in a better energy resolution [R$^+$06]. Furthermore semiconductor detectors provide low weight, good radiation hardness and can be produced by modern lithography processes. Another crucial argument in favour of these detectors are the affordable costs. Due to the high number of originating charge carriers (roughly 100 $e^-/\mu m$ in silicon) they achieve a good energy resolution. In addition semiconductor detectors facilitate the application of very thin active materials (300µm to 500µm) still providing a distinct signal. Using such low thicknesses leads to fast signal propagation and reduces the material budget.

3.1.1 Energy Band Model

The energy band model characterises the state of charge carriers of solid materials and explains their conductivity (see e.g. [Dem05]). According to quantum mechanics each atom has sharply separated energy levels which are occupied by electrons. Considering a solid object – consisting of about 10^{23} atoms – the atoms are so close together that quantum effects split-up equivalent energy levels resulting in energy multiplets. Because of the very high

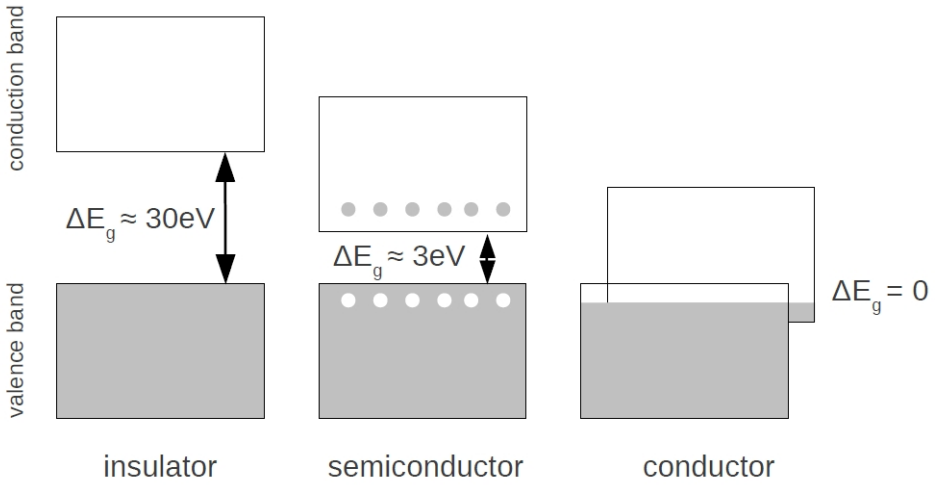

Figure 3.1: Sketch of the energy band structure for different materials. Insulators (left) have a large bandgap of $\Delta E_g > 3\,\text{eV}$ and an unoccupied conduction band (white). In semiconductors (middle) the bandgap is small ($\Delta E_g < 3\,\text{eV}$) and electrons may be lifted – thermally or by radiation – into the conduction band as illustrated. In case of conductors (right) there is no bandgap and electrons can simply enter the conduction band [Hos12].

density of each multiplet they can be treated as continuous distributions called energy bands. The highest energy band occupied by electrons is called valence band, the next higher one is the conduction band while the distance between them is named bandgap. The size of the bandgap states how much energy is required to lift an electron from the valence band into the conduction band. In case of silicon the bandgap is $\Delta E_g = 1.124\,\text{eV}$ at $T = 300\,\text{K}$ [Har09]. Further the bandgap and the occupation of the energy bands serve as classification criteria of solid objects, which are conductors, semiconductors and insulators. Sketches of the energy band structures of each are presented in figure 3.1.

- A solid object is called insulator if the conduction band is entirely free of charge carriers and when the bandgap is larger than $\Delta E_g > 3\,\text{eV}$. Due to the size of the bandgap electrons are not able to reach the conduction band independent from the present temperature.
- At low temperatures semiconductors also have a entirely unoccupied conduction band and behave like an insulator, however they have a smaller bandgap $\Delta E_g < 3\,\text{eV}$. Out of this they obtain the interesting semiconducting feature that electrons – due to the small bandgap – reach the conduction band when the temperature increases. The charge carriers of a semiconductor are the electrons in the conduction band and the holes in the valence band. Aside from thermal excitation electrons may be lifted into the conduction band by radiation.
- In conductors the valence and conduction bands overlap. Hence they show conductivity independent of the temperature.

Pure semiconductors are not favourable for semiconductor detectors since they have too many free charge carriers under typical experimental conditions.

3.1.2 Doping

Before the methods are explained to reduce the number of free charge carriers a further process has to be introduced. This process is called doping and deals with semiconductor

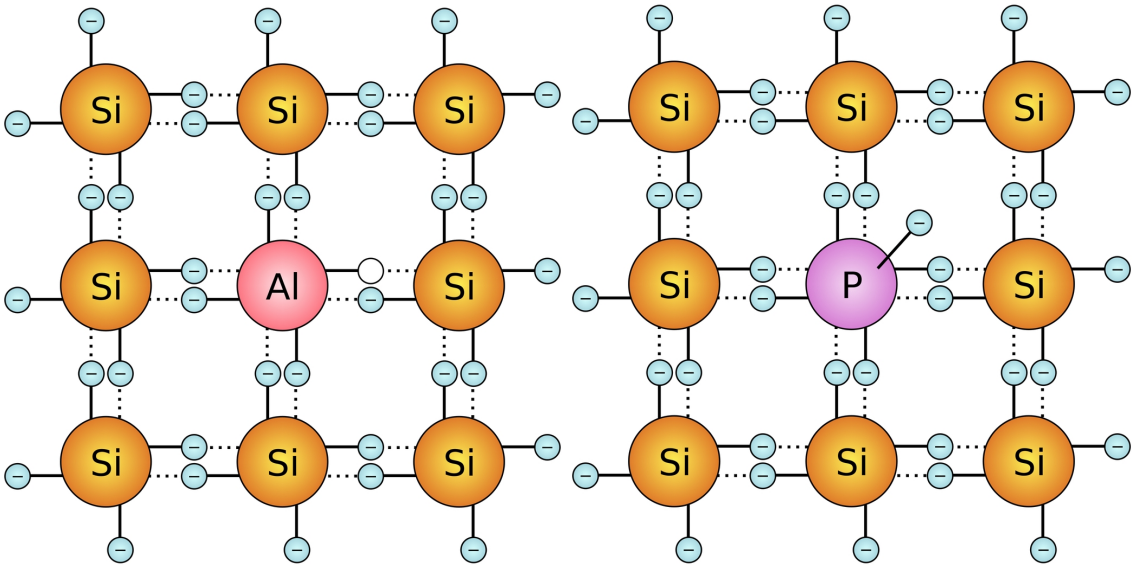

(a) p-doped silicon (b) n-doped silicon

Figure 3.2: This figure illustrates both possibilities of silicon doping. In (a) an aluminium impurity is implanted into the silicon lattice. Aluminium only provides three valence electrons hence the created charge carrier is a hole (p-type). (b) If the silicon is doped with phosphorus a quasi-free electron is added as negative charge carrier (n-type) [Com06a, Com06b].

properties which can be manipulated specifically by implanting impurities (named dopants). Since the electrical properties and the conductivity are basically dominated by the impurity atoms doped, semiconductors are called extrinsic semiconductors. A distinction is made between p-type and n-type semiconductors depending on the dominant charge carriers.

Figure 3.2 gives an example of an p-type and n-type silicon semiconductor. As silicon is an element of group IV in the periodic table it is equipped with four valence electrons. In a silicon lattice the four valence electrons of each atom enter a covalent bond. Replacing a silicon atom in the lattice by another atom with a different number of valence electrons changes the conductivity. In case of an element of group III – like aluminium – the added charge carrier is a hole (p-type), since these elements only have three valence electrons. Phosphorus an element of group V has five valence electrons, as one of its five electrons is not able to enter a covalent bond and remains (quasi-free), an electron charge carrier (n-type) is created. As group III elements are able to accept electrons they are called acceptors while group V elements – providing electrons – are donors (see e.g. [Hil08]).

The energy band model theory explains the change of the conductivity by doping the semiconductor. The introduction of dopants creates energy levels within the bandgap. Acceptors add energy levels close to the valence band hence electrons can easily leave a covalent bond and enter the acceptor levels leaving a hole in the valence band. In case of a donor an energy level slightly below the conduction band is added. A (quasi-free) electron can fairly easy be lifted into the conduction band because the gap between conduction band and added energy level is much smaller than the original bandgap.

There are several techniques of doping like ion implantation or diffusion which are described in [Sch05]. Crucial for the choice of a dopant is the final design of the device and the doping technique as different elements have different properties such as implantation depth.

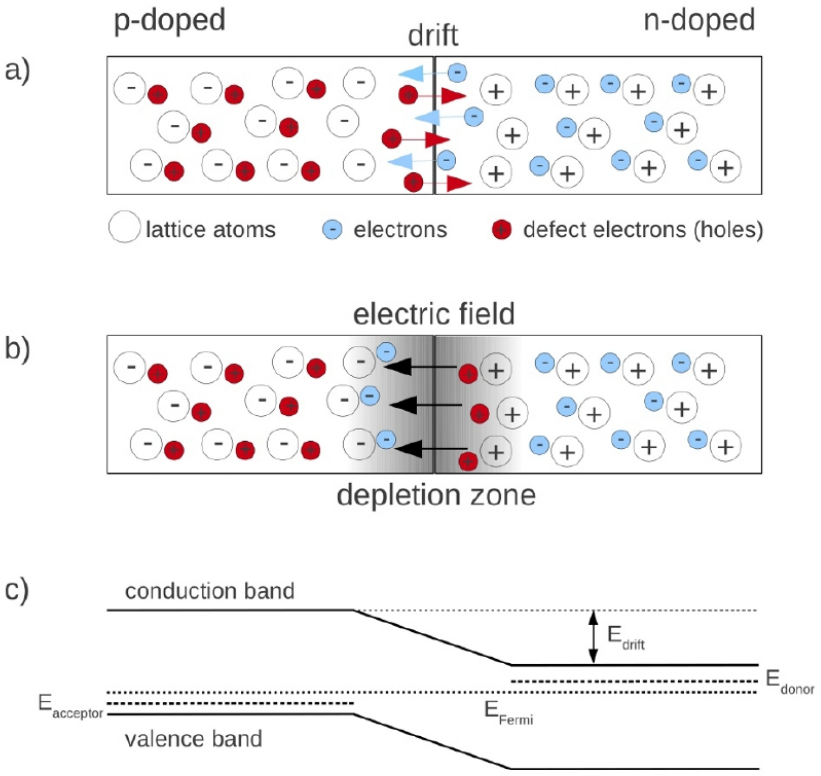

Figure 3.3: In (a) a pn-junction before the equilibrium is established is shown. Due to different Fermi levels electrons drift from n-side to p-side. The holes in the p-side can be considered as positive charge carriers which drift to the n-side. In (b) an equilibrium is established and a common Fermi level is generated. Electrons and holes recombine and a charge carrier free depletion zone originates within the contact area. (c) The energy band model of the pn-junction – at equilibrium – is displayed. The acceptor and donor levels as well as the common Fermi level over the pn-junction are visible [Hos12].

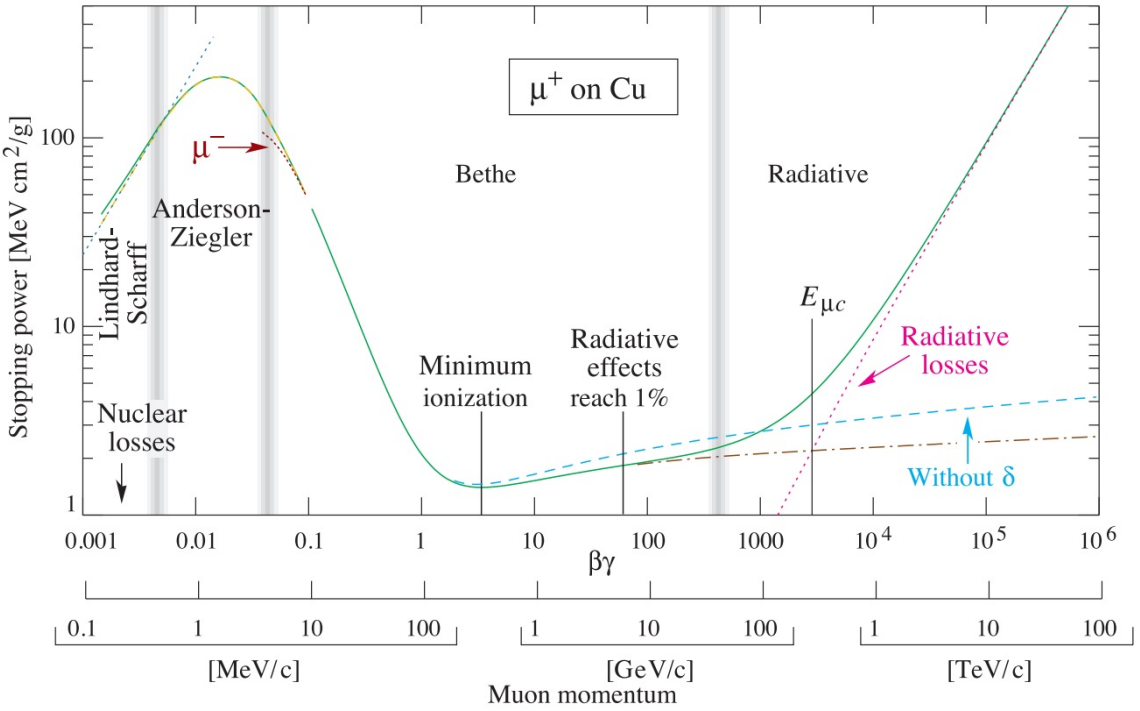

Figure 3.4: The plot shows the stopping power for positive muons in copper as a function of $\beta\gamma$. The Bethe equation is valid in the middle of the depicted momentum range. A minimum of the stopping power exists at $\beta\gamma \approx 2-3$ within the Bethe region, particles in this region are minimum ionising particles [B+12b].

3.1.3 pn-Junction

Silicon semiconductors with opposite doping have different Fermi levels E_F due to different energy levels created by acceptors and donators (see figure 3.3 c). Once these two components are connected free electrons of the n-side drift in the direction of the lower Fermi level of the p-side (see figure 3.3 a). This proceeds until at equilibrium, a common Fermi level across the pn-junction is formed. Inside the contact area electrons and holes recombine and a charge carrier free depletion zone is established (see figure 3.3 b). The width of the depletion zone depends on the original Fermi levels and the doping concentration and from the applied bias voltage. If the positive pole of the applied voltage is connected to the n-type and the negative pole to the p-type material (called reverse bias) the depletion zone grows due to an increase of the electrical field within the pn-junction. By applying a reverse bias voltage the amount of free charge carriers is reduced. The small current which occurs anyhow is called leakage current and is an important quantity influencing the power consumption and performance of silicon detectors.

A 300 µm thick intrinsic silicon semiconductor – as used by CMS – has 10^9 free charge carriers at room temperature while only 2×10^4 charge carriers are created by a charged particle [Har09]. Without reducing the amount of free charge carriers it would not be possible to identify the signal above the noise level hence CMS semiconductors detectors have pn-junctions with reverse bias.

3.1.4 Interaction of Particles and Matter

The principle of each particle detection is that they interact with the detector material. In case of the CMS tracker only particles can be detected which undergo electromagnetic interactions hence it is not possible to detect neutral particles like neutrons. Aside from

charged particles monochromatic photons are of major interest since they are important for calibrating silicon detectors, as will be described in Chapter 4 and 5.

Charged Particles

The interaction of charged particles with matter depends on the characteristics of the absorber material and the properties of the charged particles like momentum and charge. A heavy charged particle is characterised by a mass significantly heavier than electrons. Such particles mainly interact with the traversed material via ionisation and excitation losing their energy continuously. The Bethe equation describes the energy loss per distance of heavy charged particles traversing the matter [B+12b]:

$$-\left\langle \frac{dE}{dx} \right\rangle = Kz^2 \frac{Z}{A} \frac{1}{\beta^2} \left[\frac{1}{2} \ln \frac{2m_e c^2 \beta^2 \gamma^2 T_{\max}}{I^2} - \beta^2 - \frac{\delta(\beta\gamma)}{2} \right]. \tag{3.1}$$

The constant $K = 4\pi N_A r_e^2 m_e c^2$ consists of the Avogadro number N_A, the electron radius r_e, its mass m_e and the speed of light c. Further z is the charge of the incident particle, Z and A the atomic number and atom mass of the absorber as well as relativistic factors β and γ. $T_{\max}$ is the maximum kinematic energy which can be transferred to an electron, I is the mean excitation energy and $\delta(\beta\gamma)$ is a term considering a correction to density effects.

Figure 3.4 shows the stopping power of muons in copper as a function of $\beta\gamma$. The region is indicated where the Bethe equation is valid, at lower momentum various effects dominate the energy loss while radiative losses are responsible at high energies. A minimum of the mean energy loss exists at $\beta\gamma \approx 2-3$ within the Bethe region, particles corresponding to this region are minimum ionising particles (MIPs).

In case of light charged particles like electrons and positrons the Bethe equation is invalid. At low energies those particles undergo scattering and ionisation processes while they lose their energy via bremsstrahlung at high energies (see figure 3.5). When particles lose energy via bremsstrahlung they emit radiation due to deflection in the electric field of particles, mainly nuclei. First of all this effect is important in the electromagnetic calorimeter however it deposits sufficient energy in the tracker to be detected.

Photons

Photons interact with matter via three mechanisms, whereby the cross sections depend on the photon's energy and the mass number Z of the absorber. The three interaction mechanisms are photoelectric effect, Compton scattering and pair production. In all of them photons transfer their energy to charged particles which in turn can be detected. The corresponding cross sections of the interaction mechanisms as a function of the photon energy are depicted in figure 3.6.

- Compton scattering is inelastic scattering of a photon with an outer shell electron where the photon is not absorbed but its wavelength changes due to energy loss. This energy is transferred to the electron which leaves its shell where the amount of transferred energy depends on the scattering angle and is maximum at 180°. The Compton equation describes the energy E'_γ of the scattered photon as a function of the initial photon energy E_γ and the scattering angle θ [Sch95].

$$E'_\gamma(\theta) = E_\gamma \left(1 + \frac{E_\gamma}{m_e c^2} \cdot (1 - \cos\theta) \right)^{-1}, \tag{3.2}$$

  where m_e is the electron rest mass and c the speed of light. Compton scattering is the dominant mechanism for photon energies between 100 keV and 5 MeV.

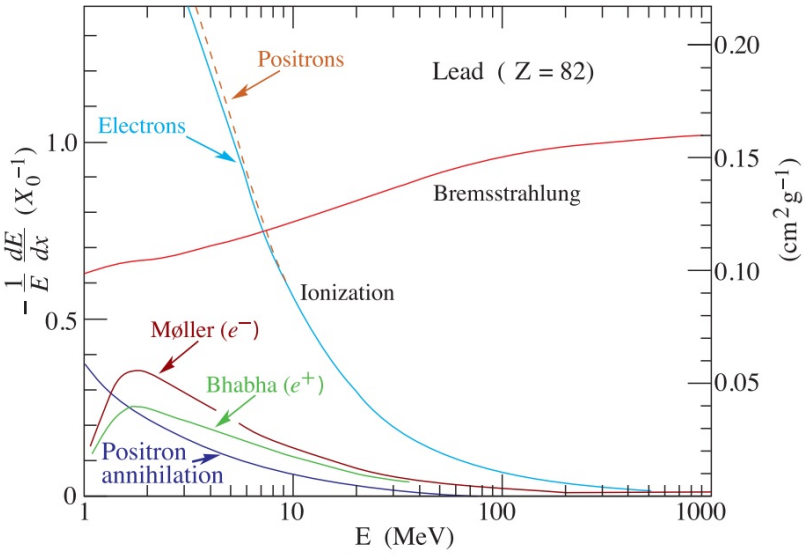

Figure 3.5: Energy loss per radiation length in lead as a function of electron or positron energy (light charged particles). Above energies of roughly 10 MeV bremsstrahlung becomes the dominant mechanism. At very low energies ionisation, annihilation as well as scattering processes are contributing to the energy loss [B+12b].

- Pair production describes the production of electron-positron pairs. This is only possible in the presence of a nucleus due to momentum conservation. Further the energy of the photon has to be higher than twice the electron rest mass $E = 2 \cdot m_e = 1.022\,\text{MeV}$. Pair production is the dominant process at high energies and depends on the atomic number Z of the absorber. Above $E_\gamma = 10\,\text{MeV}$ all other mechanisms are neglectable.
- The photoelectric effect describes the mechanism when a photon is entirely absorbed by an inner shell electron which in turn leaves the atom. A vacancy occurs which is filled by an outer shell electron emitting a low energy photon. The photoelectric effect is the dominant effect at energies below $E_\gamma = 100\,\text{keV}$.

3.1.5 Semiconductor Pixel Detectors

The function principle of a semiconductor pixel detector is based on the pn-junction of the sensor operated in reverse bias mode. The bias voltage should be high enough to deplete the sensor over the full thickness to maximise the sensitive volume. The voltage which is necessary to deplete the sensor entirely is called full depletion voltage. This voltage is not constant during the operational detector lifetime due to radiation damage generating additional energy levels in the bandgap and increasing the conductivity. Further information may be found in [Mol99].

The energy which charged particles lose when they traverse the depleted sensor is described by the Bethe equation (Equation 3.1). In this way charged particles excite electrons from the valence into the conduction band and produce electron-hole pairs as indicated in figure 3.7. The electric field applied by the bias voltage ensures that the created charge carriers drift to the electrodes where the corresponding signal is processed by readout electronics.

The 2D spatial resolution is achieved by segmenting the sensor in a pattern of isolated pixels as it is presented in figure 3.8. Each pixel is read out individually. The resolution of a pixel detector can be improved by exploiting charge sharing effects as it is the case in the CMS pixel detector. This is possible when particles traverse the sensor and deposit charge in more than one pixel. The underlying mechanism is the Lorentz drift of charge carriers in the

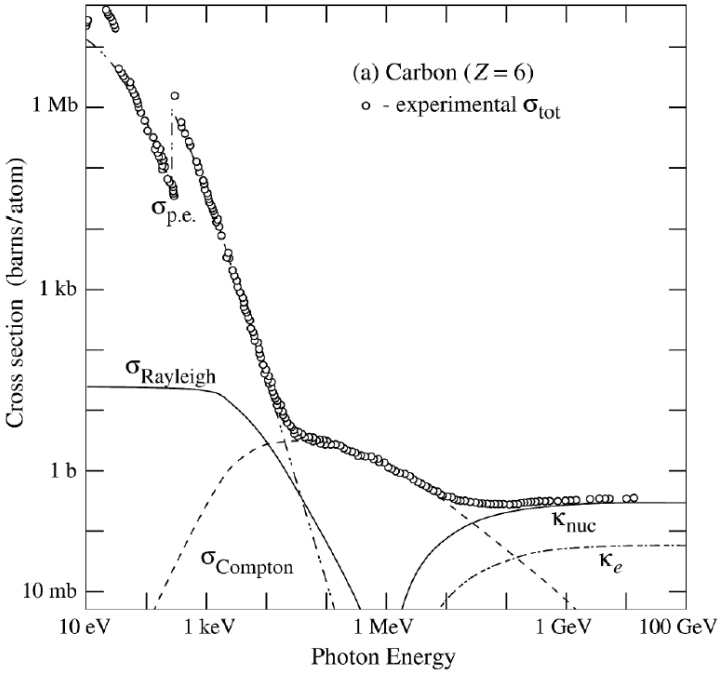

Figure 3.6: Total cross sections of photon interactions in carbon as a function of photon energy. Up to 100 keV the photoelectric effect is dominant, between 100 keV and 5 MeV Compton scattering is dominant and for energies above 5 MeV it is pair production. [B+12b].

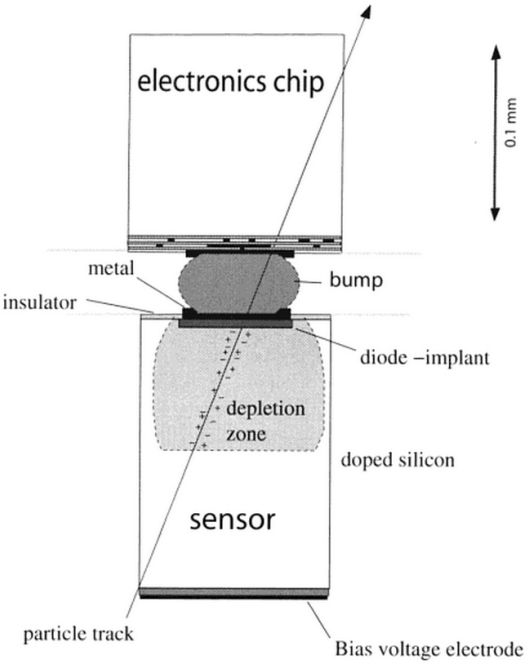

Figure 3.7: Schematic view of a semiconducting pixel detector cell. A particle traversing the depleted sensor loses energy continuously and creates electron-hole pairs. Those charge carriers are collected by an electric field and read out by electronics [R+06].

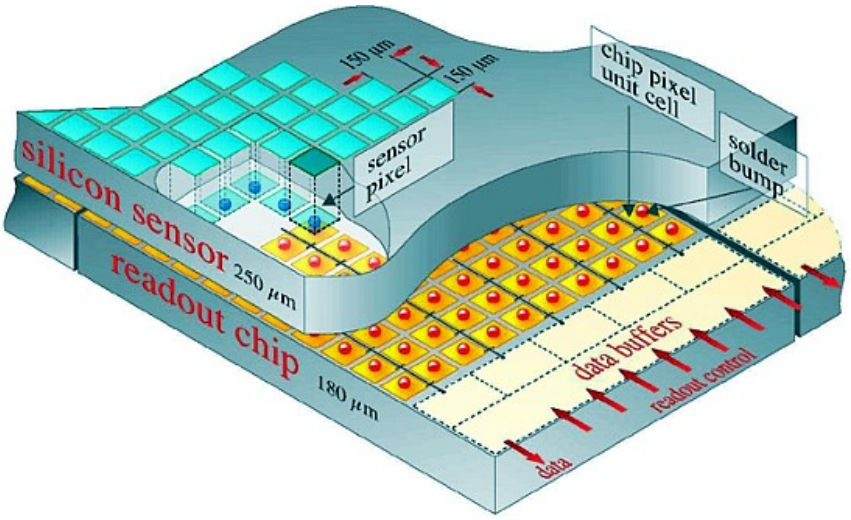

Figure 3.8: Schematic view of a hybrid pixel detector. Each sensor pixel is connected via a solder bump to a pixel unit cell on the readout chip. The hit data is stored in buffers on the bottom edge of the readout chip where it waits for the L1 trigger decision [CMS13b].

combined electromagnetic field such as the one of the CMS solenoid magnet. The number of hit pixel (pixel cluster) depends on the type of the charged particles and the incident angle. Calculating the centre of the charge distribution of the pixel clusters improves the resolution. However there is also a drawback, since the signal to noise ratio degrades when the charge is spread over more than one pixel. The signal to noise ratio qualifies how reliable a signal can be identified above the background. By mounting several layers of pixel detectors and fitting the penetration points of the particles trajectories a 3D measurement is achieved.

3.2 The CMS Pixel Detector

The CMS pixel detector consists of two parts, the cylindrical symmetrical barrel region (BPix) and the forward endcap region (FPix). In the current design the barrel region is equipped with three layers while the endcaps at each side are equipped with two discs (see figure 3.9) [CMS06, Erd10]. The pseudo rapidity covered by this design goes up to $|\eta| \lesssim 2.5$ with two to three penetration points per track.

The three barrel layers are located at radii of 4.4 cm, 7.3 cm and 10.2 cm from the beam axis. The radius of the innermost barrel layer is limited by the beam pipe, but it is necessary to mount this layer as close as possible to the interaction point to achieve the best possible impact parameter resolution. In total the layers in the barrel region consist of 672 full modules and 96 half modules which are required to assure a sensitive area without gaps. The forward endcap discs – consisting of modules mounted on several blades (see figure 3.9) – are located at distances of 34.5 cm and 46.5 cm from the interaction point. They provide a sensitive area from radius $r = 6$ cm up to $r = 15$ cm surrounding the beam axis. Furthermore all blades are slightly tilted with an overlap to guarantee a gapfree coverage.

Figure 3.10 shows the structure of a module which has a size of 66 mm × 21.2 mm in the current design and 66 mm × 22 mm after the Phase I Upgrade [D$^+$12]. Modules consist of two rows with eight readout chips each connected via bump bonds to the silicon sensor. All 16 readout chips are wire bonded to the high density interconnect (HDI) which distributes power, the LHC 40 MHz bunch crossing clock and signal as well as trigger information. On top of the HDI the token bit manager (TBM) is located, a chip managing readout, external signals

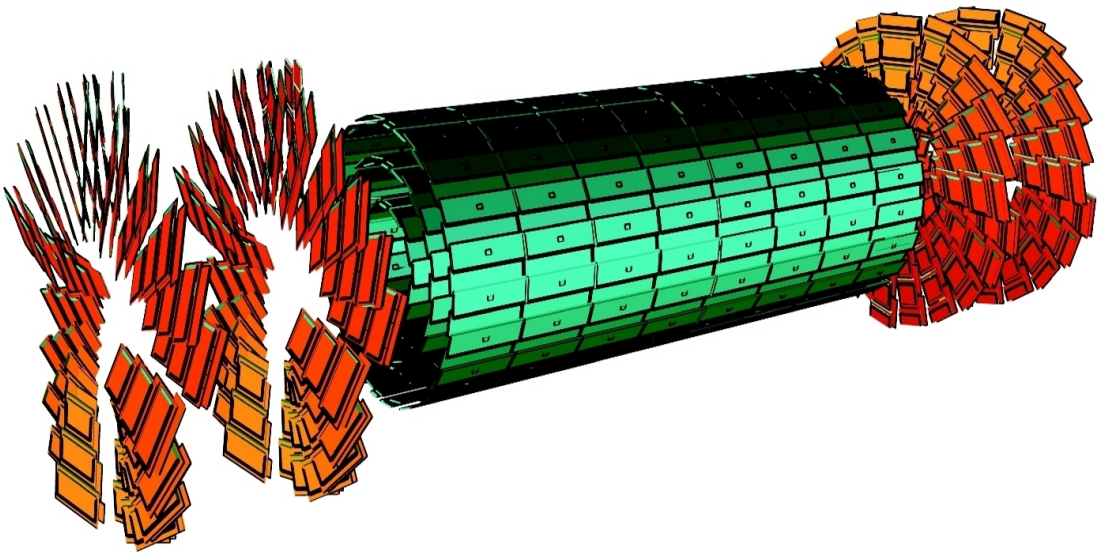

Figure 3.9: The drawing shows the barrel region and the endcaps of the current CMS pixel detector. The barrel region – depicted in green – consists of three layers assembled of rectangular modules while on each side are two endcaps – depicted in orange – constructed as tilted blades [CMS10].

and powering. The collected data is transferred by a cable while basestrips – components for mounting a module – are glued on the bottom side of the ROCs.

The silicon sensor of the CMS pixel detector uses an n-in-n technology consisting of a highly resistive n-substrate and highly doped n-implant serving as charge collecting electrode. The pn-junction is formed by a p-substrate on the back side. Due to the n-in-n technology the collected charge carriers are electrons which have the advantage of higher mobility compared to holes.

The pixel size is 150 µm in the z-direction (beam axis) and 100 µm in the $r\phi$-plane (perpendicular to the beam axis) and is determined by the following constraints. To improve the spatial resolution charge sharing between two pixels is exploited as described in section 3.1.5. The optimum pixel size in $r\phi$ can be established by calculating the Lorentz angle as explained in [Erd10]. Based on a Lorentz angle of 25° and 285 µm sensor thickness the charge does not spread over more than 150 µm. Hence a length of 100 µm in $r\phi$ ensures charge sharing over only two pixels. The z-direction is determined by the minimum size for the underlying pixel unit cell which hosts the required readout logic of a pixel. This results in a length of at least 150 µm in z-direction. The provided resolution of this design is 15 µm [CMS10].

An additional requirement for the sensor is that the pixel size on three of four edges has twice the standard size ($2 \times (150\,\mu m \times 100\,\mu m)$) while the two corners of these three edges have four times the standard size. This design is chosen as the 16 ROCs are single parts which require some tolerances during the ROC to sensor bump bonding procedure (for further information concerning bump bonding see [Hei12]).

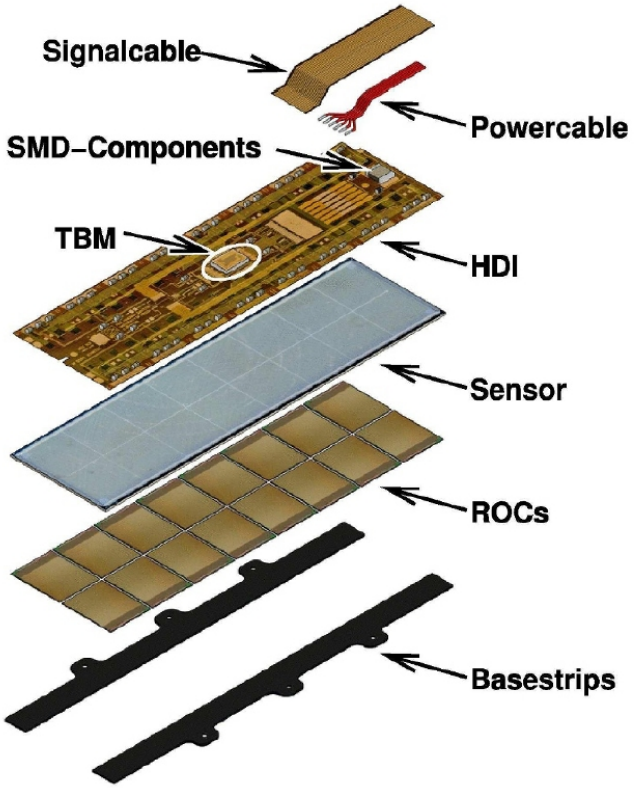

Figure 3.10: Components of a current module which are from bottom up: two basestrips for module mounting, 16 readout chips (ROCs), the silicon sensor, a high density interconnect (HDI) including the token bit manager (TBM) plus the signal and power cables [Erd10].

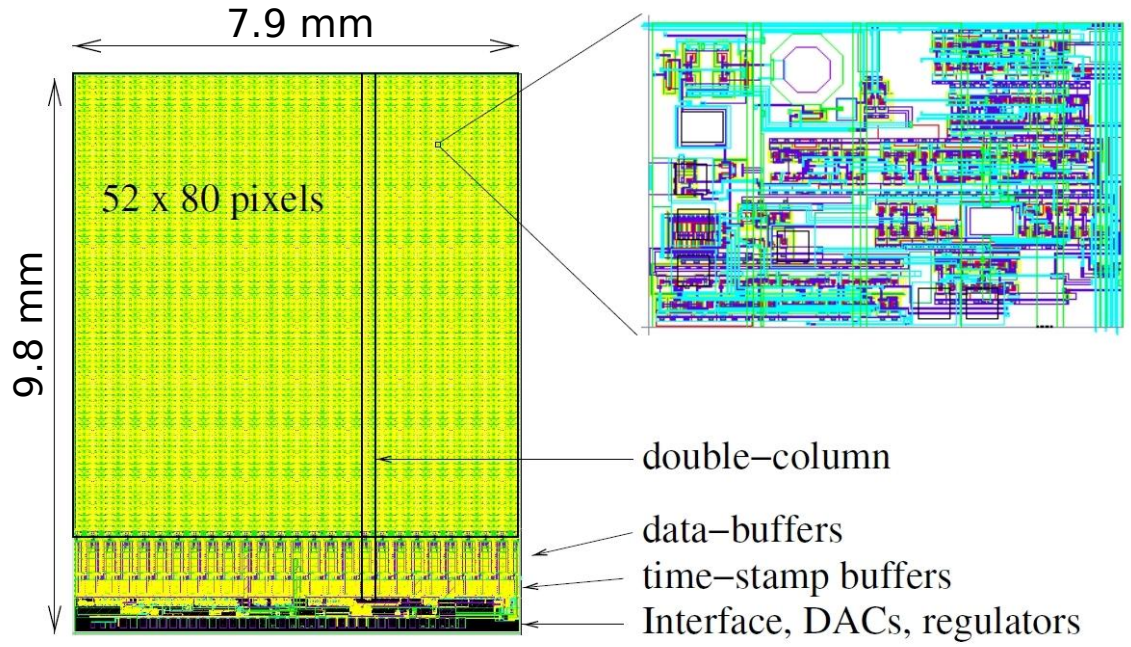

Figure 3.11: Floor plan of a PSI46 readout chip plus a zoomed sketch of a PUC. The 80×52 matrix of pixel unit cells has a size of 7.8 mm $\times$ 8 mm while the periphery has – in case of the PSI46V2 – a length of 1.8 mm [Erd10].

3.2.1 Readout Chip

The current readout chip of the CMS pixel detector is the PSI46V2 which will be replaced in 2016/17 by a new version, the PSI46dig. The final version number is not yet established, the latest available version – when this thesis is written – is the PSI46digV2. To meet the radiation hardness requirements the readout chips are produced in a 0.25 µm CMOS process [D$^+$12, Erd10]. This thesis deals particularly with the ROCs PSI46digV1 and PSI46digV2 since the detector performance is mainly determined by the ROC and the sensor. Measurements concerning the currently installed ROC PSI46V2 – which will be introduced first – can be found in [Hos12]. Note that all readout chips use identical sensors.

There are several tasks the readout chip has to perform starting with the readout of the charge generated by a traversing particle. ROCs amplify and shape the signal, compare it with an adjustable threshold and store the collected charge. In addition the pixel address and the corresponding bunch crossing timestamp is stored. When the L1 trigger decision is positive the information containing pulse height information and the pixel address are send to the periphery.

The ROC is segmented in three regions, the pixel unit cell (PUC) matrix consisting of 80×52 PUCs associated to the sensor pixels, a double column periphery for 160 pixels in each of the 26 double columns and the control and interface block with timestamp and data buffers (see figure 3.11). Additionally the control and interface block is equipped with several settable digital-to-analog converters (DACs). In this thesis only the ones considered in the calibration procedure (see chapter 4 and 5) will be mentioned. A more comprehensive description of the DACs can be found in [Dam09].

Pixel Unit Cell

The PUCs include all required electronics to individually read out the pixels. Figure 3.12 shows a block diagram of the pixel unit cell which is divided into an analog voltage domain and

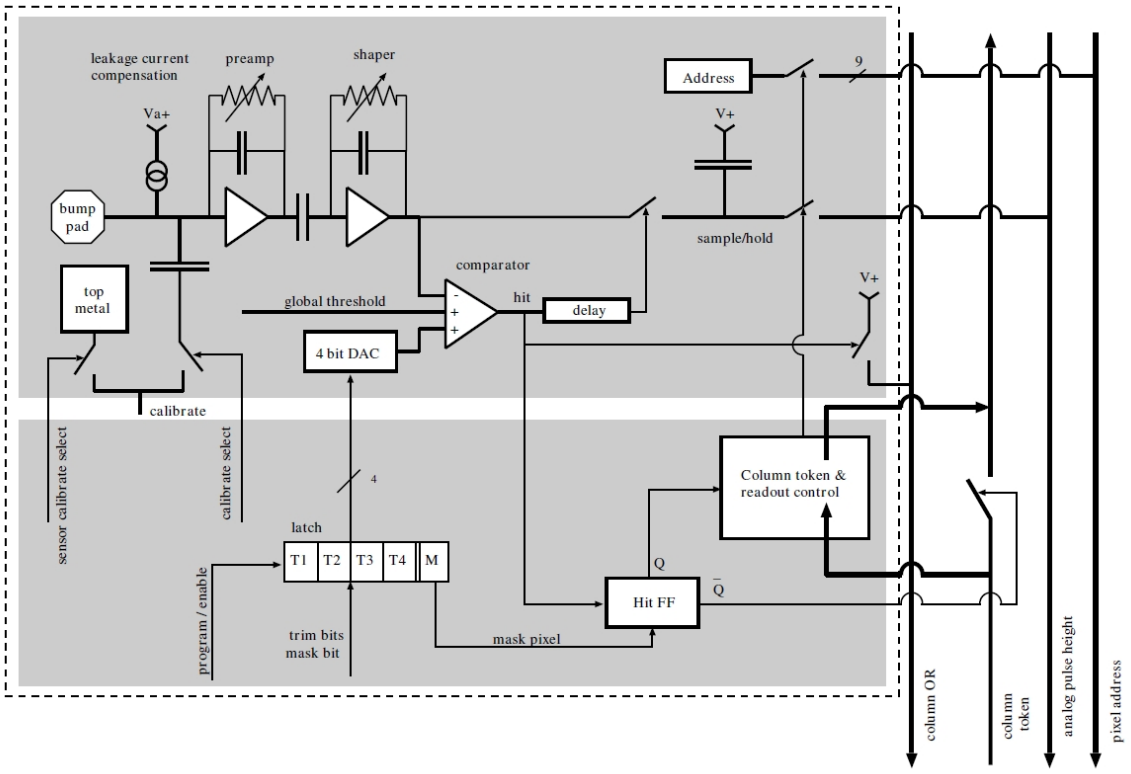

Figure 3.12: Simplified block diagram of a pixel unit cell of the current ROC PSI46V2 with the analog voltage domain in the upper part and the digital voltage domain in the bottom part. The signal that enters the PUC at the bump pad is processed in the pre-amplifier and shaper and compared to a threshold in the comparator. When the signal exceeds the threshold it is stored in the sample and hold capacitance where it waits for a token to be read out. An internal calibration pulse can be injected simulating a signal generated by a particle [Erd10]. Basically this block diagram is comparable to the PSI46dig.

a digital voltage domain. The corresponding DACs to adjust the voltages of these domains are V_{dig} and V_{ana} with the associated currents I_{dig} and I_{ana}. Both are global DACs which means that they are responsible for the entire ROC and are not adjustable for each single PUC.

After charge is generated by a traversing particle and collected by the electric field it enters the PUC via bump bonds (see figure 3.12 upper left region). Then the signal is processed by the pre-amplifier and shaper which are both optimised for fast processing with respect to the short bunch crossing time. The processed signal is then compared to a threshold via a comparator and the corresponding DAC is the VthrComp which is a global one. Nevertheless a fine tuning of the thresholds of each PUC is provided since the performance of each PUC is not 100 % identical. For this fine tuning of the threshold each PUC is equipped with four trimbits (T1 – T4 in figure 3.12). A uniform threshold is desired to assure that each pixel starts to respond at the same value of collected charge. This is important to find correct clusters and achieve the best possible resolution exploiting charge sharing. In addition there is a mask bit (M in figure 3.12) which is required to disable noisy pixels. The threshold of the PSI46V2 is at around 3800 electrons. If a signal exceeds the comparator threshold it is stored in the sample-and-hold capacitance. The sampling point for this capacitance can be adjusted with a delay and the corresponding global DAC VhldDel. An additional global DAC – the Vsf DAC – influences the signal between comparator and signal-and-hold circuit

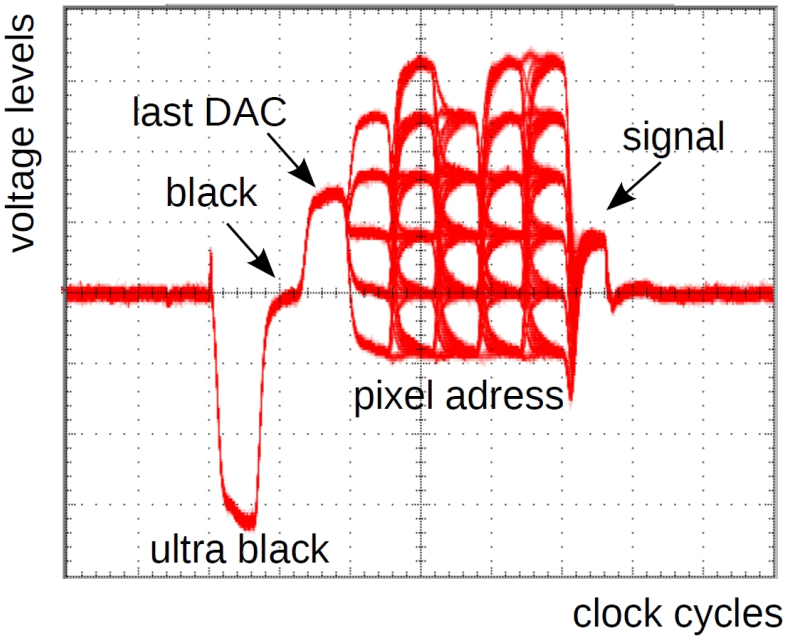

Figure 3.13: Data scheme of the PSI46V2 encoded in analog voltage levels. The first two clock cycles are the ultra black and black level responsible for ROC and TBM header and trailer identification followed by the last DAC used for debugging. The next five cycles provide the pixel address, where the first two encode the double column and the three remaining the row. The encoding scheme is completed by the pulse hight, the only pixel information which is not encoded in a discrete analog voltage level [Gab05].

which is important for the PSI46V2 chip to achieve a linear relation between collected charge and detector signal [Hos12]. The stored charge and the pixel address are read out when a token arrives in the PUC. There is an alternative method to inject calibration pulses into the PUC and simulate charge collected in the sensor. The pulse height of those calibration pulses can be adjusted by the Vcal DAC while the delay of the calibration pulses is set by the CalDel DAC. Also the charge generated by a particle is given in equivalents of the Vcal DAC. There is a low and high 8-bit Vcal register. In the low register one Vcal value corresponds to approximately 65 electrons whereas the values in the high register are multiplied by a factor of seven.

Double Column Periphery and Interface Block of the Readout Chip

The double column periphery and the interface block of the readout chip are presented in figure 3.11 with a periphery length of the PSI46V2 of 1.8 mm. Columns in the ROC are grouped into double columns equipped with one common readout bus, data and timestamp buffer. When a pixel is hit it sends a signal to the timestamp buffer, where a timestamp for this particular hit is stored, and initiates the column drain sending out a column token. All hit pixels open a flip-flop which forces the token to subsequently enter each PUC where it triggers the readout of the pulse height and the pixel address. Since only hit pixels are read out zero-suppressed data is received.

Data Encoding

The entire chip data is encoded in six discrete analog voltage levels except the pulse height information. It is important that the voltage levels are well separated since the decoding relies on predefined address level windows [Erd10]. The data scheme is depicted in figure 3.13

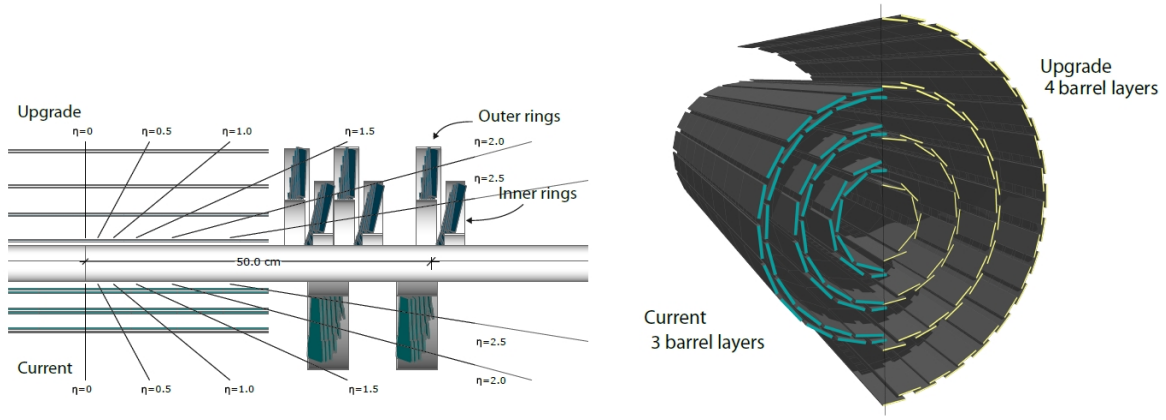

Figure 3.14: Comparison of the current design with the design after the Phase I Upgrade 2016/17. Left: The upper part will be the new design providing four-hit coverage up to $|\eta| = 2.5$ compared to the current design (bottom part) with fewer layers in the barrel and endcap part resulting in two to three penetration points. Right: The current barrel region is depicted in teal while the upgrade barrel region is presented in yellow. After the upgrade the innermost layer has a smaller radius and the new outer layer a significant larger one [D$^+$12].

where the first two clock cycles of the pixel address contain the double column information, followed by three cycles concerning the row. Completed is the hit information by one clock cycle providing the pulse height in a none-discrete voltage level. This data is embedded in headers and trailers from ROC and TBM which coordinates the readout as follows: The TBM sends a token reading out successively the 16 ROCs of a module where each ROC writes its header regardless if it has any hit information. In addition there exists a clock cycle containing the information about the last adjusted DAC which is used for debugging.

3.2.2 The CMS Pixel Detector before and after Phase I Upgrade

The CMS pixel detector was designed for a luminosity of $\mathcal{L} = 1 \times 10^{34}\text{cm}^{-2}\text{s}^{-1}$, however twice this value will be reached after LHC long shutdown in 2013/14. This will lead to a significant increase of simultaneous particle collisions (pile-up), exceeding buffer capacities resulting in an undesirable amount of data loss. For instance the average rate at the new innermost layer will increase from 120 MHz/cm^2 to almost 600 MHz/cm^2. Furthermore the increased pile-up of up to 100 would lead to a loss of efficiency of roughly 50 % (for $\mathcal{L} = 2 \times 10^{34}\text{cm}^{-2}\text{s}^{-1}$ at 50 ns bunch crossing time) in the current innermost layer. Therefore the entire CMS pixel detector will be replaced in the CMS Phase I Upgrade 2016/17.

A basic difference will be the additional barrel layer as well as the additional endcap on each side. In the barrel region the number of sensitive layers will not only be increased but the innermost layer gets even closer to the interaction point. This modification is desired in order to achieve a better secondary vertex resolution for particles like b-quarks or τ-leptons. This becomes possible since it is planned to install a smaller beam pipe during the long shutdown 2013/14.

Figure 3.14 compares the current design with the one of the Phase I Upgrade. Aside from the smaller radius of the innermost layer the fourth layer will close the gap to the micro strip detector. With the new design the pixel detector will provide four-hit-coverage up to a pseudo rapidity of $|\eta| \lesssim 2.5$. Four-hit-coverage is desired to improve the track finding and to assure good vertex reconstruction at higher pile-up. The layers in the new design will be mounted at radii of 2.9 cm, 6.8 cm, 10.2 cm and 16.0 cm.

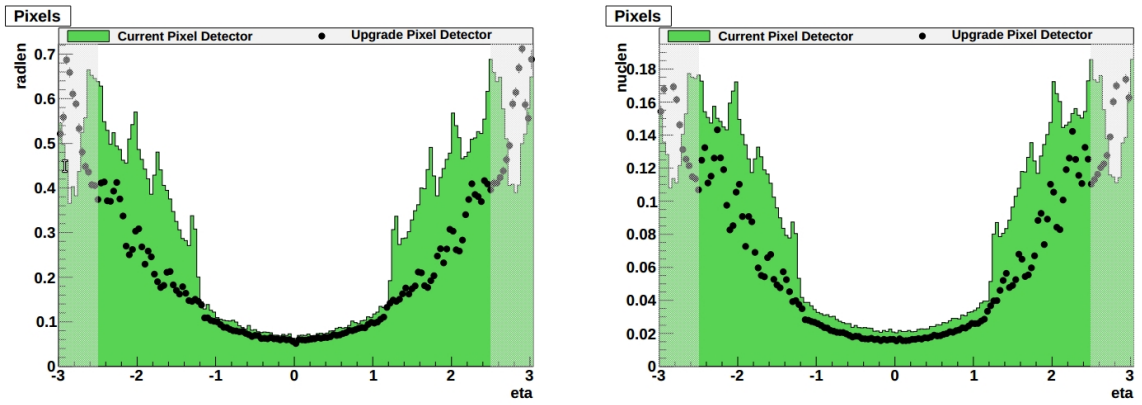

Figure 3.15: The material budget of the pixel detector is displayed as a function of the pseudo rapidity η. In the left plot the amount of material is presented in units of radiation length and in the right plot in units of nuclear interaction length. The green histogram is associated with the current pixel detector and the black points with the Phase I Upgrade detector. Light regions at pseudo rapidity above $|\eta| > 2.5$ are outside the sensitive region for track reconstruction [D+12].

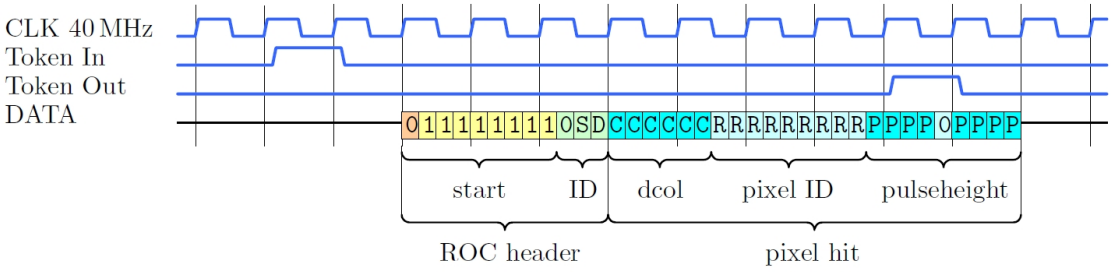

Figure 3.16: The data format of the PSI46dig consists of a 12-bit ROC header followed by one or more pixel hits while the data stream starts one clock cycle after the Token In. Hits consist of 6 bits for the double column, 9 bits for the row (pixel ID) and 8 bits for the pulse height with an additional zero in the pulse height bits avoiding fake headers [Spa12].

In spite of the additional layers the material budget will be reduced in the sensitive volume. Figure 3.15 illustrates a comparison of the material budget in units of radiation length (radlen) and in units of the nuclear interaction length (nuclen) both as a function of the pseudo rapidity η. The shaded bands at $|\eta| > 2.5$ are outside the region for track finding. The material reduction is achieved by an ultra-lightweight support with CO_2 cooling and by moving passive material such as the electronic boards and connections out of the tracking volume.

Data encoding after Phase I Upgrade

An on-chip 8-bit analog-to-digital converter (ADC) digitises the pulse height information running at 80 MHz. The data output consist of a 12-bit ROC header and is followed by 24-bits per hit pixel. Figure 3.16 displays the detailed composition of the data format for a one pixel hit. The data stream begins one clock cycle after the Token In (sent from TBM) starting with a 0 and eight consecutive 1 and is completed with a further 0 plus two reserved status bits S and D. The next six bits contain the double column information (CCCCCC) followed by nine bits for the pixel information (RRRRRRRRR). These 15 pixel coordinate bits are written in Gray Code, a binary code in which successive numbers differ only in one bit [Gra53]. The last nine bits contain the pulse height information providing a range of 0-255.

A zero in the middle of the nine bit pulse height block avoids fake ROC headers. The ROC information – including all hit information – is embedded in the TBM header and trailer both starting with a 12-bit identification sequence followed by 24 bits for trigger and status information. The readout of the 16 ROCs – coordinated by the TBM – is parallelised by reading out four ROCs at the same time, afterwards the collected data leaves the module.

There are two different column drain mechanisms for the PSI46dig one for layer 2-4 ROCs which is basically the same as the one of PSI46V2 and a modified one for the layer 1 ROC to reduce column drain dead times with respect to the high flux in the innermost layer. Instead of a simple subsequent process the column drain of the layer 1 ROC performs a 4-by-4 cluster search resulting in a gain of the data rate by a factor of 1.8 [D$^+$12].

Table 3.1 compares the current ROC PSI46V2 and the new ROC PSI46dig.

Table 3.1: Comparison of the current ROC PSI46V2 with the new one PSI46dig. The values in brackets are the ones for layer one equipped with the advanced version of the PSI46dig [D$^+$12].

	PSI46V2	PSI46dig
ROC size	7.9 mm × 9.8 mm	7.9 mm × 10.2 mm
Pixel Size	150 µm × 100 µm	150 µm × 100 µm
Radius of layer one	4.3 cm	2.9 cm
Adjustable DACs	26	19
Charge/Address readout	analog	digital
Readout speed	40 MHz	160 Mbit/s
Timestamp buffer	12	24
Data buffer	32	80
Additional output buffer	no	yes
Double column speed	20 MHz	20 MHz (40 MHz)
in-time threshold	3500 electrons	< 2000 electrons
PLL	no	yes
Data loss at maximal flux	≈ 3.8 % at 120 MHz/cm^2	1.6 % at 150 MHz/cm^2 (≈ 3 % at 580 MHz/cm^2)
TBM readout	serial	parallel

The new readout protocol – based on 160 Mbit/s LVDS – which increases the readout link speed requires several modifications.

- The generation of a 160 MHz clock within the ROC from the 40 MHz clock and a PLL to adjust frequency and phase.
- A 160 MHz data serialiser.
- Digital LVDS out devices.
- An 8-bit ADC which encodes the analog pulse height information.
- An event builder for the digital data format.

The improvements due to this modifications are the increased readout speed as well as the avoidance of the multilevel analog decoding. Due to the increased number of buffers the periphery length increased (by 0.4 mm), too. The number of DACs is reduced because some are exchanged by fixed voltages or currents as they have never been modified from the default

value. A significant reduction of the in-time threshold was achieved by reducing the internal crosstalk. The current TBM with serial readout will be replaced by a TBM reading out four ROCs in parallel. All other noted items in table 3.1 have been discussed previously [D$^+$12].

3.2.3 Module Production

For the entire barrel pixel detector 1184 modules plus spares have to be build. The total number of pixels in the barrel region will increase from 48 million to 79 million. Institutes from all over the world are participating at the production of the pixel modules. The four German institutes KIT[1], RWTH Aachen[2], University of Hamburg and DESY[3] are responsible for layer four consisting of 512 modules. Half of the modules for this layer are assembled and pre-tested at the Karlsruhe Institute of Technology. For the module evaluation calibration measurements with monochromatic X-rays are planned. Therefore this thesis deals with the new ROC PSI46dig to gain calibration experience and to obtain know-how concerning the performance of the new ROC.

[1] Acronym: Karlsruhe Institute of Technology
[2] Acronym: Rheinisch-Westfälische Technische Hochschule Aachen
[3] Acronym: Deutsches Elektronen-Synchrotron

4. Test Setups and Equipment

In the previous chapters the general context of this thesis was given, whereas in this chapter the concrete topic is described. First of all a definition of calibration is introduced and the intention why a calibration of the detector is necessary is given. Further the test samples and test setups are described as well as the software for the pre-calibration adjusting the DACs and for X-ray calibration is explained. Moreover different methods of the X-ray calibration are introduced together with important testing parameters.

4.1 Motivation

Calibration is the adjustment of a device by comparing measurement data with a reference signal [Dud13]. In case of the CMS pixel detector this means that the detector signal read out from the ROC is a voltage given in ADC units and is converted into Vcal units using a chip internal pulse height calibration. The pulse height calibration is a part of the pre-calibration explained in this chapter (section 4.5). Additionally there is a different procedure the X-ray calibration which is subsequently also denoted as calibration.

The calibration is used to investigate the relation between detector signal – typically given in Vcal – and deposited energy in the sensor. This is necessary as charge sharing (see section 3.2) is exploited and therefore the spatial resolution depends on this relation. In detail this means, if charge is spread over two (or more) pixels, the resolution depends on how accurately the corresponding proportionality can be established.

According to the definition above the calibration relies on reference signal of known energy deposited in the sensor. For instance charged particles with a known energy amount described by the Bethe equation 3.1 can serve as such a reference signal. Another alternative are for instance monochromatic X-rays in an energy range of keV which can be obtained from the K_α transition of electrons in atomic shells. Subsequently photons with material dependent energy are named characteristic photons. In the calibration procedure photons are applied as they provide several advantages over charged particles.

- Photons with K_α energy can simply be produced by excitation of a target material e.g. by irradiating it with an X-ray tube or a radioactive source.
- Due to the energy range of the available characteristic photons (see table 4.1) the interaction mechanism is mainly the photo effect (see figure 3.6). Therefore the photons either deposit all their energy in the sensor of do not interact at all.

- In case of characteristic photons the distribution of the deposited energy in the detector is a Gaussian while charged particles provide a Landau distribution. The energy of characteristic photons can simply be determined by calculating the mean of a Gaussian fit.

For the reference signals of the calibration process different target materials are used providing a set of characteristic photons shown in table 4.1. Aside from the K_α transition energies E_{K_α} the expected number of electrons N_{el} is given. Since in silicon 3.6 eV are required to create an electron-hole pair N_{el} can easily be calculated (noted in table 4.1).

$$N_{el} = \frac{E_{K_\alpha}}{3.6\,\text{eV}} \tag{4.1}$$

In the calibration process the sensor is irradiated with characteristic photons, their energy is calculated and the number of expected electrons is plotted as a function of the measured energy given in Vcal units. Then a linear fit is applied where the slope is the proportionality factor between detector signal and deposited energy. An exemplary calibration curve using six targets is shown in figure 4.1. The highlighted red vertical band illustrates that the absolute value of the detector signal depends on several parameters.

Table 4.1: List of the applied target materials presenting their K_α transition energies as well as the expected number of electrons N_{el} created via the photoelectric effect [NIS13].

Target	E_{K_α} [eV]	N_{el}
Fe	6403.13	1779
Cu	8048.11	2236
Zn	8639.10	2400
Rb	13 395.05	3721
Mo	17 479.10	4855
Ag	22 162.99	6156
In	24 209.78	6725
Sn	25 271.34	7020
Ba	32 192.87	8942
Nd	37 361.40	10 378
Tb	44 485.90	12 356

4.2 Equipment

In this subchapter the equipment which is used in the calibration process is introduced. First of all there are the test samples consisting of different versions of the readout chip. Afterwards the testboard used for the readout of the ROCs is described and finally the test setups are presented.

4.2.1 Test Samples

Single chip sensors are a convenient device to investigate the calibration procedure. Just as a module a single chip sensor consists of a sensor and a ROC connected via bump bonds, however they are equipped with one ROC only. An advantage is that single chip sensors provide a simplified test setup and readout. They are glued on a printed circuit board (PCB)

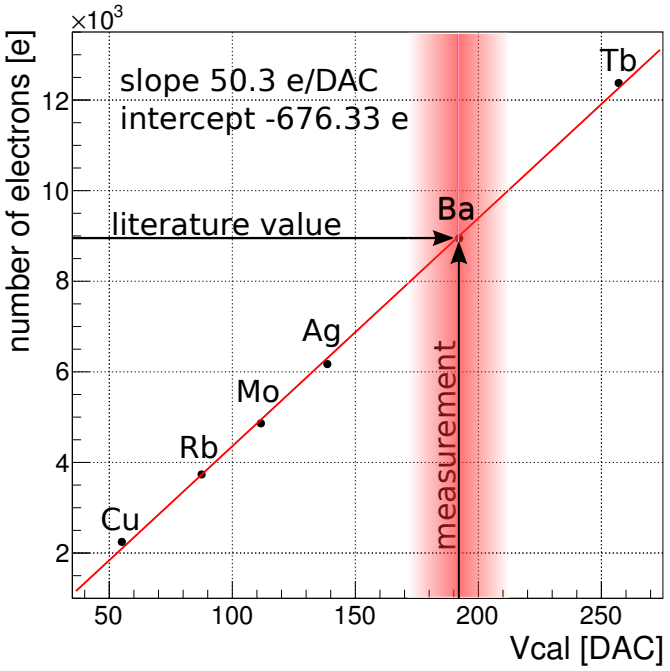

Figure 4.1: The expected number of generated electrons corresponding to the theoretical K_α transition energy is plotted as a function of the measured detector signal given in Vcal. A linear fit (the calibration curve) is applied where the slope is the proportionality factor between detector signal and deposited energy. The highlighted red vertical band illustrates that the absolute value of the detector signal depends on various parameters which will be investigated in chapter 5.

which distributes power and trigger information and in contrary to a module a single chip sensor holds no TBM and HDI.

The investigated single chip sensors are the digital versions of the ROC for the Phase I Upgrade. The available set is comprised of three PSI46digV1 with the institute internal denotation ROCdigV1 and two PSI46digV2, internally denoted as ROCdigV2. As visible in figure 4.2 they use the same PCB design with plastic caps protecting the wire bonds connecting PCB and ROC respectively sensor. Most measurements are performed with the ROCdigV1's since the ROCdigV2 become available only near the end of this thesis. Although this thesis is dedicated to the digital versions of the ROC it also deals with results of the analog version PSI46V2 from [Hos12].

4.2.2 Test Board

Another necessary component in the testing process is the CMS pixel PSI46 test board presented in figure 4.3. The test board and test samples are connected via an additional adapter board while the communication between them is based on the Inter-Integrated Circuit (I^2C) protocol used for programming the ROC [Sem13]. An USB 1.0 connection provides the communication between PC and test board while a Field Programmable Gate Array (FPGA) including a processor is located at its centre. Due to the processor it is possible to perform tests on-board and increase the testing speed by a factor of three to four compared to PC based testing [Trü08]. The test board supplies trigger and clock signal as well as a 64 MB memory for temporary data storage and is powered by a 12 V power supply. Additionally it is possible to route the sensor bias voltage via the test board if the voltage is not directly connected to the PCB of the test sample.

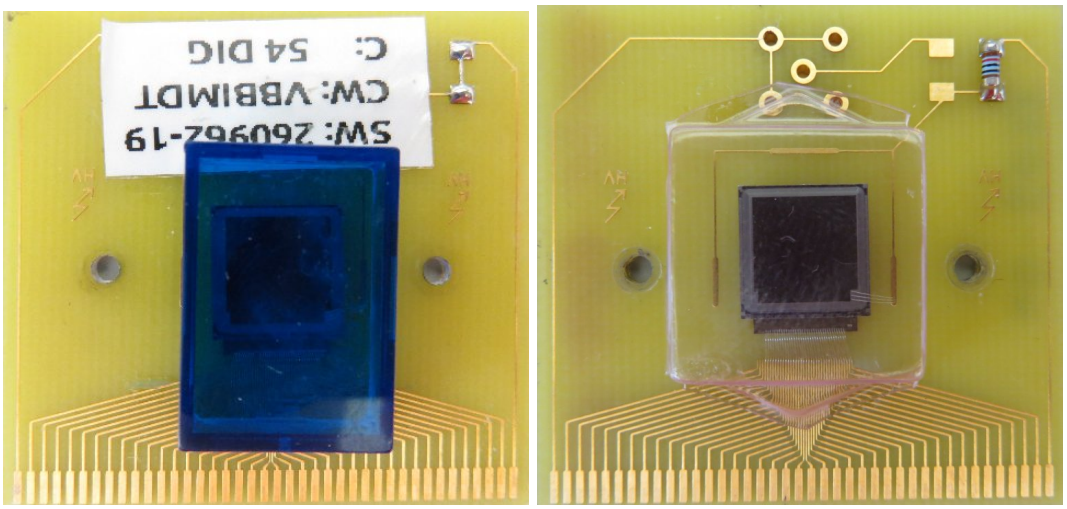

(a) PSI46digV1 (b) PSI46digV2

Figure 4.2: Photos of the investigated single chip sensors mounted on identical PCB. Plastic caps are attached to protect the wire bonds connecting the PCB with ROC and sensor. In (a) the PSI46digV1 is shown with the institute internal denotation ROCdigV1 and (b) depicts the PSI46digV2 denoted as ROCdigV2.

4.2.3 Trigger and Stretched Clock Cycle

The test board – responsible for the triggering in the laboratory – provides two trigger modes.

- Scintillator trigger: This trigger is realised by a scintillator underneath the single chip sensor. When a particle is detected in the scintillator the readout of the ROC is triggered to receive the hit information of this certain particle. Unfortunately this trigger type is only accessible for charged particles as characteristic photons cannot interact with the sensor and with the scintillator because they interact via the photoelectric effect. There are still some reasonable applications for the scintillator trigger, however this mode is not considered within this thesis since only characteristic photons are applied. Further information for applications can be found for instance in [Spa12].
- Random trigger: In this mode the test board simply sends triggers with constant frequency and without hit correlation, hence the read out data also contains empty events. All measurements in chapter 5 are performed with the random trigger.

The test board clock runs with a frequency of 40 MHz with respect to the 25 ns bunch crossing time of the LHC. This means that hits recorded within a 25 ns clock cycle are read out after a trigger arrives. After the hit information is read out, 64 µs− 25 ns (denoted as inactive time) pass until the next trigger arrives. A drawback of the random trigger is the small statistics of measurements with reasonably low radiation rates. To improve statistics the time interval (measured in clock cycle) in which pixels collect charge – subsequently denoted as active time – may be extended. The factor stretching the active time is called stretched clock cycle (*scc*). In this thesis *scc* values up to 1000 are applied. The scc only stretches the active timeframe while the inactive time stays untouched as illustrated in figure 4.4. According to this the trigger rate depends on the *scc* value and is described by the following equation:

$$f_{trig} = (64\,\mu s - 25\,ns + (25\,ns \cdot scc))^{-1} \tag{4.2}$$

The rates used for the measurements have a range from 15 625 Hz (*scc* = 1) to 11 239 Hz (*scc* = 1000). To benefit from the stretched clock cycle it is necessary to relate hit information

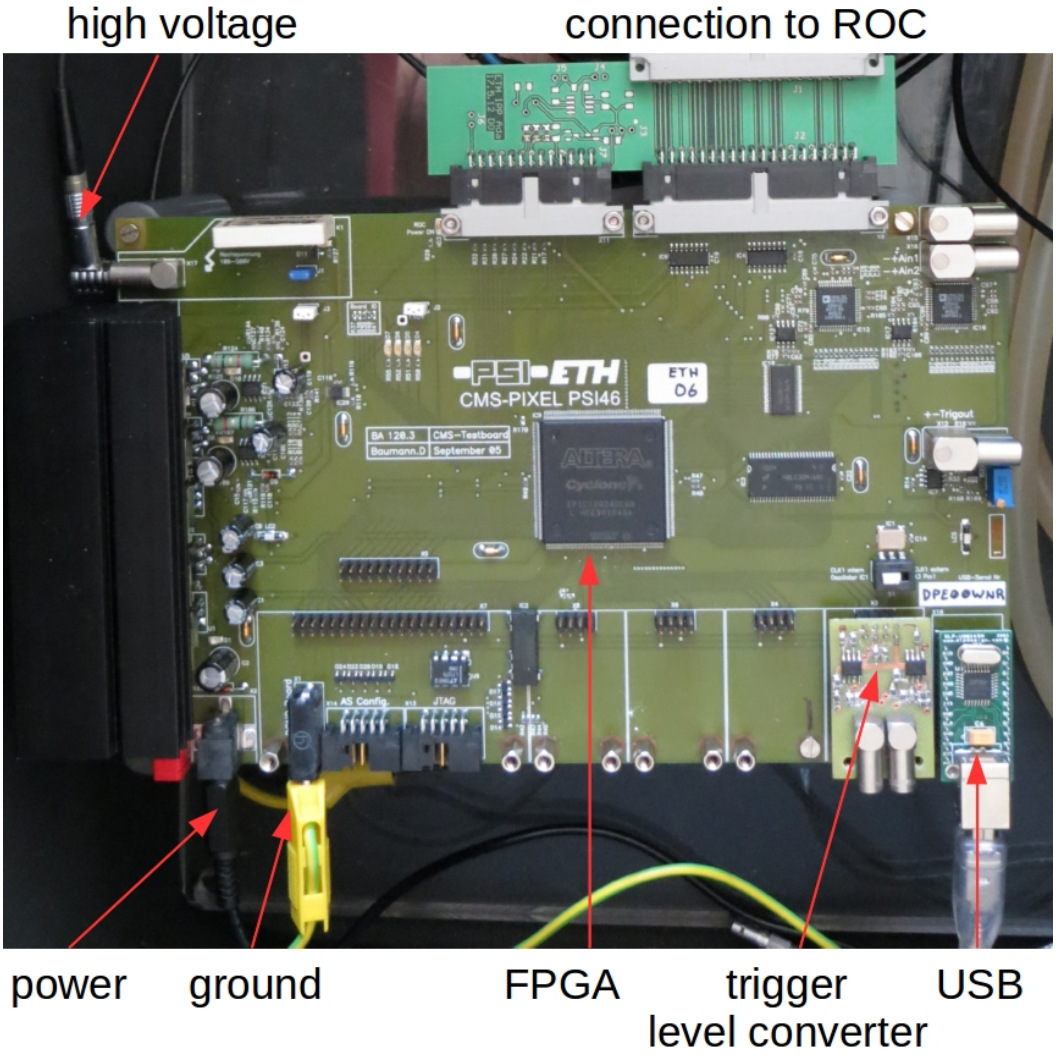

Figure 4.3: CMS pixel PSI46 test board including FPGA, adapter board for the connection to the test samples, USB connection to the PC, high voltage for biasing the sensor and test board power supply.

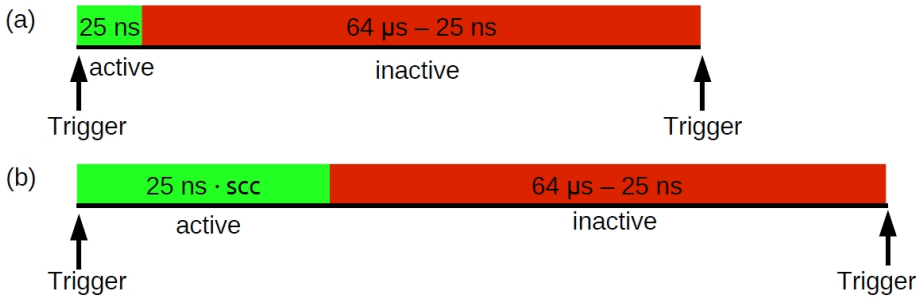

Figure 4.4: A sketch explaining the working principle of the stretched clock cycle *scc*. (a) shows the unstretched clock cycle with an active timeframe of 25 ns and an inactive timeframe of 64 µs− 25 ns. In (b) the stretching of the active timeframe is illustrated while the inactive one stays constant [Hos12].

in the ROC buffers correctly with the stretched test board block cycle. The delay between test board and ROC can be adjusted via a register called Write Bunch Crossing (WBC). When no clock cycle is stretched ($scc = 1$) it is not necessary to find a correlation to a certain clock cycle as they are all equal. For $scc > 1$ it is required to trigger a stretched clock cycle containing more hits. If the WBC is not correctly adjusted an unstretched clock cycle is read out and the higher probability to obtain additional hits is lost.

4.3 Test Setups

There are two test setups both used in the calibration procedure. In each setup the test samples are irradiated with characteristic photons relying on excitation of exchangeable targets. An advantage of two setups is to verify results easily. On the basis of measurements, improvements of the both setups are planned and implemented step by step.

4.3.1 X-ray Tube Setup

The first setup to introduce relies on a 2000 W X-ray tube powered by a General Electric ISOVOLT 3003 generator providing a continuous X-ray spectrum. An acceleration voltage up to 60 kV is supported with an adjustable tube current from 2 mA to 33 mA. Figure 4.5 shows a photo of the X-ray tube setup and illustrates the basic operating principle. The primary beam (depicted by the red vertical arrow) leaves the X-ray tube and hits the target mounted on a tiltable aluminium holder usually adjusted at 45 °. The target material excited by the primary beam emits target dependent characteristic photons – also denoted as secondary beam – irradiating the single chip sensor. Moreover this setup is equipped with two lasers to align the target respectively the beam spot exciting the target. For the X-ray tube setup different targets available – as the ones presented in figure 4.6 – with a wide range of K_α energies. They comprise copper (Cu), zinc (Zn), molybdenum (Mo), silver (Ag), indium (In), tin (Sn) and neodymium (Nd). Several *Pt1000* temperature sensors [DIN08], a Peltier element and a fan for cooling the Peltier element at the backside of the single chip sensor guarantee a stable temperature, however this cooling only provides temperatures around room temperature. A slight difference between figure 4.5 and the actual setup is the location of the test board. As the test samples – which are PSI46dig ROCs – have to be connected directly to the test board this is placed vertically underneath the test sample. In addition aluminium layers with different thicknesses can be mounted in the secondary beam serving as shielding and manipulating the rate.

The readout PC outside the box hosting all mentioned components runs with Scientific Linux 5 and is connected via a USB cable to the test board. Further the PC is connected to

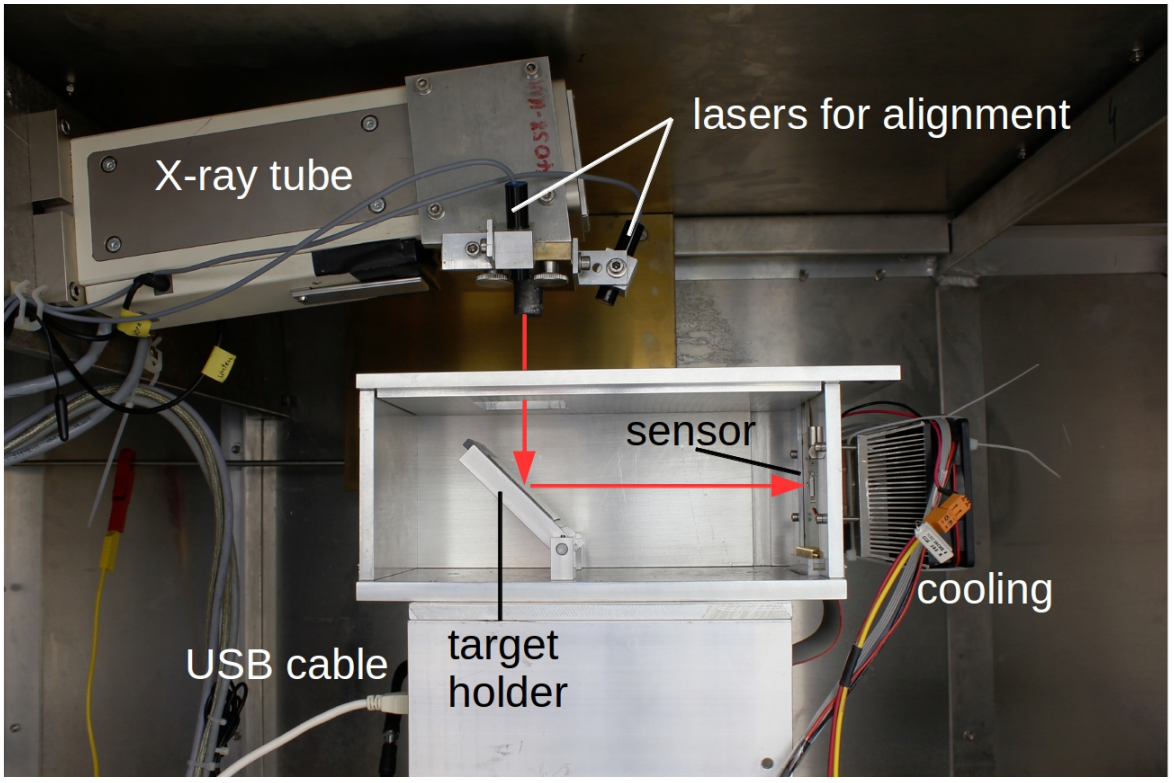

Figure 4.5: X-ray tube setup for detector calibrations. The primary beam depicted by the red vertical arrow excites the target material mounted on a tiltable holder and two lasers are mounted to align the beam spot. The emitting characteristic photons depicted by the red horizontal arrow irradiate the sensor of a test sample cooled by a Peltier element. The test board in this figure is located beneath the aluminium shielding connected to the USB cable. For the investigation of PSI46dig ROCs the test board had to be moved below the test sample since it is not possible to establish a reasonable connection between test board and PSI46dig ROCs via cable.

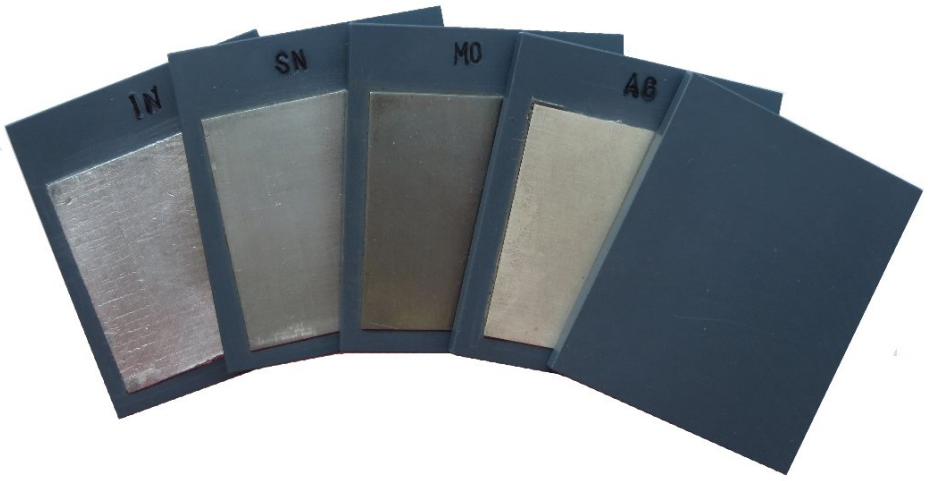

Figure 4.6: Target material used in the X-ray tube setup. Layers of indium, tin, molybdenum or silver are glued on top of a PVC substrate and can be assembled easily on the target holder presented in figure 4.5. Additionally a PVC dummy target without a metal layer for background measurements is shown.

the temperature devices and the X-ray tube generator while the control of these is realised by programs based on National Instruments LabVIEW [Lab13]. The last part to mention is a Keithley 2410 High-Voltage SourceMeter supplying the bias voltage and measures the sensor leakage current [Kei13].

The X-ray tube provides rates of up to 6.5 MHz/cm^2 in the secondary beam depending on the target. Together with the opportunity to mount a shielding a wide range of rates is accessible enabling detailed investigation of rate dependences.

4.3.2 Source Setup

The second test station is the source setup for instance equipped with an ^{241}Am source. An aluminium box (see figure 4.7) houses basically the same parts as the box of the X-ray tube setup (see figure 4.5). Differences in the setup concern the cooling and the irradiation of the single chip sensors. The cooling is more complex, consisting of a copper bridge equipped with two Peltier elements, one on each side of the bridge. Instead of a fan the backsides of the Peltier elements are cooled by a water cooling system achieving temperatures down to about $-30\,^{\circ}$C on the sensor surface. The temperature is controlled by the same LabVIEW software as used in the X-ray tube setup. Additionally the test sample, the copper bridge, Peltier elements as well as temperature and humidity sensors are embedded in a plastic box while the ^{241}Am source is located on top of this box. Moreover the aluminium box and the plastic box are flooded with dry air to prevent condensation on electrical parts.

A drawing of the ^{241}Am source is depicted in figure 4.8 showing the shielded ^{241}Am source emitting photons (the α particles with an energy of 5.5 MeV are not able to leave the source since it is closed [P$^+$95]). The ^{241}Am source irradiates one of the six target materials mounted on a rotatable target holder while the characteristic photons are emitted through a small outlet opening. The available targets are copper (Cu), rubidium (Rb), molybdenum (Mo), silver (Ag), barium (Ba) and terbium (Tb). According to latest measurements the primary ^{241}Am source has an activity of about 3.55×10^8 Bq [Woc13], however this provides only low rates of characteristic photons up to 1.2 kHz/cm^2. In addition a scintillator trigger is placed below the single chip sensor which is only usable associated with the available Sr^{90} β-source.

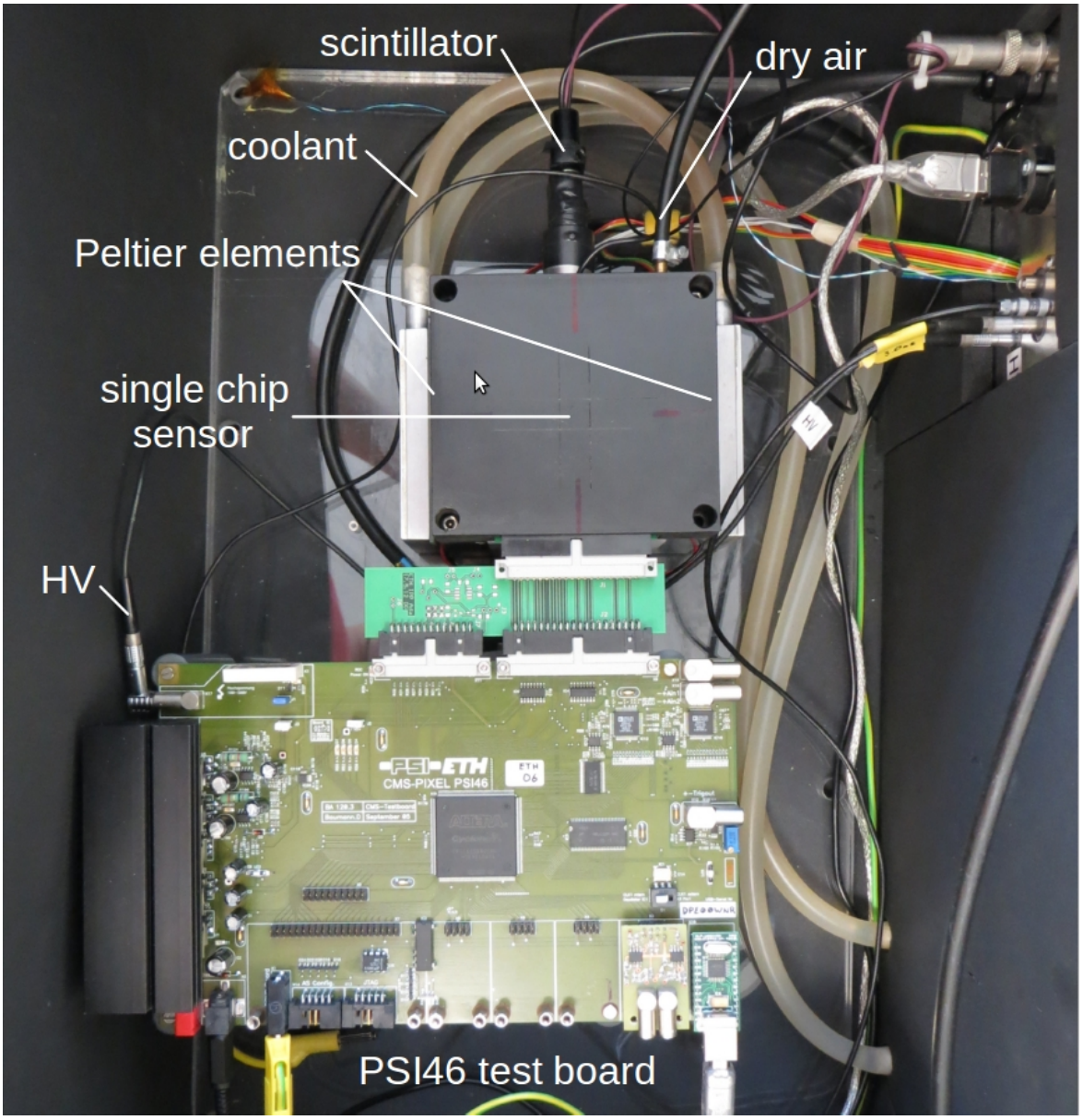

Figure 4.7: Inside view of the aluminium box housing basic parts of the source setup. The visible parts are: The PSI46 test board, a high voltage connection for the bias voltage, two Peltier elements plus the coolant building up the cooling system, a scintillator as well as a tube providing dry air. The position of the single chip sensor is indicated underneath the black plastic cover while the ^{241}Am source would be located on top of that cover.

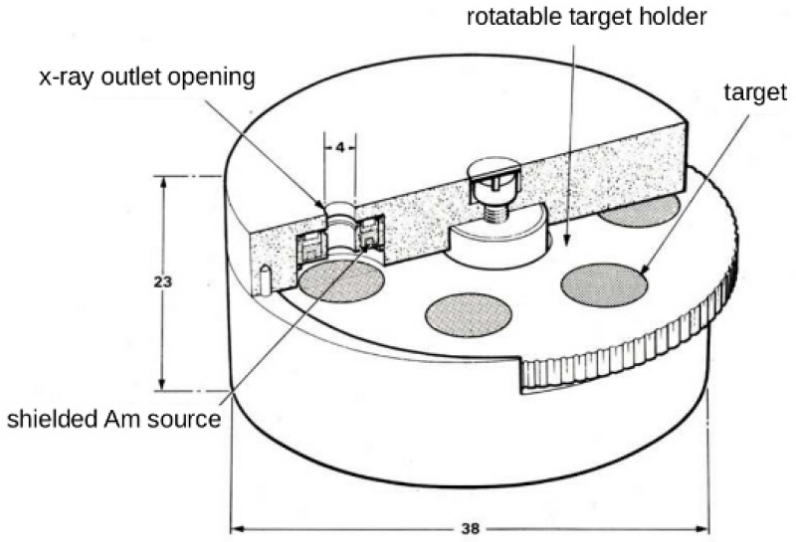

Figure 4.8: Drawing of the structure of the ^{241}Am source. The shielded primary α-source irradiates and excites the target materials which are mounted on a rotatable target holder. Emerging characteristic photons leave the source via an outlet opening [Woc13].

Outside the aluminium box are a Linux based PC, a Keithley 2410 Hight-Voltage SourceMeter for biasing the sensor and measuring its leakage current, two power supplies for the scintillator and Peltier elements plus a water chiller for cooling the backside of the Peltier elements. A drawback of the source setup is the relatively low rates compared to the X-ray tube setup but in return this setup provides measurement temperatures from 20 °C down to −30 °C.

4.4 Software

The software packages used for the pre-calibration as well as the X-ray calibration are written in C++ and run on Linux PCs while the ROOT and EUTelescope frameworks are used for analysis [BR97, B$^+$07]. The psi46expert[1] software package provides all testing algorithms for the electric pre-calibration, threshold measurements (in-software denotation X-ray) and spectrum measurements (in-software denotation HR-PixelMap). TakeData is the other software package used in this thesis providing hit information of pixels only. Both are GUI[2] based and provide the opportunity to adjust several parameters within the interface. TakeData supports for instance adjustment of the trigger mode, WBC and duration while psi46expert enables the adjustment of all DACs including WBC. During data acquisition both obtain binary files containing the raw measurement data followed by different analysis processes. In case of psi46expert the data is only temporarily stored and translated into ROOT trees by implemented scripts accessed by the HR-PixelMap routine. TakeData saves the binary data files permanently on the PC which in turn have to be analysed with an EUTelescope based script called Marlin analysing the data and storing the resulting plots in a ROOT tree. The spectra obtained with both software packages after storing them in ROOT trees have to be further analysed with ROOT. For this purpose several scripts exist as well as basic ROOT features to apply Gaussian fits as shown in figure 4.9.

[1] The latest psi46expert versions are available at `https://svnweb.cern.ch/cern/wsvn/psiexpert`
[2] Acronym: graphical user interface

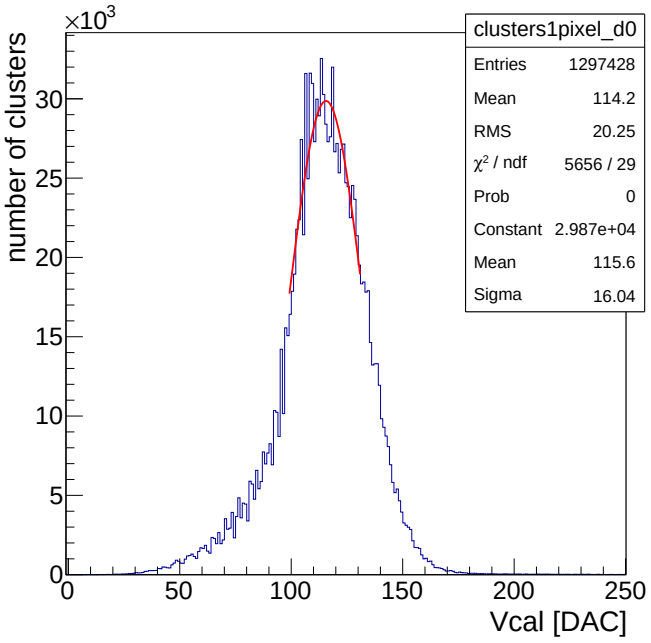

Figure 4.9: Energy distribution of characteristic photons in the sensor including a Gaussian fit and various parameters such as the mean of the distribution and the mean of the fit.

4.5 Pre-Calibration

An essential step before the data taking is started is the electric pre-calibration implemented in the psi46expert software package. The pre-calibration consists of several routines to check the functionality and to find an optimal set of DAC parameters. This procedure has to be performed for each single ROC as they all behave at least slightly different. Further new pre-calibrations are required when conditions have changed as for instance an adjusted temperature. Irradiation is not required to perform the routines of the pre-calibration as all signals are injected by the ROC internal calibration unit as described in section 3.2.1.

4.5.1 PreTest

The first test of the pre-calibration routine is the PreTest consisting of:

- Loading various parameters from configuration files.
- Test if the DACs of the readout chip are programmable.
- Adjustment of V_{ana}, CalDel and VthrComp.
- Saving the adjusted parameters in a dedicated file.

4.5.2 FullTest

The next step in the pre-calibration procedure is the FullTest which performs some basic functionality tests.

- Pixel alive test: Within this test the functionality of the masking bit is checked. Each pixel is equipped with such a bit used to disable single pixels in case they are noisy. Additionally calibration pulses are injected into the analog part of the PUC and it is checked whether there is a change in the readout data compared to the data obtained without calibration pulses. When both tests are successful the pixel is declared alive.

- Bump bonding test: In this test calibration pulses are injected capacitively into the sensor via a top metal pad (see figure 3.12) generating a signal which is measured. This process is repeated, however a switch is opened and the signal is not injected into the sensor hence only the crosstalk in the PUC is measured. The corresponding signals of both methods are compared, if there is no difference the bump of the tested pixel is marked dead.
- Address decoding: This test checks if each pixel generates its address correctly.
- Trim bit test: The trim bit test simply checks if the threshold of a pixel can be changed by disabling one trim bit. This test only checks the functionality of the trim bits and is not the actual trimming.
- Temperature calibration: This measurement relies on a chip internal temperature sensor, however the PSI46dig ROCs are not equipped with this sensor making this test redundant.

4.5.3 Trimming

In the first step of the trimming routine the DAC VthrComp responsible for the global comparator threshold is adjusted where low VthrComp values correspond to high thresholds and vice versa. For this purpose a certain calibration pulse (within this thesis mostly 35 Vcal) is injected while the comparator threshold is varied to find the VthrComp value corresponding to the calibration pulse. Since all PUCs perform slightly differently they obtain various VthrComp values, however this is a global DAC and cannot be adjusted individually for each PUC. Hence the value is selected corresponding to the pixel with the highest threshold. In a second step the DAC Vtrim is adjusted which sets the value by which the threshold is decreased per disabled trim bit. Finally the threshold closest to the target threshold is determined by consecutively disabling all possible trim bit configurations. Additional information concerning the trimming is available in [Trü08].

4.5.4 Pulse Height Calibration

This routine deals with the behaviour of the charge read out of the PUC as a function of the charge initially created which is ideally a linear relation. In the following the amount of charge which is read out also refers to the notations (detector) signal and pulse height each measured in ADC counts with one ADC corresponding to 0.1275 mV. During the routine Vcal calibration pulses with increasing strength are injected into the ROC and the corresponding pulse heights are measured for each pixel. These pulse heights are fitted by a hyperbolic tangent function providing an almost linear relation in the interesting Vcal range:

$$y = p_3 + p_2 \cdot \tanh\left(p_0 \cdot x - p_1\right). \tag{4.3}$$

The inverse of the mentioned fit function translates ADC values obtained in X-ray calibrations into Vcal values.

4.5.5 S-Curve

The final procedure in the pre-calibration is the S-curve investigating the noise to identify pixels which have to be masked. In this routine Vcal calibration pulses with increasing strength are injected observing the response efficiency given by the ratio of received to sent pulses. Ideally the efficiency is 0 % for calibration pulses below the threshold and 100 % for pulses above. Actually the detector performs as follows. As long as the injected calibration pulses are far below the threshold the efficiency is 0 % and starts to increase when the Vcal

pulses get closer to the adjusted threshold. Once they are distinctly above the threshold an efficiency of 100 % is reached. The desired step function is smeared out by noise which can be fitted by a error function. The width of this fit is proportional to the noise of a pixel, however this describes the noise of the amplifier and shaper in the PUC only. This noise of approximately 200 electrons is relatively low compared to at least 1500 electrons of the comparator threshold hence the detector performance is not limited by the noise of the PUCs.

Figure 4.10 shows the summary page presenting several plots associated with the pre-calibration routines. Not all plots are filled with reasonable values as they were originally designed for the PSI46V2. Table 4.2 shows the durations of all pre-calibration routines.

Table 4.2: List of the routines of the pre-calibration and the corresponding durations, however the test is not yet optimised for the digital ROCs.

Routine	duration [s]
PreTest	25
FullTest	175
Trimming	165
PH-Calibration	350
S-Curve	105
Total	820

4.6 Different Methods of Data Acquisition

When the pre-calibration is finished the X-ray calibration is performed to obtain the relation between generated charge and detector signal. For this purpose are two methods available providing different operating principles.

4.6.1 Spectrum Method

In the spectrum method charge is generated in the sensor and read out using the entire readout chain. The corresponding pulse heights are measured in ADC counts which in turn are converted into Vcal values and filled into a histogram. In case of characteristic photons a Gaussian fit is required where the mean of the fit provides the energy of the photons given in Vcal (for charged particles a Landau fit is necessary). Such a fit is presented in figure 4.9. Calibration with the spectrum method may be performed with TakeData and the HR-PixelMap routine of the psi46expert software package.

4.6.2 Threshold Method

The second option is the threshold method. First the comparator threshold is decreased in steps and the number of hits exceeding the threshold are counted for each step. Starting with high thresholds yields no hits. When the thresholds get closer to the measured signal the number of hits increase and saturate once the threshold is low enough to detect all hits. This plateau is followed by a steep increase in the number of counted hits as soon as the threshold is below the sensor noise level, however this region is not considered in the analysis. The next step is the application of an error function fit. While the VthrComp is determined to the value where the error function reaches 50 % of the saturation plateau. Afterwards this VthrComp is set and the associated Vcal value is identified by comparing rising Vcal calibration pulses with the threshold (the irradiation should be stopped at this point as internal pulses are used). A major difference between both methods is that the threshold method does not use the whole readout chain to measure the Vcal pulse height. It leaves out the entire sample and hold circuit.

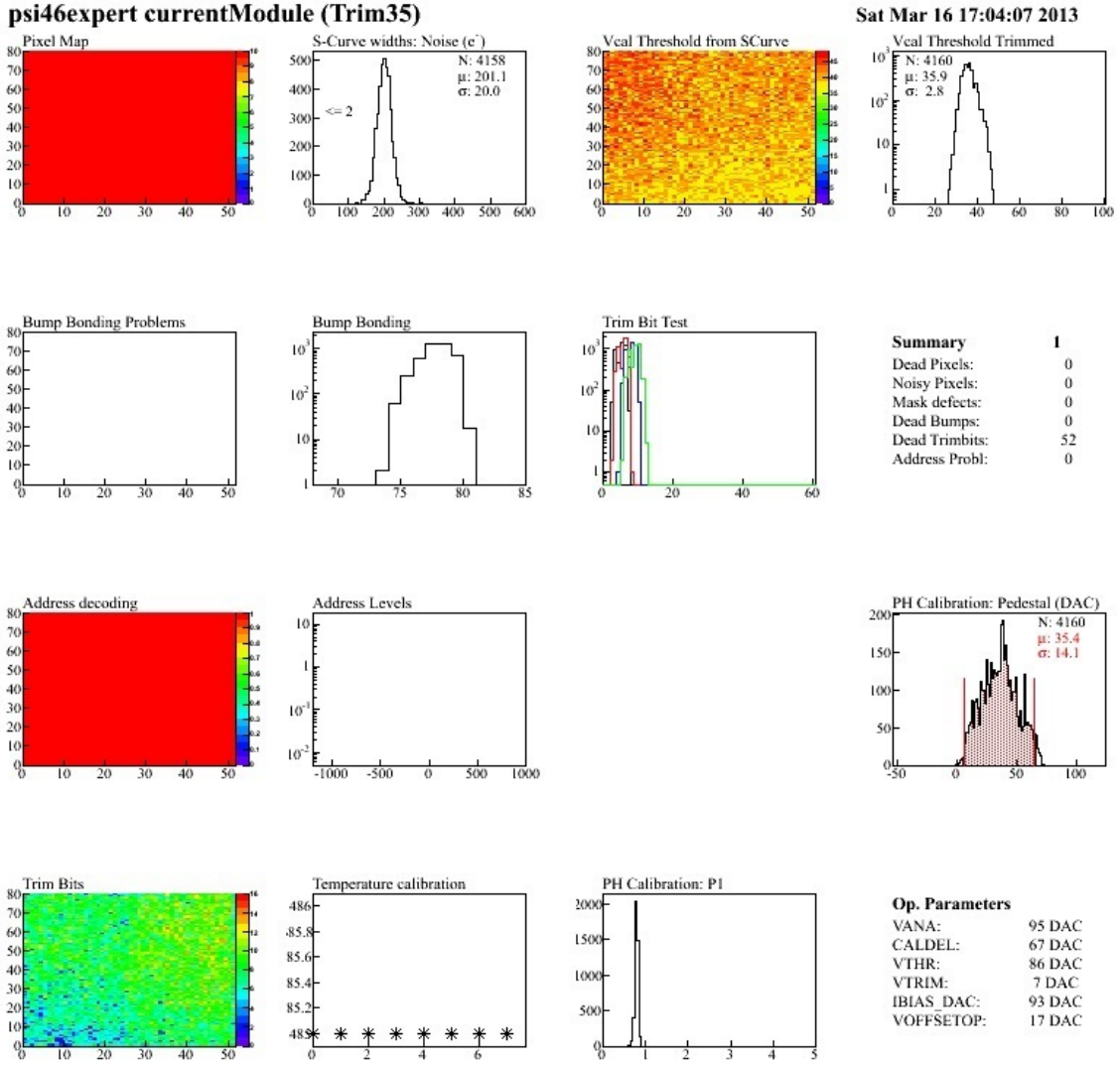

Figure 4.10: The chip summary page gives an overview of the most important plots of the electric pre-calibration.
First row, from left to right: Pixel alive map obtained with FullTest revealing no dead pixels – S-Curve width, the mean and the dispersion of the noise of the amplifier and shaper are presented – Pixel map Vcal Threshold distribution – Threshold distribution including the mean and width.
Second row: Pixel map showing bump bonding problems – Difference of the measured charge injected to the sensor and crosstalk measurement, dead bumps would yield entries around zero – Change of threshold by disabling trim bits, this test does not work flawlessly for the PSI46dig – Summary of defects.
Third row: Pixel map showing no address decoding problems – separation of analog voltage levels of the address decoding, meaningless plot for PSI46dig due to digital address decoding – Pedestal calculated with: $pedestal = p_3 + p_2 \cdot \tanh(-p_1)$ presenting the extrapolated pulse height for Vcal = 0.
Fourth row: Pixel map of the trim bit configuration – temperature calibration with an internal sensor, meaningless plot for PSI46dig as the sensor is removed – Distribution of the pulse height fit parameter p_1 – Summary of parameters.

4.7 Recorded Rate

Finally in this chapter the calculation of the recorded rate – hereafter also denoted as rate – is introduced. The introduction of this parameter is necessary to compare individual runs since the number of events is not sufficient, due to different durations and trigger rates. The recorded rate is defined as the number of detected hits normalised to the effective measuring time as well as the the sensor surface with a size of $A = 0.624\,\mathrm{cm}^2$ and is given in $\mathrm{Hz/cm}^2$ [Erd10].

$$\text{recorded rate} = \frac{\text{hits}}{\text{duration}} \cdot \frac{25\,\mathrm{ns} \cdot \mathrm{scc} + 64\,\mu\mathrm{s} - 25\,\mathrm{ns}}{25\,\mathrm{ns} \cdot \mathrm{scc}} \cdot \frac{1}{A} \tag{4.4}$$

5. Measurements and Results

The first crucial point – before starting measurements – is to know why and what shall be measured. Concerning the digital readout chip (ROC) there are two major intentions. First of all measurements give information whether there are bugs or possible improvements which can be considered in the final design of the digital readout chip. On the other side it is necessary to obtain knowledge how the ROC will behave once it is installed and running in CMS. This means that pixel detector modules respectively the ROCs have to be calibrated while the evaluation of the digital readout chip requires an estimation where uncertainties in the calibration occur and what their sizes are. In addition it is useful to compare the analog and the digital versions of the ROC at certain points. Due to the late release date of the ROCdigV2 most of the measurements are done with the ROCdigV1.

This chapter presents different options for the fitting procedure of the energy spectrum considering – as far as possible – the background. The influences of the stretched clock cycle *scc* (see section 4.2.3) and of the temperature on the peak position and on calibration curves are investigated. Further the statistical uncertainty of pre-calibrations (see section 4.5) is measured as well as the effect of different rates and timing parameters.

Each measurement is performed with a bias voltage of $V_{\text{bias}} = -150\,\text{V}$ while the generator voltage of the X-ray tube setup is $V_{\text{tube}} = 60\,\text{kV}$ by default. Moreover the standard X-ray tube current is $I_{\text{tube}} = 2\,\text{mA}$ and all data is obtained with the spectrum method (see section 4.6.1) at $20\,^{\circ}\text{C}$ as long as no other information is given.

5.1 Spectrum

The starting point of each measurement is the recorded energy spectrum which shows how much energy a particle hitting the sensor has deposited. Although the pixel detector is not intended for energy measuring, it is useful in order to achieve resolutions better than $pitch/\sqrt{12}$ the value expected from pixel geometry only [R$^+$06]. This method to improve the resolution is called charge sharing (see section 3.1.5). Therefore it is best if the detector provides a linear relation between deposited energy and detector signal. Two typical spectra of measured photons can be seen in figure 5.1. Within the K_α energy range of the available target materials the emerging photons mostly interact with the sensor via the photoelectric effect. For this reason a Gaussian distribution is expected with a mean that corresponds to the K_α energy of the target material and the goal is to measure the peak position as precisely as possible.

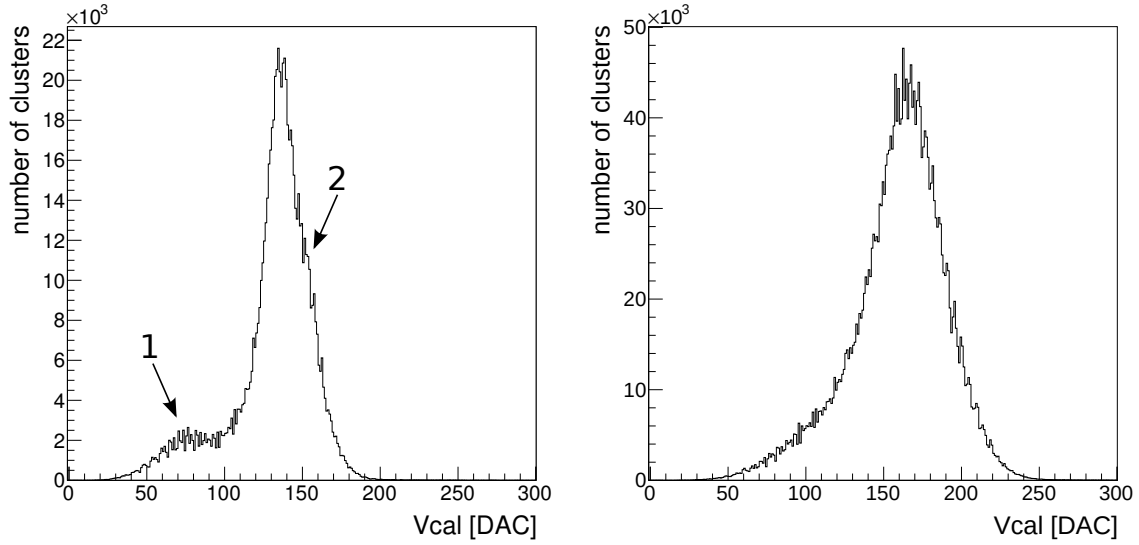

(a) tube current 2 mA (b) tube current 22 mA

Figure 5.1: Spectra obtained with the X-ray tube setup using a silver target and *scc* 250. (a) shows a spectrum measured with the default X-ray tube current 2 mA. The shoulder on the left side (1) and the one on the right side (2) are marked. In (b) a spectrum measured with a tube current of 22 mA is displayed showing an increasing width for higher tube current values.

5.2 Background

When measurements are performed it is always essential to consider the background. Of course the background should be reduced as far as it is possible and reasonable but usually it is not feasible to eliminate the background completely. Therefore it was checked how the background may influence the measurement of the spectrum. As can be seen in figure 5.1 spectra recorded with the X-ray tube setup do not only consist of a simple Gaussian, but there are two shoulders (noted as 1 and 2 in figure 5.1 (a)), one on each side of the peak. Increasing the fitting accuracy requires more information about the origin of the shoulder and whether this can be a source of uncertainty. Since the two shoulders are not expected the background spectrum is measured in order to get a possible explanation or at least an estimation of the contribution of the background on the uncertainty of the fitting process.

The background is measured in two different ways, one completely without target and one with a PVC dummy without any target material (see figure 4.6). Measuring the background with these two modifications gives the opportunity to check the influence of the PVC target support. Obviously there is a difference in the shape of the two background spectra shown in figure 5.2. As the setup with the PVC dummy is closer to the original setup it is probably the one which should be preferred. However it is interesting to investigate the effect of each background spectrum on a spectrum of a target. The background is subtracted from an energy distribution of a known target and the shape of the resulting spectrum is checked. The durations of the measurements are normalised to the same value.

Figure 5.2 shows that the spectrum corrected by the PVC dummy background has a recognisably reduced left shoulder. The correction with the background without any target is not reasonable, as there is an "over correction" leading to a negative number of events at around 55 Vcal. The peak in the background spectrum is probably pronounced because the absence of the target in the corresponding background measurement changed the shape of the background spectrum. As a consequence only the PVC dummy spectrum is usable for a background correction. However the crucial question is if there is an advantage to correct a

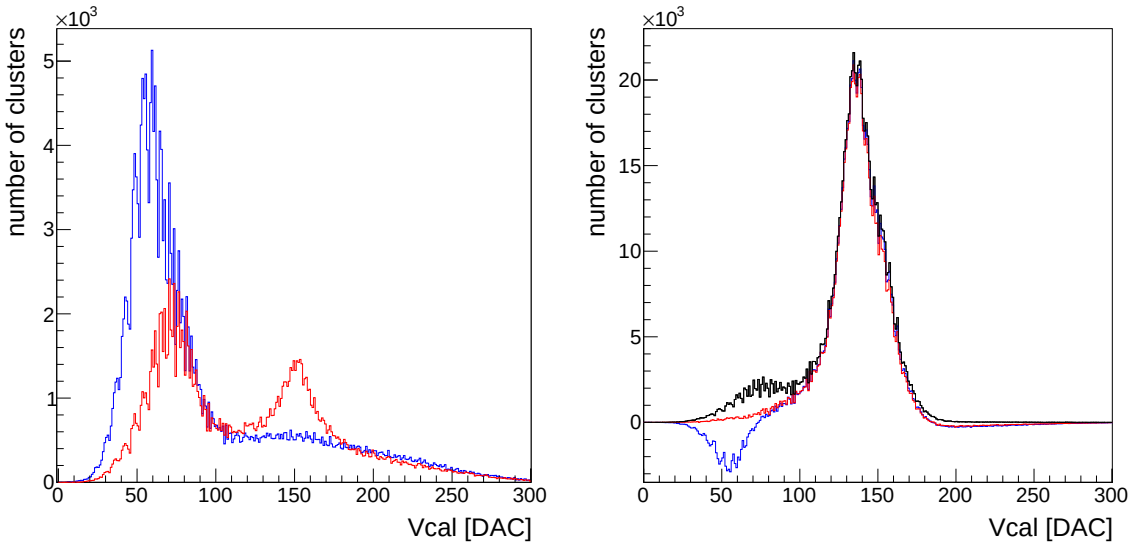

(a) background spectra (b) background subtracted spectrum

Figure 5.2: Energy distributions of background signals and of a silver target for *scc* 250. (a) The spectrum depicted by the red histogram is recorded with a PVC dummy target and the blue one is without a target on the aluminium target-holder (duration not yet normalised). (b) The black spectrum is of a silver target including the background. The red one is the silver spectrum corrected by the normalised PVC dummy background and the blue spectrum is corrected by the normalised background without any target. Only the correction with the PVC dummy background reduces at least one shoulder reasonably.

recorded spectrum with the corresponding normalised PVC dummy background. The goal is to reduce the uncertainty in the calculation of the peak position which is discussed in the next section 5.3.

Measuring the background of the setup with the X-ray source is not possible, because the ^{241}Am source and its target materials cannot be separated (see section 4.3.2). Anyway this would not be reasonable since removing the target material would require a major change in the setup which would change the shape of the background, too.

5.3 Fitting the Spectrum

It is not possible to use the mean of the distribution for the peak position since a recorded spectrum does not only consist of a single Gaussian. There are several options to calculate the peak position, decisive for each option is the size of uncertainty on the peak position and how feasible they are. The latter has to be taken in account because calculation of the peak positions has to be done for every measurement and should be easily reproducible for multiple measurements.

5.3.1 One Gaussian

A single Gaussian is the most simple option to calculate the peak position, but this calculation may include avoidable uncertainties depending on the chosen fitting interval. This effect is visible in figure 5.3 and occurs as soon as the interval includes a part of a shoulder shifting the peak position by about 2 Vcal units. Subtracting the background does not help, since there is only a reduction of the shoulder on the left side of the peak as can be seen in figure 5.2. However this uncertainty of around 2 Vcal units on the peak position can be avoided easily

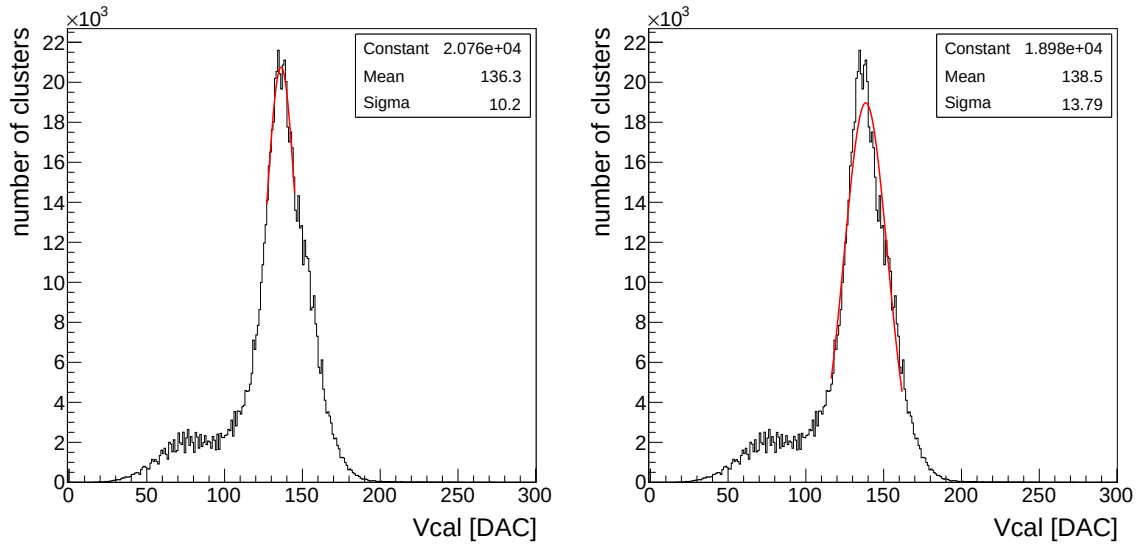

(a) good choice of limits (b) poor choice of limits

Figure 5.3: Fitting range dependence of the peak position. The target material is silver, with *scc* 250 in the X-ray tube setup and the default tube current. In (a) the range of the Gaussian fit is restricted to the Gaussian-shaped part. The fitting range in (b) partially includes one shoulder resulting in a visible mismatch of the fit mean and the recorded peak.

by setting the fitting interval carefully. In this case the remaining uncertainty is smaller than 0.2 Vcal.

5.3.2 Three Gaussians

Although the one-Gaussian fit is reliable with carefully chosen limits the fitting may be improved with a procedure that uses the whole range of a spectrum. Assuming that a spectrum recorded with the X-ray tube consists of one Gaussian for each shoulder and one for the K_α peak a three-Gaussian fit may be appropriate. Furthermore this is an opportunity to check whether one of the shoulders originate from the K_β energy of the target or from backscattered photons. Such a fit with three Gaussians is shown in figure 5.4. Whether the intention to describe the whole spectrum works can easily be checked by looking at the sum of the three Gaussians. Figure 5.4 shows that the sum suits the whole spectrum indicating that three Gaussians are sufficient.

In figure 5.4 a silver spectrum and a molybdenum spectrum are plotted. First it is tested whether the red spectra belong to the K_α energy of a target and the blue ones to the K_β energy. For silver the difference between K_α and K_β is 2779.50 eV and for molybdenum 2128.97 eV [NIS13]. These values can be converted in Vcal units for the next analysis steps. In silicon – the sensor material – 3.6 eV are necessary to create one electron-hole pair. As will be shown in section 5.4 an Vcal unit corresponds to 50 electrons. Hence the difference of K_α and K_β for silver is 15 Vcal and for molybdenum 12 Vcal. The actual distances, 7 Vcal for silver and 9 Vcal for molybdenum (see figure 5.4), are too small. Furthermore the K_α to K_β distance of silver has to be greater than for molybdenum. It is also expected that there are more K_α than K_β events which is not the case for the silver spectrum. The latter is also the reason why the green spectra cannot correspond to K_α when the red or blue ones correspond to K_β.

Another consideration is that photons passing the detector undergo Compton scattering and then hit the detector. In this case a K_α peak and a Compton peak with a distance of 9 Vcal

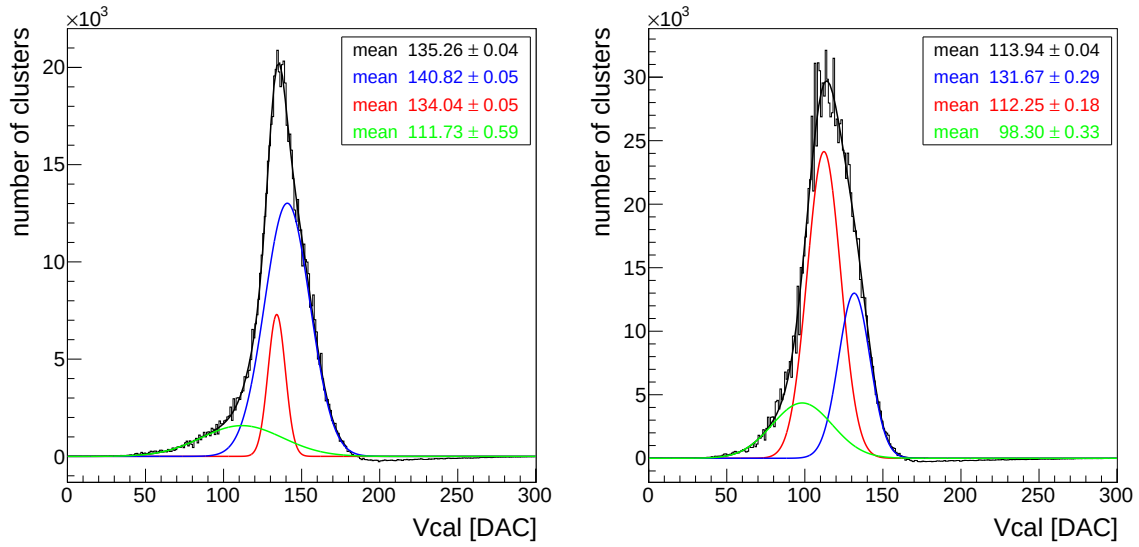

(a) silver spectrum (b) molybdenum spectrum

Figure 5.4: Three Gaussian fit for two spectra measured at *scc* 250 and corrected by the PVC dummy background. The mean – including its error – of each curve is calculated. It is visible that a three Gaussian fit is sufficient since the sum of the three Gaussians fit the entire spectra. (a) is obtained with a silver target and (b) with a molybdenum target. The blue, red and green curves are the three single Gaussians while the black one is the sum of the three.

are expected for silver (for the calculation of the Compton peak see section 3.1.4). However there is no such distance regarding the red, blue and green spectra (see figure 5.4 (a)). Finally three Gaussians fit the spectrum well, but there is no clear assignment of the single Gaussians possible.

5.3.3 Sum of three Gaussians

In the previous section 5.3.2 the assignment-problem of the application of three single Gaussians is described. However the sum of the three Gaussians, which is plotted in black in figure 5.4, is a promising candidate. In contrast to the one-Gaussian the sum uses the whole spectrum. Because of that there is no risk of an avoidable uncertainty due to unfavourable limits like mentioned in section 5.3.1. Besides eliminating the mentioned uncertainty a further improvement is not possible and as figure 5.5 shows a one-Gaussian fit provides similar results by choosing correct limits. On the other hand the application of three Gaussians comes with additional effort. For instance an adaptation of the initial values of the fitting parameters is required for most of the spectra. Since the correct limits of a single Gaussian can be adjusted easily and the use of the sum needs considerably more effort the more efficient method is a one-Gaussian fit with carefully chosen limits. From now on only single Gaussians are used for the fitting procedure.

5.4 scc Dependence

Measuring in a laboratory especially with X-ray sources with reasonably low activity like the already mentioned ^{241}Am source results in small data samples. A very efficient tool to obtain better statistics is the so called stretched clock cycle (*scc*) which is already explained in section 4.2.3. In this section the Vcal value is measured for different *scc* values between 1 and 1000. As the *scc* merely stretches a clock cycle and the deposited charge is unchanged because of the stable K_α energy no change in the Vcal value is expected. In figure 5.6 the

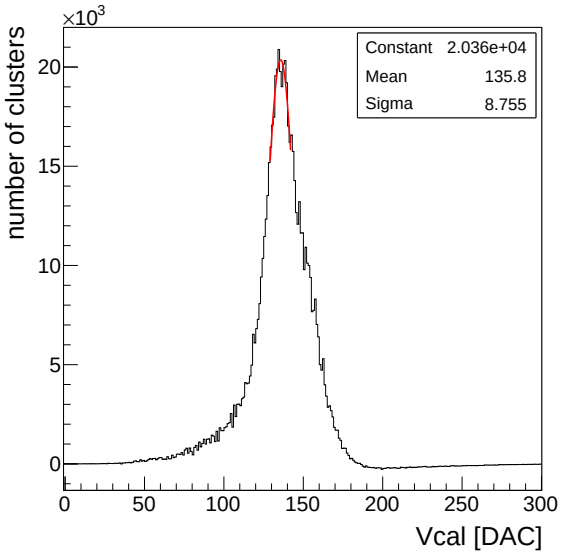

Figure 5.5: This figure shows – in principle – the same spectrum as figure 5.3, however this time it is corrected by the PVC dummy background. A one Gaussian fit with carefully chosen limits provides similar results as the sum of the three Gaussians in figure 5.4 (a) which gave a mean of 135.3 Vcal.

scc dependence of the peak position for the analog ROC and the ROCdigV1 are plotted. In contrast to the expectation the Vcal value is not constant for different *scc* values. The ROCdigV1 and the analog ROC show a steep Vcal increase for *scc* values up to around 200. Afterwards the slope of the ROCdigV1 is marked by a slight increase while the analog ROC has a plateau followed by a slight drop for *scc* values greater than 700. The total Vcal increase of the ROCdigV1 is more than 45 Vcal.

Since the *scc* simply stops the clock and hence extends the active timeframe it is incomprehensible that the Vcal value depends on the *scc*. Therefore it is crucial for all measurements that pulse heights are only comparable if they were obtained with the same *scc*. The question comes up whether the *scc* has an influence on the slope or the linearity of the calibration curve. As it is already described in section 4.5.4 a linear relation between particle energy and detector signal is desired. To test for an *scc* dependence several calibration curves were measured for different *scc* values. The results are plotted in figure 5.7. As expected due to the visible *scc* dependence in figure 5.6 the measured points are shifted to higher Vcal values for increasing *scc* values. Nevertheless the slopes of the calibration curves are independent of the *scc* at around 50 e/DAC, while the linearity gets worse for higher *scc* values. During operation in the CMS experiment the *scc* dependence is of no relevance because *scc* will not be used once the pixel detector is installed in the CMS detector. However it is of relevance for testing in the laboratory. Using a fixed *scc* between 100 and 250 should be preferred as this ensures both enough statistics and sufficient linearity of the calibration curve.

5.5 Temperature Dependence

Of particular interest is the investigation of a temperature dependence of the peak position and the calibration curves. It is planned that the temperature of the pixel sensors will be −20 °C after the Phase I Upgrade. The current analog ROC shows a clear temperature dependence already observed in [Hos12] and visible in figure 5.8. In the left graph several calibration curves for different temperatures are plotted which have obviously different slopes. The plot on the right-hand side shows the temperature dependence of the slope. Aside from

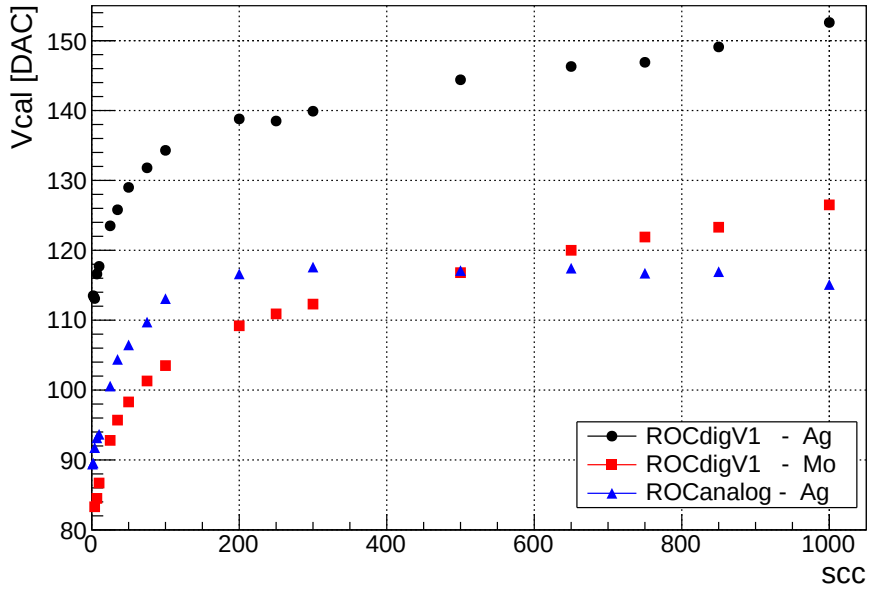

Figure 5.6: *scc* dependence of the Vcal peak position. The dependence was already obtained for the analog ROC [Hos12, p. 70] and is now also measured for the ROCdigV1 in the X-ray tube setup at the default tube current. Applying a silver and a molybdenum target delivers the same behaviour with the ROCdigV1. The analog ROC and the ROCdigV1 have a strong Vcal increase for *scc* values up to 200. Then the signal of the analog shows a plateau followed by a slight drop while the ROCdigV1 shows a moderate increase.

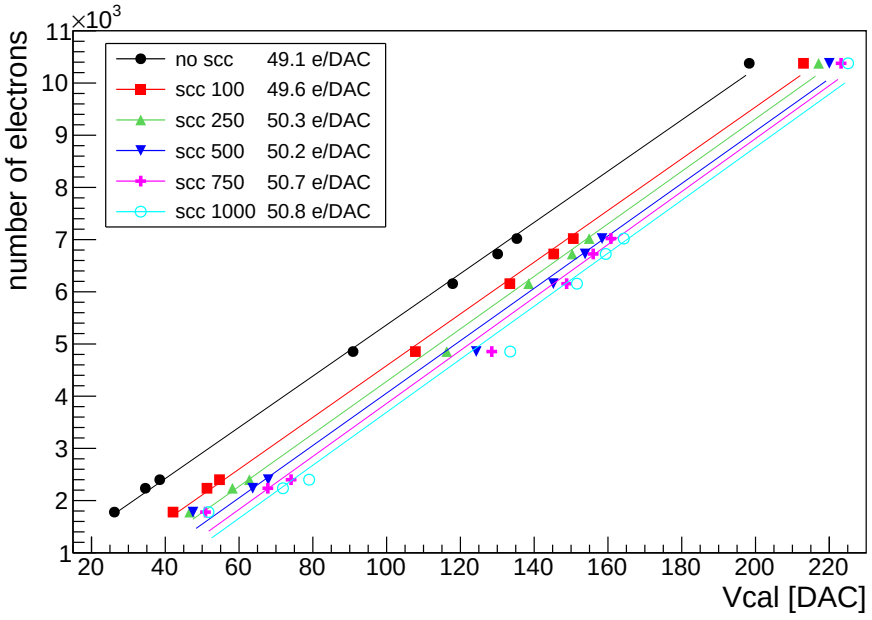

Figure 5.7: The plot shows one calibration curve without *scc* and several calibration curves with different *scc* values measured in the X-ray tube setup. All calibration curves have similar slopes of around 50 e/DAC. There is a visible shift to higher Vcal values for increasing *scc* values. The linearity of the calibration is getting worse for high *scc* values.

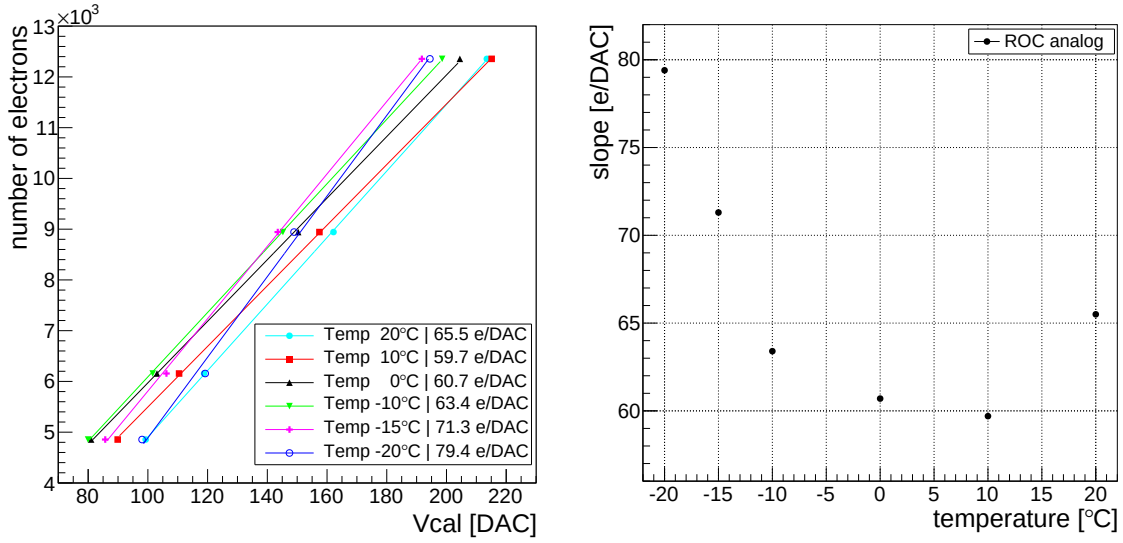

(a) calibration curves (b) calibration slopes

Figure 5.8: Temperature dependence of the analog ROC [Hos12, p. 79/80]. All temperatures are measured on the sensor surface. (a) shows several calibration curves for different temperatures. There is a distinct temperature dependence of the slopes visible. (b) shows the obtained slopes in detail, a spread from about 60 e/DAC to 80 e/DAC is observed with increasing slopes for decreasing temperatures and a possible minimum at 10 °C.

the first value of 65 e/DAC at 20 °C there is a distinct increase of the slopes, starting at around 60 e/DAC for 10 °C up to roughly 76 e/DAC at −20 °C.

As this may also occur for the ROCdigV1 and therefore influences the results during operation additional tests are necessary. However the changes in the design of the ROCdigV1 may result in a temperature independence of the calibration curves respectively the slopes.

5.5.1 Calibrations at Different Temperatures

To test the ROCdigV1 for a temperature dependence, calibration curves at several temperatures – which are the same as the ones of the analog ROC – are measured. All measurements are done in the setup with the ^{241}Am source and with an *scc* of 1000. Figure 5.9 shows that the temperature dependence of the analog ROC is not observed in measurements with the ROCdigV1 anymore. The slopes have the same values of approximately 50 e/DAC as the measurements in section 5.4. Further there is a minor offset of the calibration curves without any trend. The standard deviation of the silver measurements of the calibration curves is 2.3 Vcal and the standard deviation of the slopes is 0.4 e/DAC.

Another important point for the analog ROC is the DAC Vsf. This DAC influences the signal between shaper and sample-and-hold capacitance for manipulating the linear range of the pulse height of a pixel. In case of the analog ROC an optimisation of the DAC Vsf is necessary, otherwise the calibration curves of the analog ROC do not show a linear relation. For each temperature a different Vsf value is required, however this results in different slopes (see figure 5.8) of the calibration curves for different temperatures since the Vsf manipulates the signal in each pixel-unit-cell (PUC). The digital versions of ROCs do not require an Vsf optimisation when the temperature changes but as depicted in figure 5.10 Vsf still influences the slopes. Compared to previous results the slopes are not around 50 e/DAC but less. This could be a result of using the new ROCdigV2 or of measuring the calibration curves with only four targets.

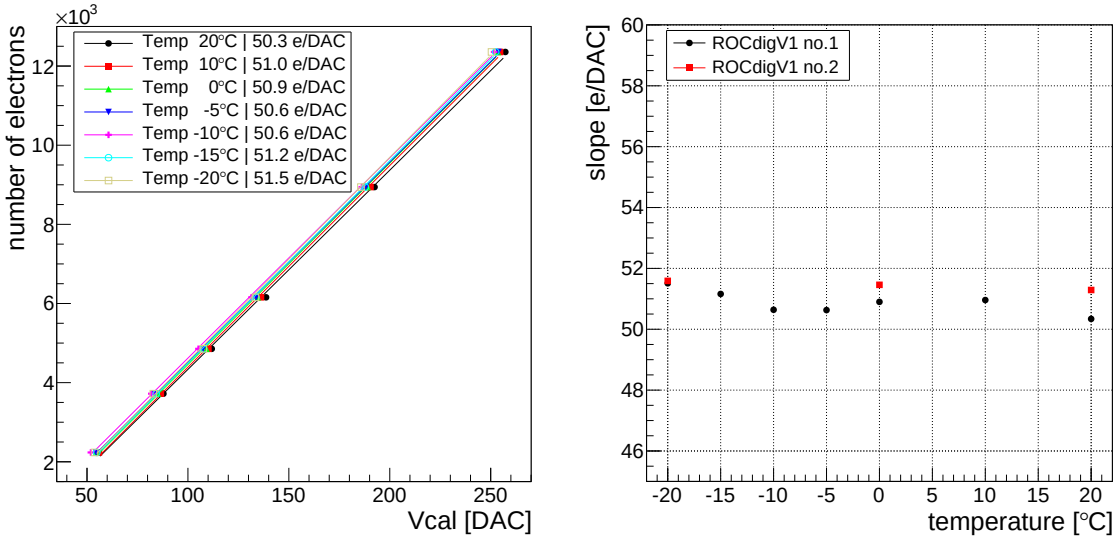

(a) calibration curves (b) calibration slopes

Figure 5.9: Temperature dependence measurements of the ROCdigV1 performed in the setup with the ^{241}Am source. All temperatures are measured on the sensor surface. (a) shows several calibration curves for different temperatures with no visible temperature dependence. There is a small shift of the calibration curves without a trend. (b) illustrates in detail the temperature independence with slopes of around 50 e/DAC and a standard deviation of 0.4 e/DAC for two different ROCs.

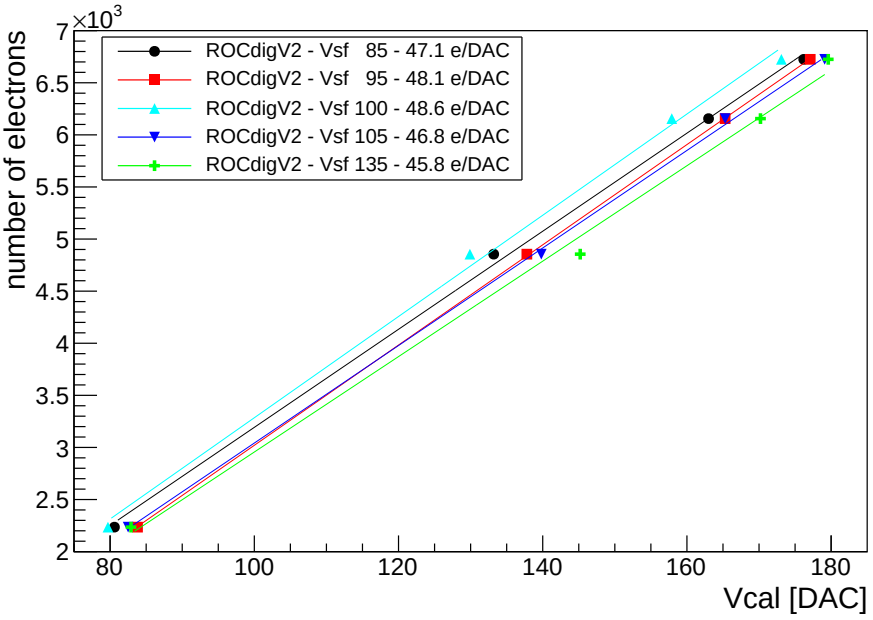

Figure 5.10: Several calibration curves are measured for different Vsf values with the ROCdigV2 and the targets silver, molybdenum, indium and copper in the X-ray tube setup. A shift of the calibration curves is visible as well as an influence on the slope but there is no trend recognisable.

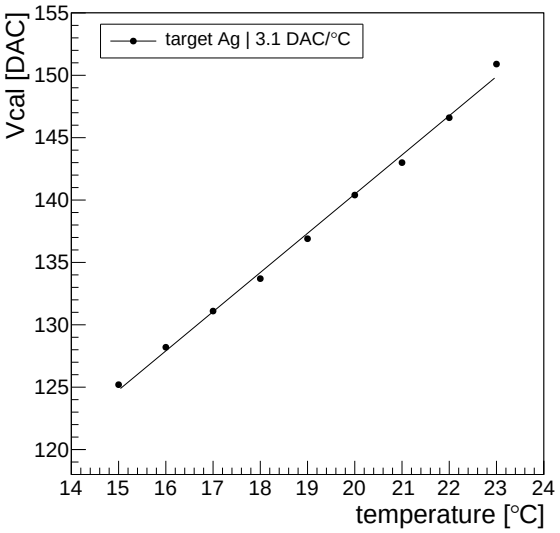

Figure 5.11: Investigation of the influence when the measuring temperature differs from the temperature during the pre-calibration. The measurements are performed with a silver target in the setup with the ^{241}Am source. The temperature of the applied pre-calibration is 20 °C while the pulse heights are measured for temperatures from 15 °C to 23 °C with a step size of 1 °C. A linear relation between temperature and Vcal is observed with a slope of 3.1 DAC/°C.

5.5.2 Temperature Uncertainties

The missing trend of the shift in figure 5.9 implies that there is no systematic temperature dependence of the ROC but it may be an uncertainty of the temperature measurement itself. Hence it is necessary to measure what happens with the pulse height if the temperature during data taking differs from the temperature of pre-calibration. A possible testing procedure is to do a pre-calibration at a certain temperature and take data at several different temperatures using this particular pre-calibration. This is done in figure 5.11. The pre-calibration temperature is 20 °C whereas data taking is performed at varying temperatures changing in steps of 1 °C, resulting in a linear relation with a slope of 3.1 DAC/°C. As the accuracy of the *Pt1000* Class A sensors [DIN08] is at least ±0.19 °C the setup should reproduce slopes to about 0.6 DAC. Therefore the slope of 3.1 DAC/°C alone cannot explain the previously mentioned standard deviation of 2.3 Vcal units (see section 5.5.1).

5.6 Error on Pre-Calibrations

Trying to explain the shift of the calibration curves mentioned in section 5.5.1 simply by the uncertainty of the temperature measurement is not sufficient. An additional source of uncertainty could be different pre-calibrations. Each calibration line in section 5.5.1 requires its own pre-calibration to have for instance a correct – temperature related – pulse height calibration. Since the pre-calibration consists of certain routines which vary the DAC values stepwise, differences between pre-calibrations are possible, even if all conditions are the same. The uncertainty related to the pre-calibrations can be determined by creating several pre-calibrations under the same conditions and comparing measured pulse heights. In this case six pre-calibrations at 20 °C are done over the course of one month. For each pre-calibration the pulse height of a silver target is measured, which is shown in figure 5.12 (a).

Obviously there is an uncertainty. The Vcal values of the pulse heights are spread over a range of 3.2 Vcal and have a standard deviation of 1.2 Vcal. This is not a major uncertainty, but

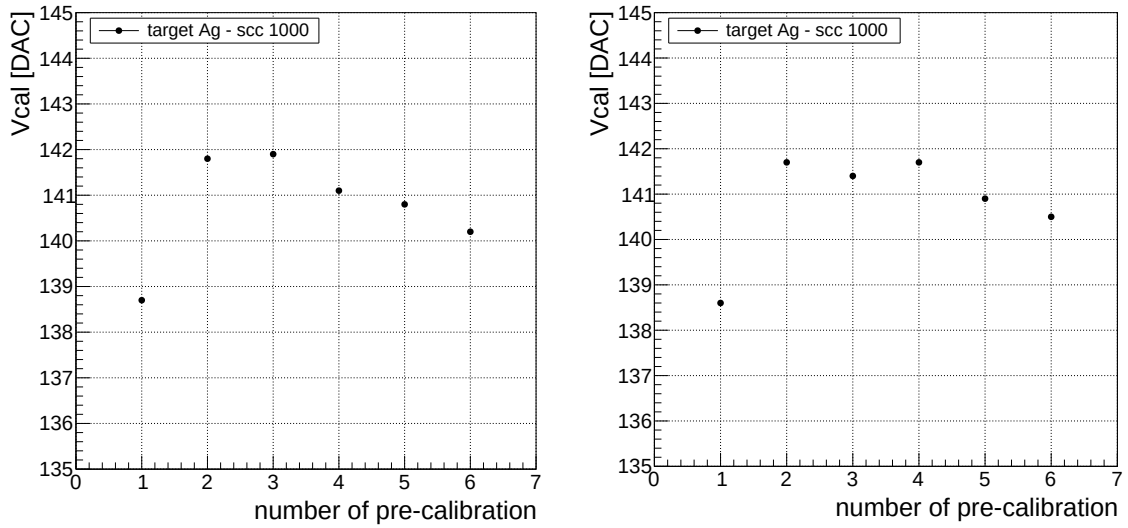

(a) (b)

Figure 5.12: Uncertainty of pre-calibrations using six pre-calibrations under identical conditions. (a) For each pre-calibration the pulse height of silver is measured and displayed. The results show a minor uncertainty with a standard deviation of 1.2 Vcal on the pulse height. In (b) one measurement is analysed with the pulse height calibration files of the different pre-calibrations resulting in a comparable distribution of Vcal values.

several small uncertainties – like the uncertainty discussed here and the one from section 5.5.2 – may explain observations like the shift of calibration curves in figure 5.9.

It is of interest whether the differences occur because of different DAC settings or if they are only based on different pulse height calibrations. If differences in the pulse height appear only due to the pulse height calibrations is simply verifiable by analysing one of the measurements with the pulse height calibration files of the different pre-calibrations. Indeed figure 5.12 (b) provides a very similar distribution as figure 5.12 (a). Hence this uncertainty is related to the pulse height calibrations and effectively independent of the DACs adjusted differently. As long as all conditions are identical it is advisable to use one certain pulse height calibration for each measurement regardless of the pre-calibration. Using one pulse height calibration for several pre-calibrations reduces the observed (figure 5.12) uncertainty, but it has to be ensured that all conditions – during pre-calibration and measurement – are equivalent. Nevertheless the uncertainty due to different pulse height calibrations only results in a minor shift of the calibration curves and does not influence the slopes.

5.7 Rate Dependence

An additional interesting topic stems from the observed rate dependence of the pulse height of the analog ROC [Hos12, p. 59-69]. The observed behaviour of the analog ROC can be seen in figure 5.13. These results of the analog ROC serve as starting point and reference for measurements with the ROCdigV1. The definition of the rate is explained previously in section 4.7. There are two ways of manipulating the rate for the investigation of the rate dependence of the ROCdigV1 which are described in this section. All measurements are performed in the X-ray tube setup.

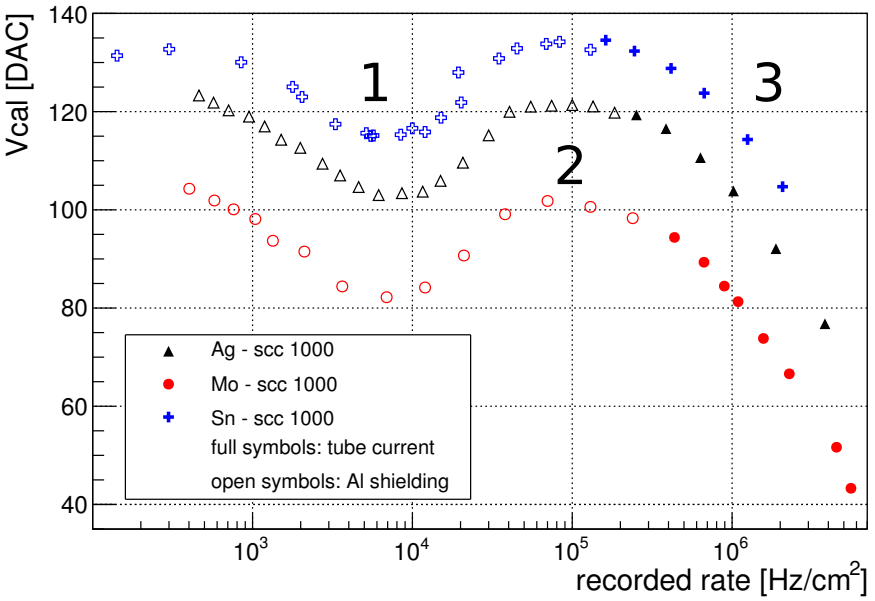

Figure 5.13: Rate dependence of the analog ROC. The pulse height – given in Vcal units – is measured as a function of the rate for different targets [Hos12, p. 63]. There is an obvious signal dip (1) at a rate of 7-8 kHz/cm^2 which is independent of the target material. The dip is followed by a plateau (2) which in turn is followed by a drop (3) above 100 kHz/cm^2.

5.7.1 Tube Current

First the manipulation by changing the current of the X-ray tube in the available range from 2 mA to 33 mA is discussed. In the measuring program the tube current is varied and the rate for each step is measured. Since the only parameter is the tube current a linear relation between rate and tube current is expected. The results in figure 5.14 confirm the expected linear relation between tube current and rate and are independent of the *scc*. This is reasonable as changing the *scc* only changes the duration of the active timeframe and does not affect the particle flux generated by the X-ray tube.

Manipulating the rate by changing the tube current within the available range delivers a rate range from about 0.5 MHz/cm^2 to almost 7 MHz/cm^2. To increase the rate to even higher values an additional modification like dismantling the collimator of the X-ray tube would be necessary.

5.7.2 Shielding

The second option to manipulate the rate is to apply a shielding. According to the Lambert-Beer law (see e.g. [Dem07])

$$P(x) = \exp\left(-\frac{l}{x}\right) \tag{5.1}$$

an exponential drop of the rate is expected. P is the probability that a photon is absorbed, l is the absorber and energy dependent attenuation length and x is the thickness of the absorber. The shielding in the X-ray tube setup is mounted in the secondary beam, between the target and the single chip sensor visible in figure 4.5. Several layers made of aluminium are used for the shielding. They have the advantage that the K_α energy of aluminium is below the adjusted threshold of the ROCdigV1 of 35 Vcal units. Additionally the available set of layers

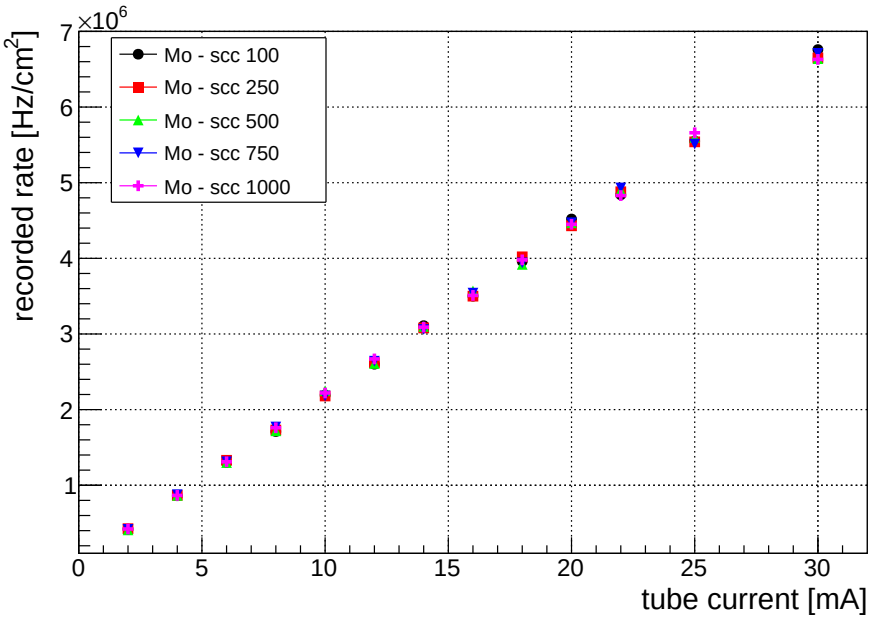

Figure 5.14: Rate manipulation by changing the X-ray tube current. Observable is a linear relation between rate and tube current. The usage of tube currents from 2 mA to 30 mA results in rates from 0.5 MHz/cm^2 to almost 7 MHz/cm^2 with no *scc* dependence.

with thicknesses between 0.5 mm and 11.5 mm in steps of 0.5 mm provides various rates. In principle the application of aluminium layers is also suitable for the setup with the ^{241}Am source. However even with high *scc* values the obtained data samples are small. So it is barely possible to perform reasonable measurements with a shielding in the setup with the available ^{241}Am source.

Modifying the tube current delivers a rate range of 0.5 MHz/cm^2 to almost 7 MHz/cm^2. The lowest rate of 0.5 MHz/cm^2 was achieved with a X-ray tube current of 2 mA. Hence mounting an additional shielding should reduce the rate and increase the available range. Nevertheless it is not avoidable that the statistics suffer with increasing shielding, even in the X-ray tube setup. To improve statistics at low rates several measurements with the same shielding are combined. Figure 5.15 shows the expected exponential drop of the rate for increasing shielding thickness. A further decrease of the rate is not advisable, as it is not possible to generate sufficient statistics within an appropriate time even by combining several measurements. Using shielding extends the available range of the rates down to several hundred Hz/cm^2. In figure 5.15 the influence of low statistics associated with a large shielding is recognisable which increase the uncertainty significantly.

5.7.3 Rate dependence over entire accessible range

The pulse height for the entire accessible rate range is measured using both methods of rate manipulation. For further investigation it is favourable to divide the recorded pulse heights in several regions. There is a region with a strong signal increase at rates above 100 kHz/cm^2, a signal dip at rates around 10-20 kHz/cm^2 and a possible drop of the signal at low rates (see figure 5.16). Concerning the drop at low rates it is not possible to make a distinct statement so far due to the rate limits of the silver measurements. The *scc* does not seem to influence the shape except the absolute pulse height which is expected after the results presented in section 5.4. There is no plateau region like it exists in case of the analog ROC (see figure 5.13).

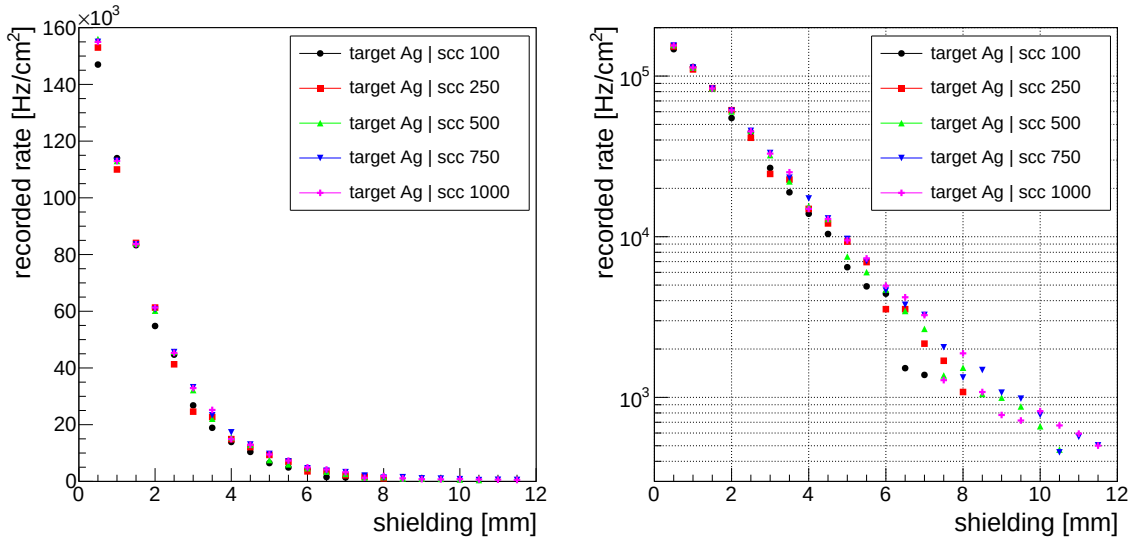

(a) exponential shape (b) logarithmic presentation

Figure 5.15: Rate manipulation by mounting a shielding of aluminium layers using a silver target. In both plots the extension of the already available rates (0.5 MHz/cm^2 - 7 MHz/cm^2) down to some hundred Hz/cm^2 is visible. (a) displays the expected exponential shape while (b) shows the same measurement with the rate (y-axis) plotted logarithmically. It is visible that the measurements suffer from low statistics especially with large shieldings and small *scc* values.

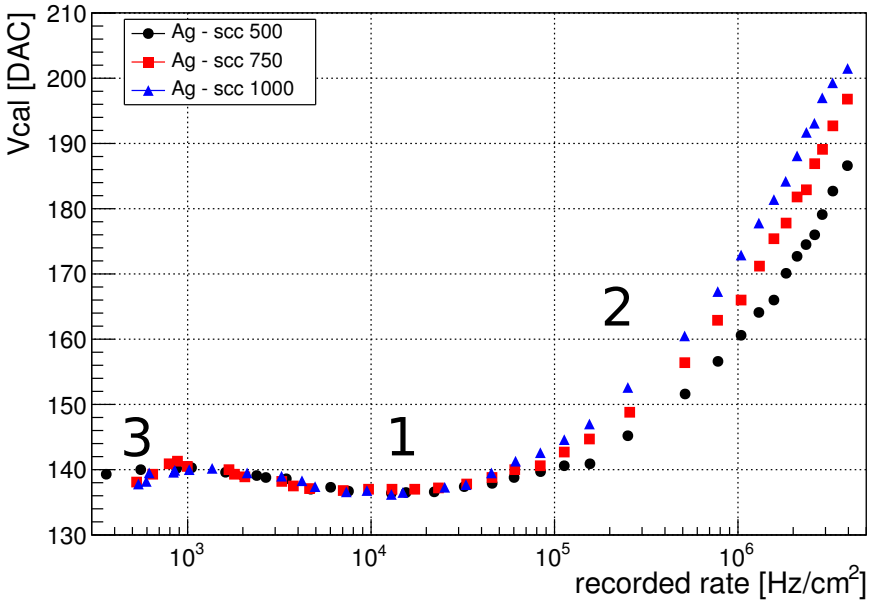

Figure 5.16: Rate dependence of the pulse height over the entire accessible range of rate, measured using a silver target. In contrast to the analog ROC (figure 5.13) there exists no plateau region in the ROCdigV1. Instead there is a signal dip (1) at around 10-20 kHz/cm^2, a strong increase (2) of the measured pulse height for rates larger than 100 kHz/cm^2 and a possible drop (3) at low rates. The *scc* only has an influence on the absolute pulse height (which is expected due to the results from section 5.4).

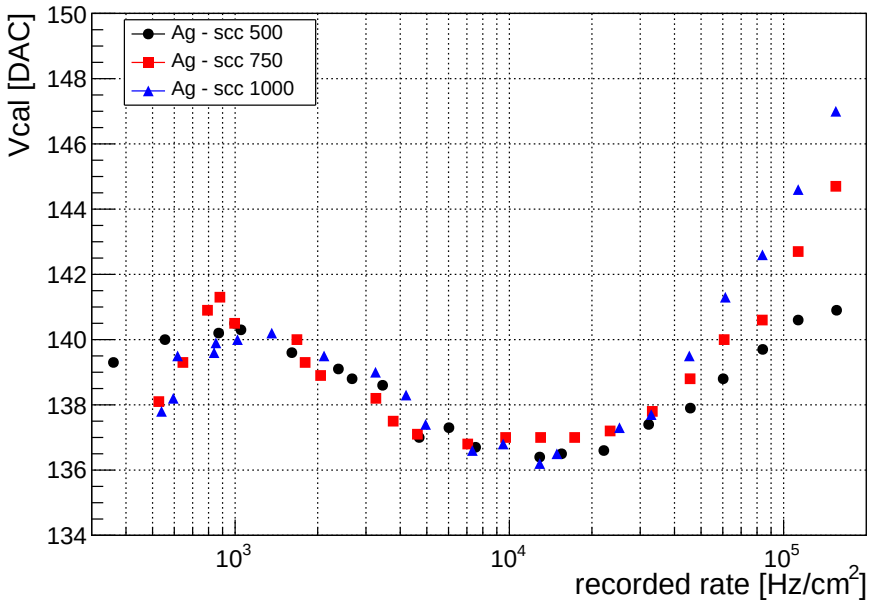

Figure 5.17: Zoomed version of figure 5.16. The signal dip of the ROCdigV1 occurs at rates of about 10-20 kHz/cm^2 and is independent of the chosen *scc* value.

5.7.4 Signal Dip

First the region of the signal dip which already occurred in case of the analog ROC is investigated (see figure 5.13). The position of the signal dip of the ROCdigV1 is at slighty higher rates at around 10-20 kHz/cm^2 and independent of the *scc*.

The reason for the signal dip is the storage capacitor of the sample-and-hold circuit which can be seen in figure 3.12. The signal which is stored in this capacitor is written by the analog voltage domain, but it is read from the digital voltage domain. While the analog current and therefore the analog voltage plus the stored signal is almost constant the digital current changes in the range of the signal dip (see figure 5.18). The readout of the mentioned storage capacitance is done by a single-ended amplifier and is supplied by the digital voltage. As the digital voltage is rate dependent the supply voltage of the amplifier decreases and hence the signal decreases, too. The mentioned variation of the supply voltage of the amplifier and its influence on the output voltage is known as *power supply rejection ratio* [Man02]. In order to minimise this effect the amplifier of the digital ROC is modified, so that the amplifier uses the same powering as the sample and hold circuit. This does not eliminate the signal dip entirely but as it is shown in figure 5.19 the effect is less distinct for the ROCdigV1 [Käs13].

To verify if the signal dip also occurs for different targets and if the position of the dip stays at 10-20 kHz/cm^2 an additional measurement with a molybdenum target is done. Since the position of the signal dip does not change for different *scc* values only one *scc* for comparison is used. Figure 5.19 shows that the position of the signal dip is not only *scc* independent but also independent from target material. Additionally the signal dip measured with an analog ROC is plotted. Obviously the signal dip of the analog ROC is remarkable more pronounced and – as previously mentioned – at lower rates of about 7-8 kHz/cm^2.

Because of the rate dependence of the pulse height it would be preferable to measure all targets of a certain calibration line at the same rate. Unfortunately the targets provide different rates for identical settings. The alternative to adjust the rate for each target by changing the X-ray tube current or applying a shielding is not favourable. Reaching similar pulse heights a plateau region where the pulse height is constant would be helpful. In case of

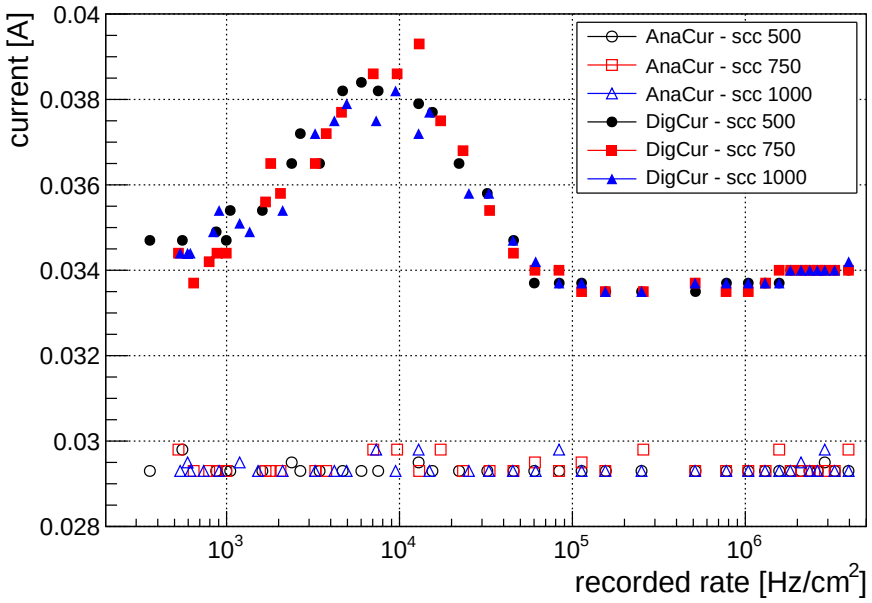

Figure 5.18: Analog and digital current as a function of the rate for several *scc* values. The analog current is constant over the entire range, while the digital current increases at the position of the signal dip.

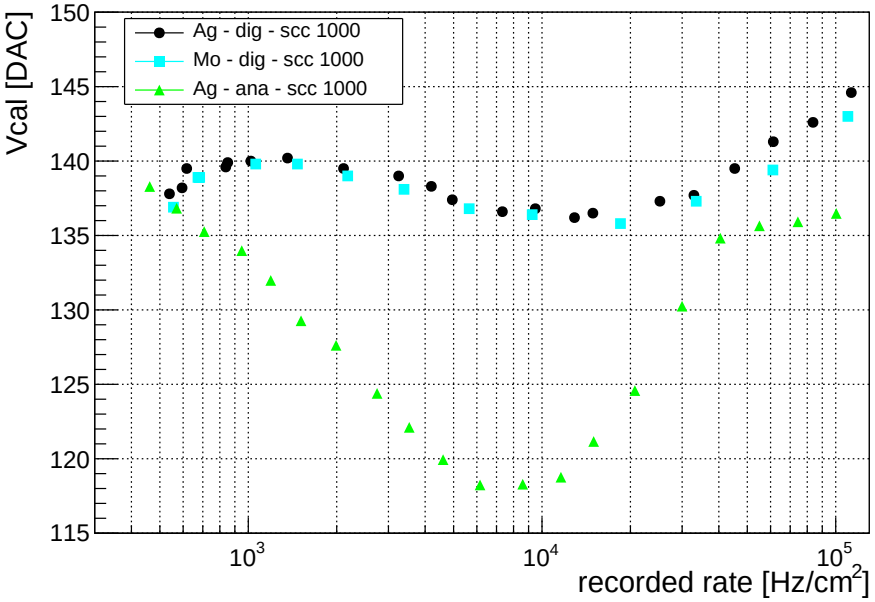

Figure 5.19: Position of the signal dip of the ROCdigV1 (marked as *dig*) at rates of about 10-20 kHz/cm^2 for silver and molybdenum targets. Independent of the *scc* value the signal dip occurs at the same rate. For comparison a measurement with the analog ROC (marked as *ana*) is plotted in green. The signal dip of the analog ROC is at lower rates and much more pronounced.

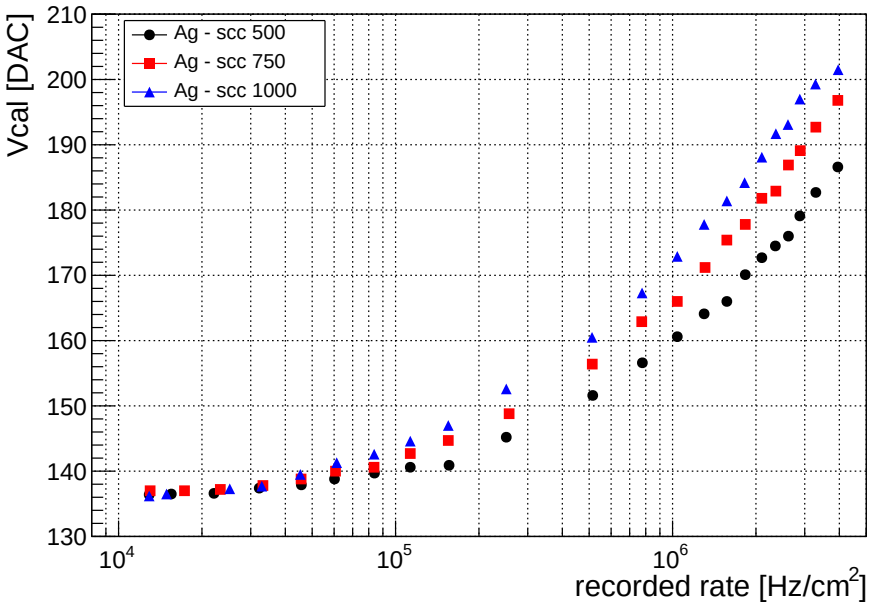

Figure 5.20: Pulse heights of the ROCdigV1 measured for high rates using an Ag target and different *scc* values. In contrast to the analog ROC there exists no plateau region in the ROCdigV1. Instead there is a strong increase of the measured pulse height for rates larger than 100 kHz/cm^2.

the analog ROC there is such a plateau region between the signal dip and the drop at high rates.

5.7.5 Rise at High Rates

Contrary to the analog ROC there is apparently no plateau for rates above the signal dip for the ROCdigV1 (see figure 5.20). Actually the pulse height increases strongly for rates greater than 100 kHz/cm^2. Compared to the observed pulse height drop of the analog ROC the behaviour of the ROCdigV1 at high rates is entirely changed. In order to get a possible explanation the analog and digital current of the ROCdigV1 are examined. Any rate dependence of one of the currents at high rates may give an indication of what the source of the strong increase is or at least isolate the increase to a certain part of the ROC. In figure 5.18 the analog and the digital current have already been presented as a function of the rate. Although the digital current shows a rate dependence it is constant at rates above 100 kHz/cm^2 while the analog current has no rate dependence at all so the currents are not able to explain the rise of the pulse height at high rates.

Nevertheless there is still an opportunity to investigate the rate dependence further. The rate dependence measurements of the ROCdigV1 are performed with the spectrum method while in section 4.6 another method is described: the threshold method which does not use the whole chain of the *PUC* (see figure 3.12). Using the threshold method tests simply whether a signal exceeds the comparator threshold or not. If the rise of the pulse height is caused by a component behind the comparator the threshold method does not show any rate dependence.

Figure 5.21 displays the measurements performed with the threshold method revealing no rate dependence and giving a comparison with the spectrum method. Hence the rise of the pulse height at rates above 100 kHz/cm^2 may be located somewhere in the sample-and-hold circuit, especially because the information about the pulse height is stored in the sample-and-hold capacitance. Furthermore it is known that there is a change in the powering of the readout amplifier of the sample-and-hold storage capacitance (see section 5.7.4). However a rate

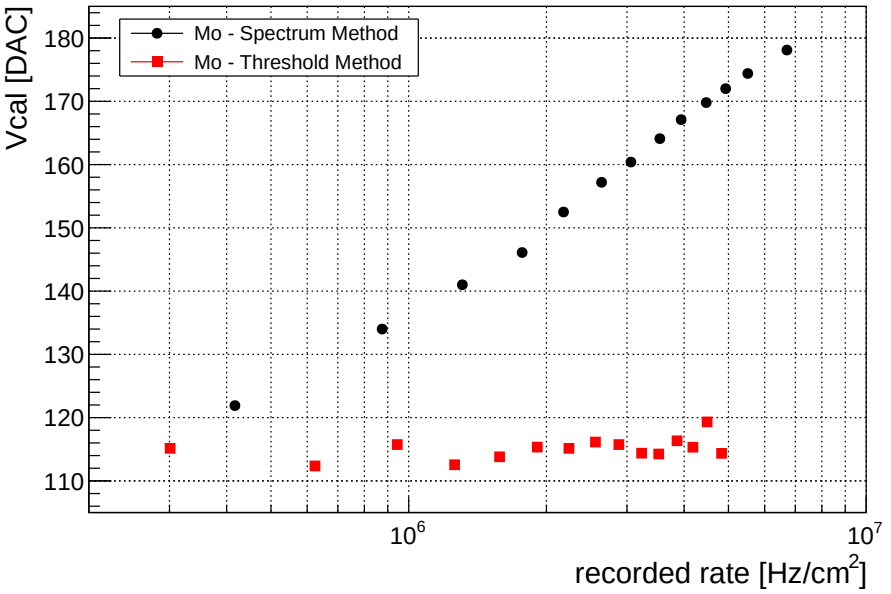

Figure 5.21: Comparison of the rate dependence of the pulse height using both data acquisition methods with a molybdenum target and an *scc* of 250. While the spectrum method shows a rise of the pulse height there is no significant dependence in the measurement with the threshold method.

dependence of the analog or the digital current would be expected if the sample and hold circuit is the reason. Therefore it is only possible to exclude the parts of the *PUC* which are used by the threshold method as reason of the rate dependence.

5.7.6 Drop at Low Rates

Finally the region of the low rates has to be investigated. Getting an acceptable amount of hits – despite low rates – requires to combine several measurements, otherwise it is not possible to do a reasonable Gaussian fit on the spectrum. In figure 5.17 the pulse height at low rates seems to decrease. However it is not possible to extend this measurement to even lower rates with a silver target and the available aluminium layers. Alternatively it is feasible to investigate the possible trend by using a molybdenum target, since its lower K_α energy leads to lower rates with the available shielding. The obtained results for the molybdenum target are presented in figure 5.22 and include also a silver measurement for comparison.

The indicated signal drop at low rates with the silver target is confirmed by the measurement with molybdenum. Actually the measurement with molybdenum does not only support the trend but also shows a possible plateau for the lowest available rates.

At the end of this diploma thesis the opportunity occurred to do a rate dependence measurement with the next version of the digital ROC, the ROCdigV2. It is simply investigated whether the ROCdigV2 shows the same rate dependence of the signal shape as the ROCdigV1. The shapes of the spectrum method measurements are similar for the different versions of the digital ROC (see figure 5.23). Unfortunately it is not possible to reproduce the threshold method results from figure 5.21, since the range of the adjustable threshold of the ROCdigV2 is too small.

5.7.7 Effects of the rate dependence

Considering the whole available range of rates it is difficult to give a recommendation which rate and hence which tube current and shielding should be preferred. Ideally there is a

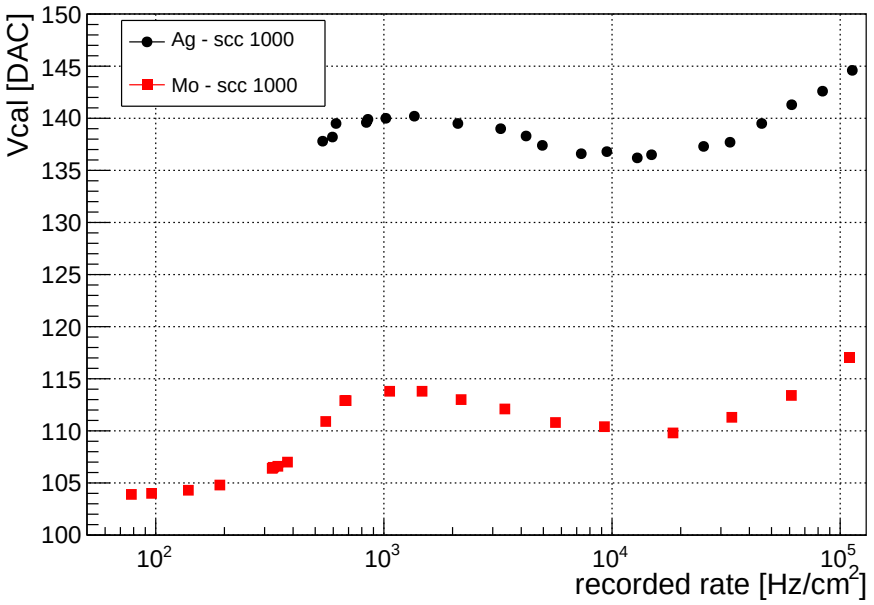

Figure 5.22: Pulse heights at low rates using a silver and a molybdenum target. While the silver measurement only indicates a drop of the signal the molybdenum measurement is able to confirm this trend with a subsequent plateau.

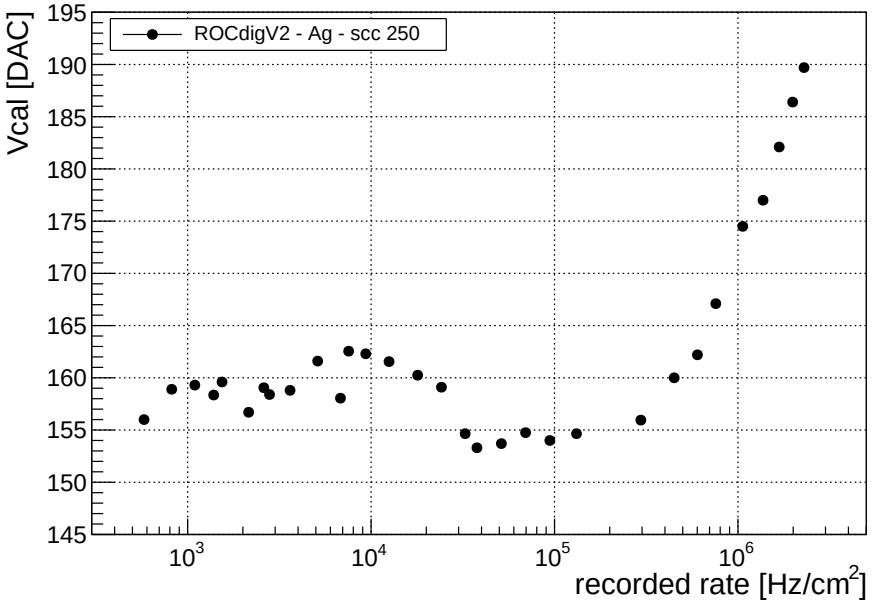

Figure 5.23: Rate dependence of the ROCdigV2 over the entire range using a silver target and *scc* 250. The shape of the signal curve is similar to the shape of the ROCdigV1 in figure 5.16.

plateau region where the pulse height as a function of the rate is constant, but the plateau observed at around 100 Hz/cm^2 in figure 5.22 is not suitable for two reasons. First of all this plateau is not available with each target. For instance, such low rates are not accessible with a silver target and the thickness of the available aluminium layers. Furthermore the statistics at low rates are too low. In figure 5.20 it is visible that the rate dependence has a minor influence around the signal dip. Nevertheless the statistics are still not satisfying due to the required shielding. Certainly the statistics at high rates are sufficient but the handicap here is the strong rate dependence of the pulse height. Consequently the compromise is located somewhere in between which leads to the following settings. Leaving out the shielding has two advantages, obtaining acceptable statistics and reducing the workload. Moreover the tube current should be 2 mA to avoid the region with the greatest rise of the pulse height.

As previously mentioned different targets provide different rates. This effect also shows up in calibration curves for example in figure 5.7. Table A contains the rates of each target from figure 5.7. It is recognisable that all rates are in the region of the pulse height increase (see figure 5.20). Molybdenum shows the highest rate and iron provides the lowest. Hence it is expected that molybdenum and iron do not fit the calibration curves as well as the rest of the targets. Since molybdenum shows a higher rate the rate dependence causes a greater increase of the pulse height. Iron has a distinctively lower rate resulting in a lower increase of the pulse height. Exactly this is observed in figure 5.7: iron, the first target from the bottom, is shifted to lower Vcal values while molybdenum, the fourth target from the bottom, has a distinct shift towards higher Vcal values.

Table 5.1: Rates of the targets used in figure 5.7 with one calibration line per row. The first column gives the *scc* values of the calibration curves. All remaining entries are the rates of the listed targets in multiples of 100 kHz/cm^2. The rates of *no scc* measurements are not assessable due to problems during the creation of their log files.

	target rates [100 kHz/cm^2]							
scc	Ag	Cu	Fe	In	Mo	Nd	Sn	Zn
100	2.45	1.93	0.63	1.66	4.04	1.44	1.37	2.67
250	2.48	2.07	0.63	1.71	4.01	1.47	1.48	2.77
500	2.51	2.11	0.63	1.72	4.02	1.33	1.50	2.78
750	2.57	2.12	0.65	1.72	4.14	1.44	1.49	2.80
1000	2.25	2.11	0.62	1.71	4.00	1.45	1.49	2.77

5.8 TCT/WBC Dependence

Investigating new technology often reveals unexpected random features. For instance, there are two parameters which are responsible for correct timing of the ROC. These two 8-bit registers are the *Write Bunch Crossing* (WBC) and the *Time Calibrate Trigger* (TCT). The WBC works as a *bunch crossing pointer* providing an adjustable timing to chose a certain bunch crossing. The TCT is a testboard timing parameter setting a variable delay of the trigger signal. The operating principle is explained using the example of an ordinary measurement with *scc*. As previously mentioned (see section 4.2.3) measuring with *scc* means that a certain clock cycle and hence the timeframe of a certain bunch crossing is stretched. Profiting from the *scc* is only possible if the stretched bunch crossing is read out. For the further explanation it is assumed that the right timing for the readout of the stretched clock cycle is set. Increasing the TCT and hence the delay leads to a readout of a later bunch crossing, since the trigger which initiates the readout arrives at the ROC later. With this

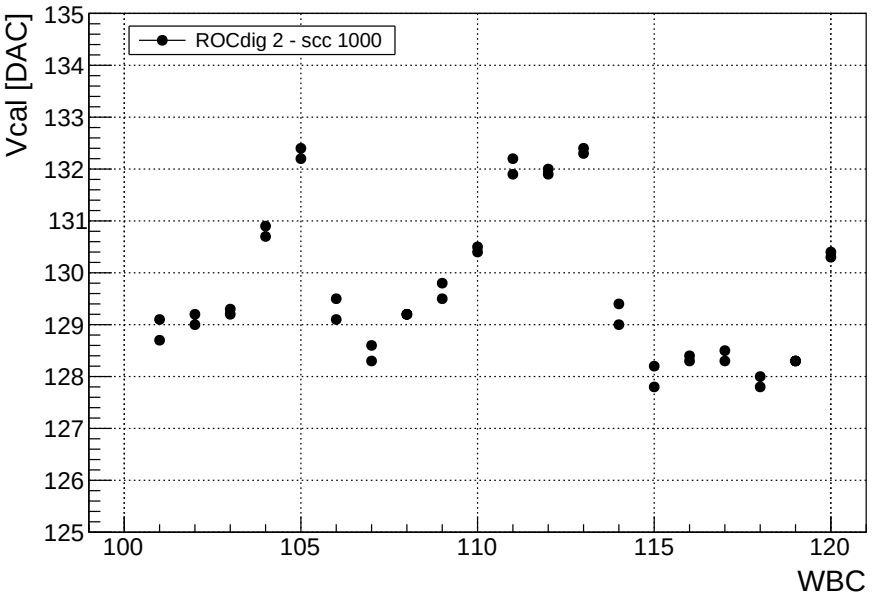

Figure 5.24: TCT/WBC dependence of the pulse height for a ROCdigV1 using a silver target. Checking for statistical uncertainties, each TCT/WBC pair is measured twice at different points of time.

changed timing the stretched clock cycle would not be read out any longer. In order to counteract this the WBC has to be adjusted, too. Increasing the WBC simply results in a readout of the events of an older bunch crossing. If the changes of WBC and TCT have the same value they compensate each other. Using the software TakeData which is introduced in section 4.4 in the laboratory leads to the condition:

$$\mathrm{TCT} - \mathrm{WBC} = 3. \tag{5.2}$$

As long as this condition is fulfilled the stretched clock cycle is read out. Of course this condition may be different for another software or test board. However WBC and TCT should not have any influence on the pulse height since they simply adjust the timing for the readout of the ROC buffers. In order to reduce the measuring effort – keeping the same WBC/TCT for the pre-calibration and TakeData – a different WBC/TCT pair is used. However there is a difference in the observed pulse height. The first step is to check whether this is a statistical effect. For that reason several measurements for certain TCT/WBC pairs with $\mathrm{TCT} - \mathrm{WBC} = 3$ are done.

The results are presented in figure 5.24 showing good reproducibility and ruling out the idea of a statistical variation. Additionally the standard deviation for TCT = 163 and WBC = 160 is calculated to 0.45 Vcal. For this calculation five measurements are used. This result underpins that the observed TCT/WBC dependence is not a statistical variation.

For further investigation and to check if there is any pattern the measuring range is increased in steps of five TCT/WBC units examined with an additional ROCdigV1. The obtained results are displayed in figure 5.25 and illustrate two aspects. Obviously there is no visible pattern and the shape is different for the ROCs presented. Hence this behaviour is even ROC dependent which implies that the chosen TCT/WBC pair should not be changed during all calibrations to achieve a better comparability and to keep the uncertainty small.

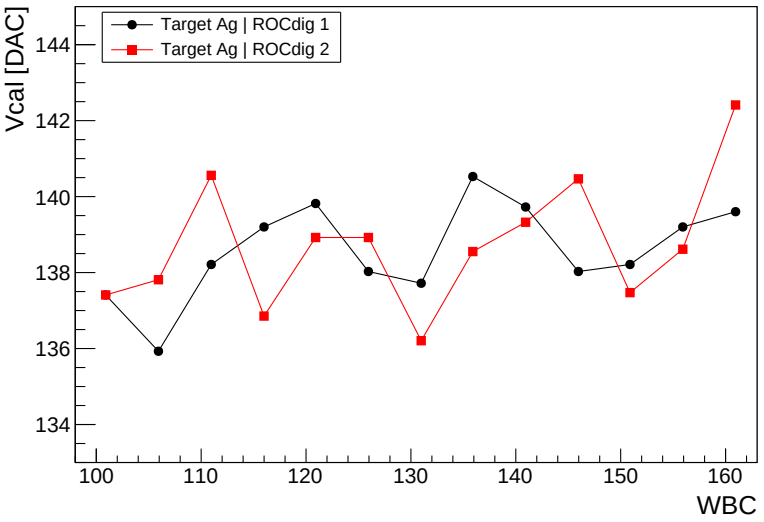

Figure 5.25: TCT/WBC dependence of the pulse height for two ROCdigV1. The measuring range is increased and the step size is five TCT/WBC units. There is no recognisable pattern but the behaviour is apparently ROC dependent.

5.9 Uncertainties

So far the influence of different parameters on the peak position and the associated calibration curves were discussed. In addition all parameters bring along diverse uncertainties on the peak position, some of which are simply statistical while others come up with inappropriate parameter choice. Table 5.2 gives an summary where uncertainties occur and what there sizes are. For each uncertainty there is a separate reference measurement obtained with silver targets and performed with the ROCdigV1 test samples.

- Gaussian fit: When a fit is applied it may occur that the calculated mean of the Gaussian fit is shifted up to +2 Vcal units if the fit-limits are insufficient. This uncertainty is a minor one and can easily be avoided using appropriate limits.
- Stretched clock cycle: The peak position depends strongly on the *scc* value. Based on the *scc* of 1000 the Vcal pulse height may decrease by 38 Vcal at most, this is a large effect but is entirely avoided by choosing constant *scc* values.
- Calibrations at different temperatures: According to section 5.5.1 an ±2.3 Vcal uncertainty of the peak position exists depending on the temperatures. This is probably a minor statistical one and is unavoidable.
- Inconsistent temperatures: If the temperature of pre-calibration and X-ray calibration does not match the Vcal pulse height changes with ±3.1 Vcal/°C. The effect of this uncertainty is determined by the stability and accuracy of the temperature control.
- Pre-calibrations: Due to the functional principle of the pre-calibration routines they never provide entirely consistent results even for identical conditions. The associated minor uncertainty of ±1.2 Vcal is avoided as long as only one pre-calibration is used under stable conditions.
- Recorded rate with spectrum method: The peak position dependence on the rate obtained with the spectrum method is the strongest one observed. In this case an interval from −16.5 Vcal ... +48.9 Vcal is given for the uncertainty referring to the peak obtained with the default tube current and an *scc* of 1000. This uncertainty does not occur when the rate is kept constant, but this is difficult for different targets.

- Recorded rate with threshold method: The threshold method delivers no rate dependence but there is a statistical uncertainty of ±0.6 Vcal units. This very small value can be neglected, anyhow the spectrum method is preferred, as it uses the whole readout chain.
- WBC/TCT: This unexpected dependence results in a statistical uncertainty of ±1.5 Vcal units, however it is easily avoided as long as the WBC/TCT pair stays unchanged.

Table 5.2: List of uncertainties on the peak position, corresponding to silver targets measured obtained with the ROCdigV1.

Parameter	Uncertainty [Vcal]	Uncertainty [%]
One Gaussian fit	+2	1.6
Stretched clock cycle (*scc*)	−38	24.0
Calibrations at different temperatures	±2.3	1.7
Inconsistent temperatures [per °C]	±3.1	2.2
Pre-calibrations	±1.2	0.8
Recorded rate with spectrum method	−16.5 ... +48.9	32.4
Recorded rate with threshold method	±0.6	0.5
WBC/TCT	±1.5	1.2

Summarising it can be said, that the temperature, *scc* as well as the WBC/TCT settings should be fixed within a certain calibration to avoid the corresponding uncertainties. In addition the rate should be fixed as far as possible, however this is difficult for different targets. Further the limits of a one-Gaussian fit have to be chosen reasonably to reduce the uncertainty on the peak position down to 0.2 Vcal. Under stable conditions only one pre-calibration should be used to avoid the associated uncertainty.

6. Summary and Outlook

After the consolidation of the Large Hadron Collider (LHC) during the long shutdown in 2013/14 the maximum centre-of-mass energy $\sqrt{s}$ will increase up to 14 TeV [D$^+$12]. Further the luminosity will reach twice the design luminosity $\mathcal{L}_{\text{upgrade}} = 2 \times \mathcal{L}_{\text{design}} = 2 \times 10^{34}\,\text{cm}^{-2}\text{s}^{-1}$ and the number of simultaneous collisions called pile-up will increase from 25 up to 50. This results in a harsher conditions for the detectors of the experiments in particular with regard to readout speed and radiation hardness. In case of the Compact Muon Solenoid (CMS) experiment this especially concerns the pixel detector which is the innermost part and closest to the interaction point. The tasks of the pixel detector are trajectory and vertex reconstruction of charged particles. In order to maintain its high efficiency and good resolution the entire pixel detector will be replaced during an extended technical stop at the end of 2016. The pixel detector after the upgrade will be equipped with new chips containing digital readout and extended buffers to achieve faster readout speed and to cope with the increased particle rate. Moreover the number of sensitive barrel layers will be increased by one and an additional disc will be placed in each endcap to improve tracking and b-tagging.

At Karlsruhe Institute of Technology (KIT) half of the modules of the new layer four will be produced. Modules are the smallest units in which the pixel detector can be divided. For the evaluation of the modules calibration measurements with monochromatic X-rays are planned.

This thesis has two major objectives. One is to gain experience in the calibration process since this will be the procedure used for the evaluation of the assembled modules while the other objective is to obtain as much know-how of the ROC performance as possible. Therefore the measurements performed within this thesis investigate several experimental parameters such as temperature, clock stretch factor or irradiation rate. In addition this work shows where uncertainties during the calibration occur and how they can be avoided or at least minimised. As far as possible comparisons with the current ROC PSI46V2 are given.

The calibration process relies on the irradiation of the test samples with monochromatic X-rays. For this purpose two test setups are used, one based on an X-ray tube and the other one using an ^{241}Am source. Both generate monochromatic X-rays by exciting some target material and obtaining photons with the corresponding K_α energy while the readout of the recorded data is provided by PSI46 test boards and the software packages psi46expert and TakeData. The detector signal is measured with two different methods, the spectrum method using the whole readout chain and the threshold method which only compares detector signals with an adjustable threshold. Thanks to the two methods it was possible to exclude some parts of the pixel unit cell (PUC) for certain observed properties, however the spectrum

method should be preferred since it is the more realistic method as it uses the whole readout chain.

A first concern of this thesis was the fitting procedure and the investigation of the background. The most effective fitting procedure in terms of accuracy and effort is the application of a one-Gaussian fit with reasonably chosen limits. It is not necessary to perform any background correction since this provides no improvement for the fitting process.

The influences of irradiation rate, clock stretch factor and WBC on the detector signal revealed several unexpected dependences.

- ***scc* dependence**: The detector signal of the ROCdigV1 shows a steep rise for increasing *scc* values up to about 200 followed by a moderate increase. This behaviour occurs independently of the target and was already detected with the analog ROC PSI46V2 [Hos12]. The reason for this effect my be connected with the sampling time of the signal, but so far there is no test available to check this assumption.
- **Signal dip due to rate dependence**: There is a signal dip at rates of 10-20 kHz/cm^2 observed with both ROCdigV1 and ROCdigV2 and occurring independently of *scc* value and target. The signal dip also occurs for the analog ROC PSI46V2 at rates around 7-8 kHz/cm^2 where it is much more pronounced. Responsible for the signal dip is the storage capacitor of the sample-and-hold circuit shown in figure 3.12. A change in the powering of the amplifier in the sample-and-hold circuit of the ROCdigV1 and ROCdigV2 minimized this effect.
- **Rise at high rates**: At rates above 100 kHz/cm^2 the detector signal of both ROCdigV1 and ROCdigV2 shows a steep increase which is entirely different compared to the observed pulse height drop of the analog ROC PSI46V2. Just as the signal dip this effect occurs independently of *scc* value and target. It is not possible to explain the increase with the behaviour of the digital and analog currents as both of them are constant at rates above 100 kHz/cm^2. Since measurements with the threshold method revealed no rate dependence the reason for increase is related to some components after the comparator in the PUC. In order to avoid a strong influence on the calibration rates below 200 kHz/cm^2 should be preferred.
- **Drop at low rates**: A drop of the pulse heights at low rates (below 0.6-1 kHz/cm^2) is indicated by measurements with a silver target, but it is not possible to reach lower rates with the available equipment and a silver target. However it is possible to extend the measurements with a molybdenum target which confirms the signal drop at low rates. Actually the measurement with molybdenum does not only confirm the trend but also shows a possible plateau for the lowest available rates.
- **WBC/TCT dependence**: Measurements of the ROCdigV1 show a WBC/TCT dependence of the pulse height with a dispersion of 5 Vcal units. There is no visible pattern and the shape is different for each considered ROCdigV1 which indicates that this behaviour is even ROC dependent. This implies that the chosen TCT/WBC pair should not be changed during all calibrations to achieve a better comparability and to avoid this effect entirely.

In contrast to the analog ROC PSI46V2 the digital ROCs do not show any temperature dependence of the calibration curves. All calibration curves of the ROCdigV1 are obtained with the spectrum method and provide slopes of around 50.52 $\pm$ 0.19 e/DAC which seems to be a reliable value. The results of the ROCdigV2 deliver slopes of about 47.28 $\pm$ 0.55 e/DAC which are slightly lower compared to the ROCdigV1. In addition table 5.2 indicates where uncertainties occur and what their sizes are while the description explains how most of them – particularly the largest ones – can be avoided. However a systematic uncertainty of

approximately 0.19 e/DAC remains. Further measurements concerning the ROCdigV1 are for instance documented in [Def13] and for the ROCdigv2 in [eM13].

For better understanding of the calibration curves and the associated slightly lower slopes of the ROCdigV2 more experience with that readout chip and higher statistics are required. Of great interest are measurements at temperatures around $-20\,^{\circ}\mathrm{C}$ and a more detailed investigation of the Vsf influence.

It is proposed to equip the X-ray tube setup with more powerful cooling in order to achieve temperatures down to at least $-20\,^{\circ}\mathrm{C}$. This would provide the opportunity to prove the calibration results obtained with the source setup at significant higher rates. Further the rate dependence with special regard to regions of the signal dip and the steep signal increase could be investigated for additional temperatures. This could be implemented when the X-ray tube is adapted for the upcoming module production and the associated evaluation of complete modules.

Summarising it can be said that this work can be used as the foundation of a calibration procedure for the new pixel detector. As soon as the prototype production is done and the available time to test a full module is known a detailed calibration plan has to be established.

Bibliography

[A+09] L. Agostino *et al.*: *Commissioning of the CMS High Level Trigger.* J. Instrum., 4 CMS-NOTE-2009-012:P10005. 14 p, June 2009.

[A+12] G. Aad *et al.*: *Observation of a new particle in the search for the Standard Model Higgs boson with the ATLAS detector at the LHC.* Physics Letters B, B716:1–29, 2012.

[Abb13] M. Abbrescia: *Operation, performance and upgrade of the CMS RPC muon system at LHC.* Technical Report CMS-CR-2013-072, CERN, Geneva, March 2013.

[ALI08] ALICE Collaboration: *The ALICE experiment at the CERN LHC. A Large Ion Collider Experiment.* J. Instrum., 3:S08002. 259 p, 2008.

[ATL08] ATLAS Collaboration: *The ATLAS Experiment at the CERN Large Hadron Collider.* J. Instrum., 3:S08003. 437 p, 2008.

[ATL13] ATLAS Collaboration: *Combined coupling measurements of the Higgs-like boson with the ATLAS detector using up to 25 fb^{-1} of proton-proton collision data.* Technical Report ATLAS-CONF-2013-034, CERN, Geneva, March 14, 2013.

[B+00] G. L. Bayatyan *et al.*: *CMS TriDAS Project: Technical Design Report, Volume 1: The Trigger Systems.* Technical Design Report CMS. Geneva, December 15, 2000.

[B+04] O. S. Brüning *et al.*: *LHC Design Report.* CERN, Geneva, 2004.

[B+07] A. Bulgheroni *et al.*: *EUTelescope: Tracking Software.* EUDET-Memo-2007-20, 2007.

[B+12a] G. Bauer *et al.*: *The CMS High Level Trigger System: Experience and Future Development.* Technical Report CMS-CR-2012-147, CERN, Geneva, June 2012.

[B+12b] J. Beringer *et al.*: *Review of Particle Physics, 2012-2013. Review of Particle Properties.* Phys. Rev. D, 86(1):010001, 2012.

[Bar13] D. Barney: *Interactive Slice of the CMS detector*, August 22 2013. `https://cms-docdb.cern.ch/cgi-bin/PublicDocDB/ShowDocument?docid=4172`.

[Bon12] O. Bondu: *Photon energy scale determination and commissioning with radiative Z decays.* Technical Report CMS-CR-2012-031, CERN, Geneva, January 2012.

[BR97] R. Brun and F. Rademakers: *ROOT – An object oriented data analysis framework.* Nuclear Instruments and Methods in Physics Research Section A: Accelerators, Spectrometers, Detectors and Associated Equipment, 389(12):81 – 86, April 1997.

[Bro07] R. M. Brown: *The CMS Lead Tungstate Electromagnetic Calorimeter.* Technical Report CMS-CR-2007-047, CERN, Geneva, September 2007.

[But12] E. M. Butz: *Operation and Performance of the CMS Silicon Tracker.* Technical Report CMS-CR-2012-357, CERN, Geneva, November 2012.

[C+12] S. Chatrchyan *et al.*: *Observation of a new boson at a mass of 125 GeV with the CMS experiment at the LHC.* Physics Letters B, B716:30–61, 2012.

[CER09] CERN Video Productions: *Two beams circulating in the LHC! First collisions in four detectors!* November 2009.

[CGL09] A. G. Cohen, S. L. Glashow, and Z. Ligeti: *Disentangling Neutrino Oscillations.* Phys.Lett., B678:191–196, 2009.

[CMS97a] *The CMS muon project: Technical Design Report.* Technical Design Report CMS. CERN, Geneva, 1997.

[CMS97b] CMS Collaboration: *The CMS hadron calorimeter project: Technical Design Report.* Technical Design Report CMS. CERN, Geneva, 1997.

[CMS06] CMS Collaboration: *CMS Physics: Technical Design Report Volume 1: Detector Performance and Software.* Technical Design Report CMS. CERN, Geneva, 2006.

[CMS07] CMS Collaboration: *CMS Physics: Technical Design Report Volume 2: Physics Performance.* Technical Design Report CMS. CERN, Geneva, 2007.

[CMS08] CMS Collaboration: *The CMS experiment at the CERN LHC. The Compact Muon Solenoid experiment.* Technical report, 2008.

[CMS10] CMS Collaboration: *Commissioning and Performance of the CMS Pixel Tracker with Cosmic Ray Muons.* J. Instrum., 5(CMS-CFT-09-001):T03007. 37 p, 2010.

[CMS11] *Technical proposal for the upgrade of the CMS detector through 2020.* CMS Collaboration, CERN-LHCC-2011-006, June 2, 2011.

[CMS13a] *CMS Higgs Physics Results*, August 21 2013. `https://twiki.cern.ch/twiki/bin/view/CMSPublic/PhysicsResultsHIG`.

[CMS13b] *CMS silicon pixel detector*, September 9 2013. `http://cms.web.cern.ch/news/silicon-pixels`.

[CMS13c] CMS Collaboration: *Observation of a new boson with mass near 125 GeV in pp collisions at $\sqrt{s}$ = 7 and 8 TeV.* Technical Report CMS-HIG-12-036, CERN, Geneva, March 19 2013.

[Com06a] Wikimedia Commons: *Dotierung im zweidimensionales Siliziumkristallgitter mit Aluminium* [sic], September 11 2006. `http://commons.wikimedia.org/wiki/File:Schema_-_p-dotiertes_Silicium.svg`, File: Schema - p-dotiertes Silicium.svg.

[Com06b] Wikimedia Commons: *Dotierung im zweidimensionales Siliziumkristallgitter mit Phosphor* [sic], September 11 2006. `http://commons.wikimedia.org/wiki/File:Schema_-_n-dotiertes_Silicium.svg`, File: Schema - n-dotiertes Silicium.svg.

[CRS02] S. Cittolin, A. Ràcz, and P. Sphicas: *CMS TriDAS Project: Technical Design Report, Volume 2: Data Acquisition and High-Level Trigger. CMS trigger and data-acquisition project.* Technical Design Report CMS. CERN, Geneva, 2002.

[D+12] A. Dominguez *et al.*: *CMS Technical Design Report for the Pixel Detector Upgrade.* CERN-LHCC-2012-016, Geneva, September 27, 2012.

[Dam09] S. Dambach: *CMS pixel module readout optimization and study of the B^0 lifetime in the semileptonic decay mode.* PhD thesis, ETH Zürich, 2009.

[Def13] M. Deffert: *Untersuchung des digitalen Auslesechips PSI46dig für das Phase-I-Upgrade des CMS-Experimentes.* Bachelor Thesis, IEKP-Bachelor/2013-08, May 28 2013.

[Dem05] W. Demtröder: *Experimentalphysik 3: Atome, Moleküle und Festkörper.* Springer, 2005, ISBN 9783540214731.

[Dem07] W. Demtröder: *Laserspektroskopie: Grundlagen und Techniken.* Springer-Verlag, Berlin-Heidelberg, 5. edition, 2007, ISBN 978-3-540-33792-8.

[DIN08] *Industrial platinum resistance thermometers and platinum temperature sensors.* Technical Report DIN EN 60751, Deutsches Institut für Normung, 2008.

[Dud13] *Duden Online.* Bibliographisches Institut, September 20 2013. `http://www.duden.de/node/808152/revisions/1230875/view`.

[EB64] F. Englert and R. Brout: *Broken Symmetry and the Mass of Gauge Vector Mesons.* Phys. Rev. Lett., 13:321–323, 1964.

[EB08] L. Evans and P. Bryant: *LHC Machine.* J. Instrum., 3(08):S08001, August 2008.

[eM13] K. el Morabit: *Untersuchung von Testverfahren für die Produktion von CMS-Pixel-Modulen.* Bachelor Thesis, IEKP-Bachelor/2013-23, September 2013.

[Erd10] W. Erdmann: *The CMS pixel detector.* Int.J.Mod.Phys., A25:1315–1337, 2010.

[Esp96] J. R. Espinosa: *Theoretical Higgs mass bounds in the standard model and supersymmetric extensions.* DESY-96-107:37, June 1996.

[F$^+$08] H. Flächer *et al.*: *Revisiting the Global Electroweak Fit of the Standard Model and Beyond with Gfitter.* Eur. Phys. J. C, 60(CERN-OPEN-2008-024):543–583. 65 p, October 2008.

[F$^+$12] P. Fessia *et al.*: *The LHC Incident in Sector 3-4: A Simplified Mechanical Model to Explain the Mechanical Damages.* IEEE Trans. Appl. Supercond., 22(CERN-ATS-2012-042):4905304. 5 p, February 2012.

[Gab05] K. Gabathuler: *PSI46 Pixel Chip - External Specification.* Technical report, Paul Scherrer Institut, 2005.

[GHK64] G. S. Guralnik, C. R. Hagen, and T. W. B. Kibble: *Global Conservation Laws and Massless Particles.* Phys. Rev. Lett., 13:585–587, 1964.

[Gra53] F. Gray: *Pulse Code Communication.* United States Patent 2632058, March 1953.

[Gri08] D. Griffiths: *Introduction to Elementary Particles.* Wiley, 2008, ISBN 9783527406012.

[Har09] F. Hartmann: *Evolution of Silicon Sensor Technology in Particle Physics.* Springer Tracts in Modern Physics. Springer, 2009, ISBN 9783540250944.

[Hei12] S. Heitz: *Bump-Bonding-Technologie für das Upgrade des CMS-Pixeldetektors.* Diplomarbeit, IEKP-KA/2012-16, Oktober 2 2012.

[Hig64a] P. W. Higgs: *Broken Symmetries and the Masses of Gauge Bosons.* Phys. Rev. Lett., 13:508–509, October 1964.

[Hig64b] P. W. Higgs: *Broken symmetries, massless particles and gauge fields.* Physics Letters, 12:132–133, 1964, ISSN 0031-9163.

[Hil08] U. Hilleringmann: *Silizium-Halbleitertechnologie: Grundlagen mikroelektronischer Integrationstechnik.* Vieweg+Teubner Verlag, 2008, ISBN 9783835102453.

[Hos12] J. Hoss: *X-Ray Calibration of Pixel Detector Modules for the Phase I Upgrade of the CMS Experiment*. Diplomarbeit, IEKP-KA/2012-17, September 27 2012.

[HS12] F. Hartmann and A. Sharma: *Multipurpose detectors for high energy physics, an introduction*. Nucl. Instrum. Methods Phys. Res., A, 666:1–9, 2012.

[K+98] V. Karimäki *et al.*: *The CMS tracker project: Technical Design Report*. Technical Design Report CMS. CERN, Geneva, 1998.

[Käs13] H. C. Kästli: Private communitcation, March 18 2013.

[Kei13] Keithley 2410 High-Voltage SourceMeter, September 22 2013. `http://www.keithley.com/products/dcac/currentvoltage/2400smu/?mn=2410`.

[Lab13] National Instruments LabVIEW 2009, September 22 2013. `http://www.ni.com/labview/`.

[LDM+11] LHC Higgs Cross Section Working Group, S. Dittmaier, C. Mariotti, G. Passarino, and R. Tanaka (Eds.): *Handbook of LHC Higgs Cross Sections: 1. Inclusive Observables*. CERN-2011-002, CERN, Geneva, 2011.

[Lef09] C. Lefevre: *LHC: the guide (English version). Guide du LHC (version anglaise)*. Feb 2009.

[LEP01] *Search for the Standard Model Higgs Boson at LEP*. Technical Report CERN-DELPHI-2001-113-CONF-536, CERN, Geneva, July 2001.

[LHC98] LHCb Collaboration: *LHCb: Technical Proposal*. Tech. Proposal. CERN, Geneva, 1998.

[LHC08a] LHCb Collaboration: *The LHCb Detector at the LHC*. J. Instrum., 3 LHCb-DP-2008-001:S08005, 2008.

[LHC08b] LHCf Collaboration: *The LHCf detector at the CERN Large Hadron Collider*. J. Instrum., 3:S08006, 2008.

[LHM+13] LHC Higgs Cross Section Working Group, S. Heinemeyer, C. Mariotti, G. Passarino, and R. Tanaka (Eds.): *Handbook of LHC Higgs Cross Sections: 3. Higgs Properties*. CERN-2013-004, CERN, Geneva, 2013.

[Lut99] G. Lutz: *Semiconductor Radiation Detectors: Device Physics*. Accelerator Physics Series. Springer-Verlag, 1999, ISBN 9783540648598.

[Man02] R. Mancini: *Op Amps for everyone*. Texas Instruments, Aug 2002.

[Mei11] B. Meier: *CMS pixel detector with new digital readout architecture*. J. Instrum., 6(01):C01011, 2011.

[MoE09] MoEDAL Collaboration: *Technical Design Report of the MoEDAL Experiment*. Technical Report CERN-LHCC-2009-006, CERN, Geneva, June 2009.

[Mol99] M. Moll: *Radiation Damage in Silicon Particle Detectors - Microscopic Defects and Macroscopic Properties*. PhD thesis, Universität Hamburg, 1999.

[Moo94] B. Moore: *Evidence against dissipationless dark matter from observations of galaxy haloes* [sic]. Nature, 370:629, 1994.

[Ngu11] M. Nguyen: *Jet Reconstruction with Particle Flow in Heavy-Ion Collisions with CMS*. Technical Report CMS-CR-2011-088, CERN, Geneva, June 2011.

[NIS13] *X-ray Transition Energies Database*, August 23 2013. `http://www.nist.gov/pml/data/xraytrans/index.cfm`, National Institute of Standards and Technology.

[P+95] G. Pfennig *et al.*: *Karlsruher Nuklidkarte*. Forschungszentrum Karlsruhe GmbH, 1995.

[Phy12] Tevatron New Physics: *Updated Combination of CDF and D0 Searches for Standard Model Higgs Boson Production with up to 10.0 fb-1 of Data*. Technical Report FERMILAB-CONF-12-318-E, July 2012.

[Pov04] B. Povh: *Particles and Nuclei: An Introduction to the Physical Concepts*. Springer-Verlag GmbH, 2004, ISBN 9783540201687.

[R+06] L. Rossi *et al.*: *Pixel Detectors: From Fundamentals to Applications*. Particle Acceleration and Detection. Springer, Berlin, 2006, ISBN 978-3-540-28332-4.

[Sat08] A. Satpathy: *Overview and status of the CMS silicon strip tracker*. Journal of Physics: Conference Series, 110(9):092026, 2008.

[Sch95] P. Schmüser: *Feynman - Graphen und Eichtheorien für Experimentalphysiker*. Lecture notes in physics. Springer-Verlag GmbH, 1995, ISBN 9783540584865.

[Sch05] E. F. Schubert: *Doping in III-V Semiconductors*. Cambridge Studies in Semiconductor Physics and Microelectronic Engineering. Cambridge University Press, 2005, ISBN 9780521017848.

[Sem13] Philips Semiconductors: *The I^2C-bus and how to use it*, September 22 2013. `http://www.i2c-bus.org/fileadmin/ftp/i2c_bus_specification_1995.pdf`.

[Sha09] A. Sharma: *The readiness of CMS for exotic physics at LHC*. Technical Report CERN-PH-EP-2009-004, CERN, Geneva, February 2009.

[Spa12] S. Spannagel: *A High-Rate Beam Test for the CMS Pixel Detector Phase I Upgrade*. Diplomarbeit, IEKP-KA/2012-15, November 2 2012.

[SS07] I. O. Stamatescu and E. Seiler: *Approaches to Fundamental Physics: An Assessment of Current Theoretical Ideas*. Springer, Berlin, 2007, ISBN 978-3-540-71115-5.

[TOT08] TOTEM Collaboration: *The TOTEM Experiment at the CERN Large Hadron Collider*. J. Instrum., 3:S08007, 2008.

[Trü08] P. Trüb: *CMS pixel module qualification and Monte-Carlo study of $H \to \tau^+\tau^- \to l^+l^- ET$*. PhD thesis, ETH Zürich, 2008.

[VPB07] T. Virdee, A. Petrilli, and A. Ball: *CMS High Level Trigger*. Technical Report CERN-LHCC-2007-021, CERN, Geneva, June 2007.

[Woc13] J. Wochele: *4345LV: Am-241 X-ray Quelle variabler Energie*, September 23 2013. `www-ik.fzk.de/~ssb/pdf/Am_4345LV.pdf`.

[WZ74] J. Wess and B. Zumino: *Supergauge transformations in four dimensions*. Nucl. Phys. B, 70(CERN-TH-1753. 1):39–50, 1974.

[Zim09] F. Zimmermann: *CERN Upgrade Plans for the LHC and its Injectors*. PoS, EPS-HEP2009(sLHC-PROJECT-Report-0016):140. 5 p, July 2009.

Appendix

A Data Documentation

Table A assigns the measurement data of presented figures and tables with the raw data source for internal documentation. For threshold measurements no run number are available.

Table A.1: Raw data sources of presented measurements

Figure or table	date	remark	PC	test sample	run number or pre-calibration
Figure 4.1	15/02/2013		ikhero8	ROCdigV1-1	62 - 75
Figure 4.9	08/01/2013	Mo	ikhero9	ROCdigV1-1	100
Figure 4.10	23/05/2013		ikhero9	ROCdigV1-1	20130523_XrayBox_T20_ROCdig
Figure 5.1 (a)	08/01/2013	Ag, 2 mA	ikhero9	ROCdigV1-1	82
Figure 5.1 (b)	08/01/2013	Ag, 22 mA	ikhero9	ROCdigV1-1	92
Figure 5.2 (a)	21/01/2013	without target	ikhero9	ROCdigV1-1	411
	21/01/2013	PVC dummy	ikhero9	ROCdigV1-1	413
Figure 5.2 (b)	08/01/2013	Ag	ikhero9	ROCdigV1-1	82
	08+21/01/2013	without target	ikhero9	ROCdigV1-1	82, 411
	08+21/01/2013	PVC dummy	ikhero9	ROCdigV1-1	82, 413
Figure 5.3 (a) & (b)	08/01/2013	Ag	ikhero9	ROCdigV1-1	82
Figure 5.4 (a)	08+21/01/2013	Ag	ikhero9	ROCdigV1-1	82, 413
Figure 5.4 (b)	08+21/01/2013	Mo	ikhero9	ROCdigV1-1	100, 413

Figure or table	date	remark	PC	test sample	run number or pre-calibration
Figure 5.5	08+21/01/2013	Ag	ikhero9	ROCdigV1-1	82, 413
Figure 5.6	11/01/2013	Ag	ikhero9	ROCdigV1-1	82, 148, 266 - 280
	11/04/2013	Mo	ikhero9	ROCdigV1-2	3 - 27, 40, 53, 66, 79
	19/04/2012	Ag	ikhero9	sensor 8	25 - 41
Figure 5.7	07/01/2013	$scc = 1$	ikhero9	ROCdigV1-1	45 - 55
	07/01/2013	$scc = 100$	ikhero9	ROCdigV1-1	60 - 69
	08/01/2013	$scc = 250$	ikhero9	ROCdigV1-1	82, 97 - 104
	08/01/2013	$scc = 500$	ikhero9	ROCdigV1-1	105 - 113
	09/01/2013	$scc = 750$	ikhero9	ROCdigV1-1	127 - 135
	09/01/2013	$scc = 1000$	ikhero9	ROCdigV1-1	161 - 169
Figure 5.8 (a) & (b)	29+30/03/2012		ikhero12	sensor 6	183 - 205
Figure 5.9 (a) & (b)	15/02/2013	20 °C	ikhero8	ROCdigV1-1	62 - 75
	18/02/2013	10 °C	ikhero8	ROCdigV1-1	148 - 159
	15/02/2013	0 °C	ikhero8	ROCdigV1-1	76 - 87
	17/02/2013	−5 °C	ikhero8	ROCdigV1-1	136 - 147
	17/02/2013	−10 °C	ikhero8	ROCdigV1-1	124 - 135
	17/02/2013	−15 °C	ikhero8	ROCdigV1-1	112 - 123
	16/02/2013	−20 °C	ikhero8	ROCdigV1-1	88 - 99
Figure 5.10	20/08/2013	Vsf = 85	ikhero9	ROCdigV2-S13	169 - 173
	20/08/2013	Vsf = 95	ikhero9	ROCdigV2-S13	174 - 181
	27/08/2013	Vsf = 100	ikhero9	ROCdigV2-S13	196 - 203
	21/08/2013	Vsf = 105	ikhero9	ROCdigV2-S13	182 - 190
	21/08/2013	Vsf = 135	ikhero9	ROCdigV2-S13	191 - 195
Figure 5.11	27/02/2013	Ag	ikhero8	ROCdigV1-1	185 - 202
Figure 5.12 (a)	15-27/02/2013	Ag	ikhero8	ROCdigV1-1	64/64, 160 - 162, 175/176, 205-208, 210/211
Figure 5.13	31/01/12	Ag	ikhelap56	sensor 8	411 - 437, 475 - 480
	31/01/12	Mo	ikhelap56	sensor 8	438 - 461, 462 - 473
	18,19+23/01/12	Sn	ikhelap56	sensor 8	254 - 261, 262 - 293
Figure 5.14	15/04/2013	Mo, $scc = 100$	ikhero9	ROCdigV1-2	79 - 91
	15/04/2013	Mo, $scc = 250$	ikhero9	ROCdigV1-2	66 - 78

Figure or table	date	remark	PC	test sample	run number or pre-calibration
	13/04/2013	Mo, $scc = 500$	ikhero9	ROCdigV1-2	53 - 65
	13/04/2013	Mo, $scc = 750$	ikhero9	ROCdigV1-2	40 - 52
	13/04/2013	Mo, $scc = 1000$	ikhero9	ROCdigV1-2	27 - 39
Figure 5.15 (a) & (b)	16/01/2013	Ag, $scc = 100$	ikhero9	ROCdigV1-1	305 - 321
	15/01/2013	Ag, $scc = 250$	ikhero9	ROCdigV1-1	281 - 297
	11/01/2013	Ag, $scc = 500$	ikhero9	ROCdigV1-1	245 - 265
	11/01/2013	Ag, $scc = 750$	ikhero9	ROCdigV1-1	222 - 244
	10/01/2013	Ag, $scc = 1000$	ikhero9	ROCdigV1-1	199 - 221
Figure 5.16	08+11+23/01/2013	Ag, $scc = 500$	ikhero9	ROCdigV1-1	113 - 125, 245 - 265, 477 - 483
	09+11+23/01/2013	Ag, $scc = 750$	ikhero9	ROCdigV1-1	130, 136 - 147, 222 - 236, 490, 491
	08+10+23/01/2013	Ag, $scc = 1000$	ikhero9	ROCdigV1-1	148 - 160, 191 - 212, 492 - 499
Figure 5.17	11+23/01/2013	Ag, $scc = 500$	ikhero9	ROCdigV1-1	245 - 265, 477 - 483
	11+23/01/2013	Ag, $scc = 750$	ikhero9	ROCdigV1-1	222 - 236, 490, 491
	10+23/01/2013	Ag, $scc = 1000$	ikhero9	ROCdigV1-1	191 - 212, 492 - 499
Figure 5.18	11+23/01/2013	currents, $scc = 500$	ikhero9	ROCdigV1-1	245 - 265, 477 - 483
	11+23/01/2013	currents, $scc = 750$	ikhero9	ROCdigV1-1	222 - 236, 490, 491
	10+23/01/2013	currents, $scc = 1000$	ikhero9	ROCdigV1-1	191 - 212, 492 - 499
Figure 5.19	08+10+23/01/2013	Ag	ikhero9	ROCdigV1-1	148 - 160, 191 - 212, 492 - 499
	16/01/2013	Mo	ikhero9	ROCdigV1-1	322 - 333
	31/01/12	Ag	ikhelap56	sensor 8	411 - 437
Figure 5.20	08+11/01/2013	Ag, $scc = 500$	ikhero9	ROCdigV1-1	113 - 125, 245 - 253
	09+11+23/01/2013	Ag, $scc = 750$	ikhero9	ROCdigV1-1	130, 136 - 147, 222 - 230
	08+10+23/01/2013	Ag, $scc = 1000$	ikhero9	ROCdigV1-1	148 - 160, 191 - 207
Figure 5.21	13/04/2013	spectrum	ikhero9	ROCdigV1-2	40 - 52
Figure 5.22	10+23/01/2013	Ag, $scc = 1000$	ikhero9	ROCdigV1-1	191 - 212, 492 - 499
	16/01/2013	Mo	ikhero9	ROCdigV1-1	322 - 343
Figure 5.23	09/08/2013	Ag	ikhero9	ROCdigV2-S13	122 - 125, 128 - 149
Table A	07/01/2013	$scc = 100$	ikhero9	ROCdigV1-1	60 - 69
	08/01/2013	$scc = 250$	ikhero9	ROCdigV1-1	82, 97 - 104
	08/01/2013	$scc = 500$	ikhero9	ROCdigV1-1	105 - 113

Figure or table	date	remark	PC	test sample	run number or pre-calibration
	09/01/2013	$scc = 750$	ikhero9	ROCdigV1-1	127 - 135
	09/01/2013	$scc = 1000$	ikhero9	ROCdigV1-1	161 - 169
Figure 5.24	19+21/03/2013	Ag	ikhero8	ROCdigV1-2	72 - 111
Figure 5.25		Ag	ikhero8	ROCdigV1-2	72 - 111, 116 - 201
	04/03/2013	Ag	ikhero8	ROCdigV1-1	209 - 235

Danksagung

Abschließend möchte ich mich all denjenigen bedanken, die mich während meiner Diplomarbeit unterstützt haben und zum Gelingen dieser beigetragen haben.

Zuallererst geht mein Dank an Prof. Dr. Ulrich Husemann für seine ausgezeichnete Betreuung und für die Möglichkeit, eigenständig zu arbeiten. Prof. Dr. Marc Weber danke ich für die Übernahme des Korreferats.

Dr. Thomas Weiler möchte ich für die ausgiebige Unterstützung, die detaillierte Einarbeitung in alle Testsysteme und für die regelmäßigen und sehr hilfreichen Diskussionen meiner Messergebnisse danken. Darüber hinaus natürlich auch für das ausführliche Korrekturlesen, selbst wenn er eigentlich keine Zeit hatte!

Stefan Heindl, der stets jede Frage beantworten konnte, dabei aber auch immer zur guten Laune durch Anekdoten aus dem aktuellen Tagesgeschehen beitrug. Selbstverständlich gilt auch ihm mein Dank für das akribische Korrekturlesen.

Vielen Dank auch an Dr. Hans Jürgen Simonis, für die Hilfe bei jeglichen IT-bezogenen Problemen und dafür, dass er versuchte, mit die klassische Musik näher zu bringen. Tobias Barvich für eine gute und immer nette Zusammenarbeit, selbst dann noch, wenn wieder einmal eine Kleinigkeit zu reparieren war.

Robert Eber danke ich ebenfalls für das Korrekturlesen. Sowie ihm und allen anderen Mitgliedern der Pixeldetektor-, Streifendetektor- und Analysegruppe für ein sehr angenehmes Klima, bei dem es nie eine Zeit gab, zu der ich nicht gerne zur Arbeit gekommen wäre. Der Elektronikwerkstatt, die sofort zur Stelle war, wenn man ihre Hilfe brauchte.

Marco Deffert und Karim el Morabit für viele Stunden gemeinsamen Messens und Diskutierens der Ergebnisse. Natürlich auch Fabian Hoffmann und Jan Müller, die keine Frage zu ROOT unbeantwortet ließen.

Für alle Hilfe bei organisatorischen und bürokratischen Angelegenheiten bedanke ich mich bei Frau Diana Fellner-Thedens sowie Frau Brigitte Gering.

Vor allem möchte ich mich bei meinen Eltern Andrea und Bernhard Freund bedanken, die mich während meines gesamten Studium unterstützten und dieses erst ermöglichten. Bei meinen Brüdern Sebastian und Moritz Freund, die dafür sorgten, dass ich mich nicht nur mit Physik beschäftigte.

Ganz besonders danke ich meiner Freundin Stefanie Krickl, die in den letzten Jahren so viel Geduld hatte und mich – obwohl sie oft kürzer gekommen ist – zu jeder Zeit unterstützte. Außerdem danke ich auch ihr für das ausgiebige Korrekturlesen.

Danke aber auch an alle Freunde, Verwandte und Bekannte die das Studium zu einer wunderbaren Zeit gemacht haben!

Hiermit versichere ich, die vorliegende Arbeit selbstständig verfasst
und nur die angegebenen Hilfsmittel verwendet zu haben.

Benedikt Freund

Karlsruhe, September 2013